Downloaded from orbit.dtu.dk on: Apr 18, 2025

DTU Library

Production of Hot Electrons for Enhancement of Surface Reactivity

Nielsen, Gunver

Publication date:
2009

Document Version
Publisher's PDF, also known as Version of record

Link back to DTU Orbit

Citation (APA):
Nielsen, G. (2009). *Production of Hot Electrons for Enhancement of Surface Reactivity*. Technical University of Denmark.

General rights
Copyright and moral rights for the publications made accessible in the public portal are retained by the authors and/or other copyright owners and it is a condition of accessing publications that users recognise and abide by the legal requirements associated with these rights.

- Users may download and print one copy of any publication from the public portal for the purpose of private study or research.
- You may not further distribute the material or use it for any profit-making activity or commercial gain
- You may freely distribute the URL identifying the publication in the public portal

If you believe that this document breaches copyright please contact us providing details, and we will remove access to the work immediately and investigate your claim.

Production of Hot Electrons for Enhancement of Surface Reactivity

Ph.D. Thesis by Gunver Nielsen

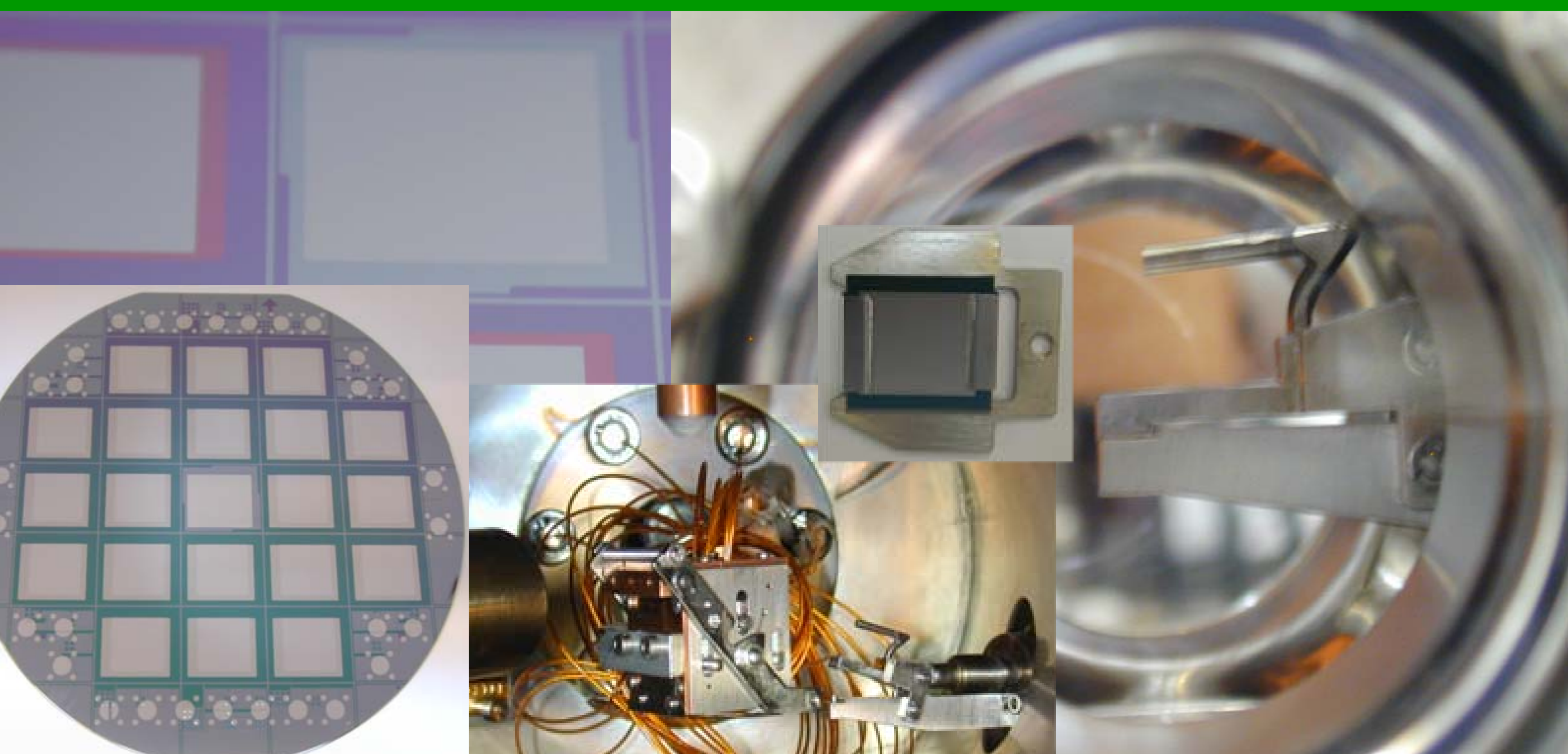

Center for Individual Nanoparticle Functionality
Department of Physics
Technical University of Denmark

September 2009

Preface

This thesis is submitted in partial fulfilment of the requirements for obtaining the Ph.D. degree from the Technical University of Denmark (DTU). The work presented has been carried out in the period from the 1st of August, 2005 to the 10th of September, 2009 at Center for Individual Nanoparticle Functionality (CINF), Department of Physics, DTU, under the supervision of Professor Ib Chorkendorff, CINF, and Associate Professor Ole Hansen, CINF and Nanotech, DTU. CINF is funded by the Danish National Research Foundation. My contribution to the experimental work was interrupted from February to October 2008 when I was on maternity leave with my son, Thomas, born in March 2008.

First of all I would like to thank my two supervisors for being so enthusiastic and helpful and for always having time for discussion or answering questions. Ib has been a very encouraging supervisor, setting things in perspective and asking the good (devil's advocate) questions. Throughout the project he has always helped when the UHV struggle got tough. Ole has shared of his bottomless well of knowledge and experience, and I really appreciate his thorough and pedagogical way of explaining things, also when I had to ask the most basic questions.

It must be stressed, that the progress made within the HEFatS (Hot Electron Femtochemistry at Surfaces) project presented in this thesis is the product of excellent teamwork in the hot electron-group. I would like to thank Lasse Thomsen for great collaboration throughout the whole project. I appreciate his enthusiasm, skills and good sense of humor. I further thank Søren Vendelbo, Robert Jensen and Martin Johansson for the collaboration. I have enjoyed being a part of this group. I also appreciate the collaboration with the hot electron theoreticians Thomas Olsen, Jeppe Gavnholt and Jakob Schiøtz.

Without the commitment and enthusiasm of the highly skilled precision mechanics at the institute work shop H.C. Sørensen and Dan Shacham, and lately also Peter Christensen, we would not have come far in this project. It has been great interacting with them on the development of new equip-

ment and I appreciate their nice solutions and clever inputs to our very diverse UHV problems. Also John Larsens help and experience in UHV related matters are highly appreciated.

I further thank all the very professional process technicians and engineers in the Danchip cleanroom for their readiness to help and share their experience. Especially Yvonne Gyrsting, but also Helle Vendelbo and Conny Hougaard deserve mentioning.

The great working environment at CINF has made these now four years as a Ph.D. student a great time. Everyone has contributed to the good spirits and many fruitful discussions have taken place.

Last, but certainly not least, I thank my husband Jesper Liltorp Mortensen for his support, his endless believe in me, and his patience with me and as a father. Getting a child is great and has put some perspective on life and surface science. But unlike surface science it is a project were progress is a sure thing, sometimes even on a daily basis.

Gunver Nielsen
Kgs. Lyngby, 10th of September, 2009

Abstract

The title of this thesis is "Production of Hot Electrons for Enhancement of Surface Reactivity". Metal-Oxide-Semiconductor (MOS) devices have been designed and fabricated for exploration of their applicability for Hot Electron Femtochemistry at Surfaces (HEFatS). The MOS devices have ultralarge active areas of 1 cm^2 and consist of an n-doped Si substrate, an ultrathin ($\sim$55 Å) thermally grown SiO_2 layer and an also very thin metal film, for example 5-7 Å Ti/70 Å Au or 200 Å Pt depending on their use. Current-voltage characteristics of the devices confirm Fowler-Nordheim tunneling through the oxide barrier and high quality of the oxide. Energy-resolved spectra of electrons emitted to vacuum from Au devices show that a major part of the emitted electrons have lost no or very little energy during transport through the metal layer. The spatial distribution of the emitted electrons shows variations on the 50-100 μm scale, possibly surface related, but is otherwise homogeneously distributed across the whole device area. These emission characteristics make the devices well-suited for inducing reactions on the metal surface.

The effect of depositing Cs in a controlled manner on well-characterized and clean Au devices has been investigated by surface sensitive methods. The work function decreases with increasing Cs coverage, and the onset-energy of emission is seen to follow the work function. Unfortunately the devices break down rapidly and at low bias voltages after Cs deposition.

CO adsorption on the surface of clean Pt devices has been studied, and it shows that adsorbed CO is very stable at room temperature, and that CO can be dosed to saturation and thermally desorbed with very reproducible results. Experiments with direct measurement of hot electron induced CO desorption or the quantification of the amount of induced desorption after prolonged hot electron exposures have yet not been sensitive enough to prove the occurrence of HEFatS. For still unclarified reasons O_2 does not adsorb on the clean surfaces of Pt devices, so the oxidation of CO could not be tested.

Resumé

Titlen på denne afhandling er "Fremstilling af Varme Elektroner til Forøgelse af Overfladereaktivitet". Metal-Oxid-Halvleder (eng. fork. MOS) komponenter er blevet designet og fremstillet med henblik på at undersøge deres anvendelighed til Varm Elektron Femtokemi på Overflader (eng. fork. HEFatS). MOS komponenterne har meget store aktive arealer på 1 cm^2 og består af et n-doteret Si substrat, et ultratyndt ($\sim$55 Å) termisk dyrket SiO_2-lag og et også meget tyndt metallag, for eksempel 5-7 Å Ti/70 Å Au eller 200 Å Pt, afhængig af anvendelsen. Strøm-spændingskarakteristikker af komponenterne bekræfter at der foregår Fowler-Nordheim-tunnellering gennem oxidlaget, som er af høj kvalitet. Energiopløste spektre af elektroner emitteret til vakuum fra Au-komponenter viser at størstedelen af de emitterede elektroner har mistet ingen eller meget lidt energi på vejen gennem metallaget. Den rumlige fordeling af emitterede elektroner udviser variationer på skalaen 50-100 μm som sandsynligvis er overfladerelaterede, men emissionen er ellers jævnt fordelt over hele det aktive areal. Disse egenskaber ved emission gør komponenterne velegnede til at inducere reaktioner på metaloverfladen.

Effekten af at deponere Cs på velkarakteriserede, rene Au komponenter på en veldefineret måde er blevet undersøgt med overfladefølsomme metoder. Arbejdsfunktionen falder med stigende Cs-dækningsgrad, og energien hvor elektronemissionen starter følger arbejdsfunktionen. Desværre bryder komponenterne hurtigt sammen ved lave spændinger når der er blevet deponeret Cs.

Adsorberingen af CO på rene Pt-komponenter er blevet undersøgt, og undersøgelserne viser at adsorberet CO er meget stabilt ved stuetemperatur, og at CO kan doseres til mætnignsgraden og desorberes termisk med meget reproducerbare resultater. Eksperimenter hvor desorptionen af CO induceret med varme elektroner måles direkte eller hvor mængden af desorberet CO bestemmes efter længere tids udsættelse for varme elektroner har endnu ikke været følsomme nok til at påvise forekomsten af HEFatS. Af uvisse årsager adsorberer O_2 ikke på de rene Pt komponenter, så CO-

oxidation har ikke kunnet testes.

Contents

1 Introduction **1**

2 Hot Electron Femtochemistry at Surfaces **3**
2.1 A HEFatS Model 3
2.1.1 DIET and DIMET 5
2.2 First Principles Modeling at CINF 5
2.3 Routes to HEFatS 6
2.3.1 HEFatS on Tunnel Structures 6
2.4 Chemicurrents 7

3 Metal-Oxide-Semiconductor Devices **9**
3.1 The MOS Structure 9
3.2 Transport 12
3.2.1 Tunneling 12
3.2.2 Transport through Metal 13
3.3 Tunnel Devices as Electron Emitters 14

4 Fabrication of MOS Devices **15**
4.1 Device Design and Wafer Layout 15
4.2 Process Sequence 16

5 Experimental Methods **21**
5.1 Electrical Measurements 21
5.2 UHV Experiments 22
5.2.1 Sample Holder and Interface 23
5.2.2 Temperature Measurements and Heating 25
5.2.3 Thermally Induced Desorption 26
5.2.4 X-ray Induced Photoelectron Spectroscopy 27
5.2.5 Ion Scattering Spectroscopy 28
5.2.6 Work Function Measurements 28
5.2.7 Electron Emission Detection 29

5.2.8 Cs Deposition 31

6 Results and Discussions 33

6.1 IV-Curves 33

6.2 Electron Emission 37

6.2.1 Electron Emission in Air 37

6.2.2 Electron Emission Spectra 38

6.2.3 Spatially Resolved Emission 39

6.3 Cleanness of Metal Surfaces 43

6.3.1 Au Cleaning 44

6.3.2 Pt Cleaning 46

6.3.3 Interpretation of Additional Features in ISS Spectra . 47

6.4 Cs on Au 50

6.5 CO and O/O_2 on Pt 57

6.6 Discussion of Systems for HEFatS 62

7 Conclusion and Outlook 65

7.1 0utlook 67

A RCA Clean 69

Bibliography 71

List of Symbols 81

List of Abbreviations 83

List of Papers 85

Included Papers

Chapter 1

Introduction

Heterogeneous catalysts are very important in the chemical industry. The energy required to overcome the inherent energy barriers of the process is provided thermally by increasing the temperature, which can be rather energy demanding and even push the equilibrium of exothermic reactions towards the reactants. A prominent example of this is ammonia synthesis [1]: The rate limiting step is the dissociation of N_2 which is strongly bound so a rather reactive catalyst is needed to break the bond. A reactive catalyst will however also bind the adsorbed atomic N strongly, leaving no free sites for further reactions, hence the temperature is increased to overcome the desorption barrier. At the high process temperature needed, the equilibrium constant is so low, that very high pressures are needed to get decent amounts of ammonia.

This example also nicely illustrates Sabatier's principle [2], which cannot be circumvented in thermal catalysis: The activation energy of a catalytic reaction is correlated with the binding energy of the reactants and products to the catalyst, so a reactive catalyst will yield high reaction rates but will also tend to poison itself, whereas a more noble catalyst will not be able to induce the reaction in the first place.

In the hot electron-group at CINF we want to do catalysis differently, namely by non-thermal, electronic excitations of the reactants adsorbed on a catalyst. It has been proposed, that energetic ("hot") electrons originating from beneath the surface of a substrate and injected into empty states of adsorbed molecules can induce reactions, a phenomenon referred to as Hot Electron Femtochemistry at Surfaces [3; 4]. It has further been suggested, that solid-state tunnel structures could act as tunable narrow band hot electron sources for reactions on the surface of the top metal electrode [4]. This approach to catalyzing chemical reactions holds the possibilities of better energy efficiency, since energy can be directed into the reaction coordinate

at room temperature, and selectivity, due to the tunability of the hot electron energy.

The aim of our work has been to design and fabricate tunnel structures and test their performance in HEFatS under Ultra High Vacuum (UHV) conditions. Our tunnel structures are Si/SiO_2-based Metal-Oxide-Semiconductor (MOS) devices. Parallel to the efforts on realizing HEFatS, we have explored the ways of utilizing these devices as hot electron emitters. With help from the Patent Office at DTU we investigated the possibilities for patenting, but the inventive step from earlier patents was not high enough. Collaboration with several other research groups has been initiated during the project with the aim of utilizing our devices in various experiments, these experiemnts have however not led to any specific results yet.

The outline of this thesis is as follows: In Chapter 2 a general introduction to the mechanisms of HEFatS is given, and the main routes to achieving it are discussed. Then follows an introduction to MOS devices in Chapter 3. Chapter 4 concerns the design and production of devices in this project. The experimental setup for electrical measurements as well as the UHV chamber and its equipment are described in Chapter 5, and the various experimental methods are discussed. Chapter 6 presents results obtained during the project and discusses their implications. The main subjects are electrical device characterization, electron emission characteristics, methods developed for obtaining clean surfaces for surface scientific studies, as well as the study of Cs on Au covered devices, and CO and O on Pt covered devices. Finally conclusions and an outlook for further UHV studies will be given in Chapter 7. Papers which I co-authored are referenced by capital letters as listed in List of Papers on page 85.

Chapter 2

Hot Electron Femtochemistry at Surfaces

The concept Hot Electron Femtochemistry at Surfaces (HEFatS) refers to reactions occurring at surfaces upon interaction with energetic electrons from below the surface. In order to be able to interact with unoccupied energy levels of the adsorbates, the electrons should typically have energies of a few to several eV which in temperature would correspond to tens of thousands of K, hence the appellation "hot" electrons. The term femtochemistry refers to the timescale of femtoseconds which is typical for these reactions.

This chapter will introduce the principles of HEFatS in the conceptual picture proposed an treated by Gadzuk in his comprehensive contribution to the field. Some results from the theoretical hot electron group at CINF will be presented. Furthermore, the various approaches to exploring HEFatS will be summarized, and the related topic of chemicurrent detection will be touched upon.

2.1 A HEFatS Model

An easily comprehensible picture of hot electron induced desorption from surfaces is that of inelastic electron scattering via a negative-ion resonance state [3–5]. The concept can be picturised by transitions between the potential energy surfaces of the molecular ground state, V_0, and of the excited, negative-ion potential, V_-, shown in Figure 2.1. An energetic electron of energy $E_{\rm in}$ in resonance with an unoccupied level in an adsorbed molecule or atom might hop on to the adsorbate, in that way creating a temporary negative ion. This negative-ion will now find itself attracted to the surface by the image force or in other words it is displaced from the equilibrium of the negative-ion state potential, V_-. The negative ion will start oscillating

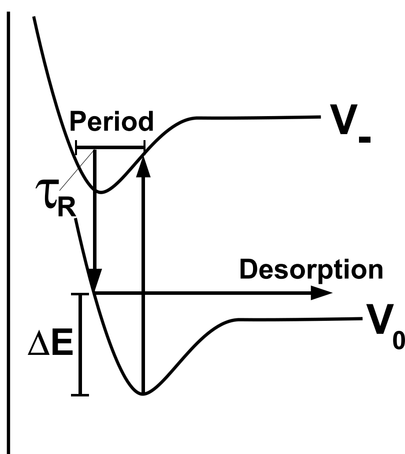

Figure 2.1: Illustration of the mechanism for hot electron induced desorption in the picture of Gadzuk [5]. Initially the adsorbate is at the bottom of the ground state potential energy curve, V_0, and then it is excited to the negative-ion excited state shown as V_- by a hot electron in resonance. It will now feel the image force towards the surface, or in other words be vibrationally excited in the negative-ion state. After a certain residence time, τ_R, the electron tunnels back again and the molecule returns to the electronic ground state. In the case shown, the residence time is so that the molecule returns to an unbound state and desorbs. Or equivalently: the electron has left the energy ΔE in the molecule which is larger than the energy needed for desorption.

under the influence of the image force, and after a residence time τ_R the electron will tunnel back into the substrate with energy E_fin, $E_\mathrm{fin} \leq E_\mathrm{in}$. The adsorbate will have gained the energy $\Delta E(\tau_\mathrm{R}) = E_\mathrm{in} - E_\mathrm{fin}$ which depending on τ_R might be high enough for the adsorbate to desorb. This means that the lifetime of the negative ion in conjunction with the vibrational period of the excited state determine the probability of desorption once the adsorbate has been excited. The resulting overall desorption rate further depends on the energy distribution of the hot electrons and the probability of exciting the adsorbate in the first place.

This theoretical model can be extended to also involving the internal degrees of freedom of the molecule [6] and in that way probabilities for bond breaking inside the molecule (dissociation) can be assessed. The potential energy curves of potential energy vs. adsorbate-substrate distance are then replaced by potential energy contour plots on a plane spanned by the adsorbate-substrate distance and the interatomic spacing.

2.1.1 DIET and DIMET

The picture described above is applicable to the Desorption Induced by Electronic Transitions (DIET) regime, where a single electron induces the desorption event. In cases where the hot electron intensity impinging on the surface is very high, the regime of DIMET, where M is for Multiple, is entered [7]. In that case excitations will occur as described above, but subsequent excitations can occur so rapidly that the ground electronic state will be vibrationally more and more excited. For DIMET the residence time of the electron is not crucial but the rate of excitations is. Working with tunnel structures for creating the hot electrons we will definitely be in the DIET regime, whereas femtosecond-laser pulse excitation can induce DIMET.

2.2 First Principles Modeling at CINF

At CINF HEFatS are being studied not only experimentally but also theoretically [8–10]. This group (Thomas Olsen, Jeppe Gavnholt and Jakob Schiøtz) has developed a modification of the Δ Self-Consistent Field (ΔSCF) method and been successful in calculating excited state potential energy surfaces and predict trends in desorption rates in HEFatS [8; 9]. ΔSCF is an extension to Density Functional Theory (DFT) which is a first principles method based on electron densities which has had great success in predicting trends in interatomic bond lengths, energies, barriers etc.

They model N_2 on Ru and both CO and NO on various transition metal surfaces [8; 9]. Their results show, that the largest displacement of the excited electronic state compared to the ground state is in the interatomic distances. This can be explained by the increase in the center-of-mass distance due to the prolonged molecular bond which counteracts the influence of the image force, but this internal stretch can perfectly well induce desorption. The desorption rates on four different metals decrease in the following order: Pt>Rh>Ru>Pd for CO and Pt>Pd>Rh>Ru for NO. A very important result is that electrons with an energy approximately half the desorption energy higher than the resonance energy give the highest desorption probability. In that way the electron is "the most" in resonance with the adsorbate state both for the excitation and the de-excitation. The de-tuning of the CO-level of energy 3.9 eV on Pt is found to be 0.6 eV, meaning that excitation with 4.5 eV electrons yields the highest desorption probability [9]. These predictions are very valuable to us when designing experiments.

2.3 Routes to HEFatS

There are various ways in which hot electrons for HEFatS can be produced. For surface reactions driven by laser-excitation of the substrate, the adsorbate excitation was proven to be mediated by the sea of hot electrons excited by the pulse [11]. It is the most studied approach to HEFatS and for high laser-fluences works in the DIMET regime. The development of femtosecond-lasers has made time-resolved desorption measurements possible [12; 13] and has provided important temporal information on HEFatS.

Another approach to transferring hot electrons or holes to an adsorbate is by means of a Scanning Tunneling Microscopy (STM) tip. Such experiments give detailed information of the energy necessary for inducing reaction and they can further provide spatial information about surface reactions by for instance mapping out destinations of reactions products [14; 15]. Finally hot electrons for HEFatS can be generated in tunnel structures as described in the section below.

2.3.1 HEFatS on Tunnel Structures

The application of tunnel structures as the source for hot electrons for HEFatS is not new, the works presented in the literature are however countable. The first experiments were conducted in the beginning of the 1970's by Haidinger et al. who observed acceleration of the decomposition of formic acid [16] as well as the selective oxidation of propene [17] on Au by hot electrons generated in their Au-Al_2O_3-Au Metal-Insulator-Metal (MIM) tunnel structures, operated in a batch reactor. They further filed a patent on the process [18]. There is some ambiguity to the actual energy of the electrons, but the idea behind it is sound. For unknown reasons this work is not mentioned in any of the later publications within the field.

More than twenty years later reports on HEFatS on tunnel structures again appeared. Sharpe, Palmer et al. decomposed chloroform and other chlorinated hydrocarbons in the gas phase by means of hot electrons from a MIM device [19; 20]. Wadayama et al. deposited films on top of MIM devices of 2-methyl-1,4-naphthoquinone [21] and p-nitrobenzoic acid [22] and by optical spectroscopies they observed enhanced decomposition when the films were exposed to hot holes (former) or hot electrons (latter). The exact mechanism is however not entirely clear. Studies of the effect of hot charge carriers in electrochemical systems have also been investigated. H_2 evolution in liquid phase water by means of hot electrons from MIM devices has been reported, see for instance [23; 24]. It is our hope to be able to

make HEFatS with adsorbates on well-characterized surfaces under UHV conditions applying surface scientific characterization methods.

2.4 Chemicurrents

A different, but closely related topic within the field of non-adiabatic surface reactions which deserves mentioning is the detection of so-called chemicurrents. This is essentially the opposite phenomenon of HEFatS where exothermic reactions on surfaces excite electron-hole pairs inside the metal film of a tunnel structure. These hot electrons (or holes) can then be detected on the other side of the barrier as a chemicurrent. This was first accomplished with the adsorption of thermal H and D atoms on top of a Ag/Si Schottky diode [25]. Subsequently many other reactions have been studied for instance the adsorption of various gasses [26] and the oxidation of CO [27], also on Schottky diodes. Metal-Insulator-Semiconductor devices have also been applied and look promising for distinguishing different reactions by varying the device bias voltage [28].

Chapter 3

Metal-Oxide-Semiconductor Devices

Our approach to producing hot electrons relies on a tunnel structure consisting of a thin dielectric layer sandwiched between two layers of conducting material. When a bias voltage is applied between the two conducting layers, charge carriers will be able to tunnel through the insulating layer, gaining kinetic energy proportional to the applied bias voltage. Such tunnel devices could be based on a Metal-Insulator-Metal (MIM) structure or a Metal-Insulator-Semiconductor (MIS) structure, the main requirement being a very thin, high quality insulator in order to achieve decent tunnel currents and avoid breakdown under the high applied fields.

For the HEFatS project, a Metal-SiO_2-Si based structure has been chosen, since SiO_2 has a high breakdown field strength and films of high quality can be grown by thermal oxidation of Si. Furthermore, we can benefit from the proximity of cleanroom facilities and large expertise in the field. MIS devices based on Si and SiO_2 are generally referred to as Metal-Oxide-Semiconductor (MOS) devices, and this term will be adopted for the remainder of this thesis. This chapter first describes the electrical properties of the MOS structure, then a brief discussion of the parameters important for electron transport follows and finally the application of tunnel structures as free electron emitters is discussed.

3.1 The MOS Structure

The MOS structure consist of a Si substrate, a thin, thermally grown SiO_2 film and a thin metal film, each material defined by their characteristic energy levels relative to the vacuum level as depicted in Figure 3.1a [29][1].

[1]This presentation was adapted from [29] but could follow any textbook on semiconductor devices.

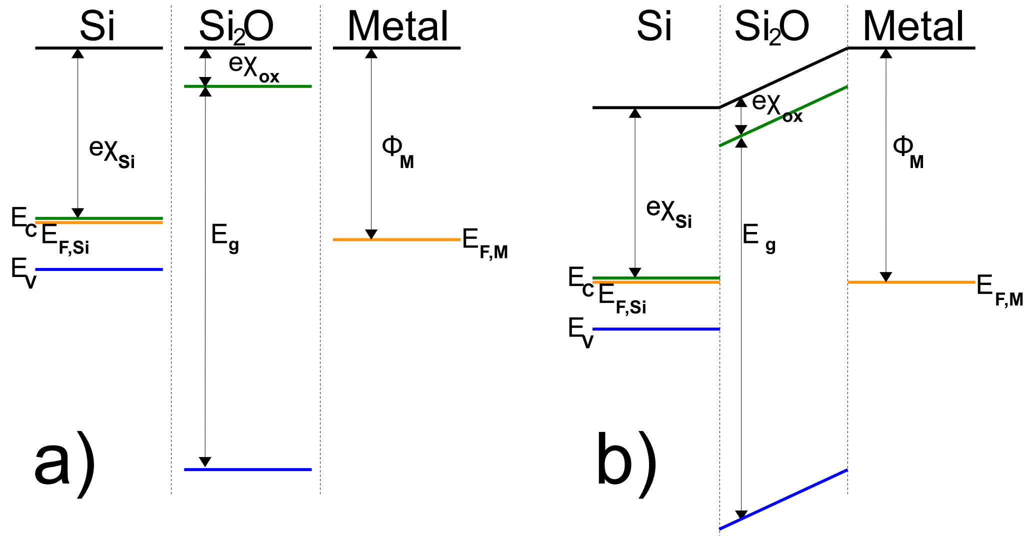

Figure 3.1: a) Band diagrams of the individual layers of a MOS structure, the reference level being the vacuum level (black). Si and SiO_2 are characterized by the electron affinity χ and the band gap E_g which determine the positions of the valence band E_V (blue) and conduction bands E_C (green). In Si the doping density determines the position of the Fermi level E_F (orange). In the metal, here exemplified by Au, the work function Φ_M determines the position of E_F (orange). b) Band diagram of the MOS structure at zero applied gate voltage V_g, where the Fermi level is constant throughout the structure, which leads to a non-zero field in the oxide due to the difference between χ_{Si} and Φ_M (band bending in Si is not shown).

For the metal, the relevant parameter is the work function, Φ_M, which defines the position of the Fermi level, $E_{F,M}$. Here the metal is exemplified by Au, Φ_{Au}= 5.4 eV [30][2]. The oxide is characterized by the electron affinity χ_{ox} which is 0.9 V for SiO_2, and the band gap E_g which is ~9 eV, and from these the positions of the valence and conduction bands follow, the band edges are denoted E_V and E_C, respectively. For Si we have χ_{Si} = 4.01 V and E_g = 1.12 eV. The Si substrate is n-type, heavily doped with Sb to a doping density of N_d ~3×10^{18} cm^{-3} in order to reduce the ohmic resistance, so the Fermi level, $E_{F,Si}$, is positioned 0.06 eV below the conduction band in the bulk[3].

When the three materials are connected and the MOS device is shorted,

[2]Work functions Φ are given in the units of energy (eV) for later convenience.

[3]$E_C - E_F = k_B T \ln N_C/N_d = 0.06$ eV, k_B is the Boltzmann constant, T the absolute temperature (room temperature) and $N_C = 2.8\times10^{19}$ cm^{-3} the effective density of states in the conduction band.

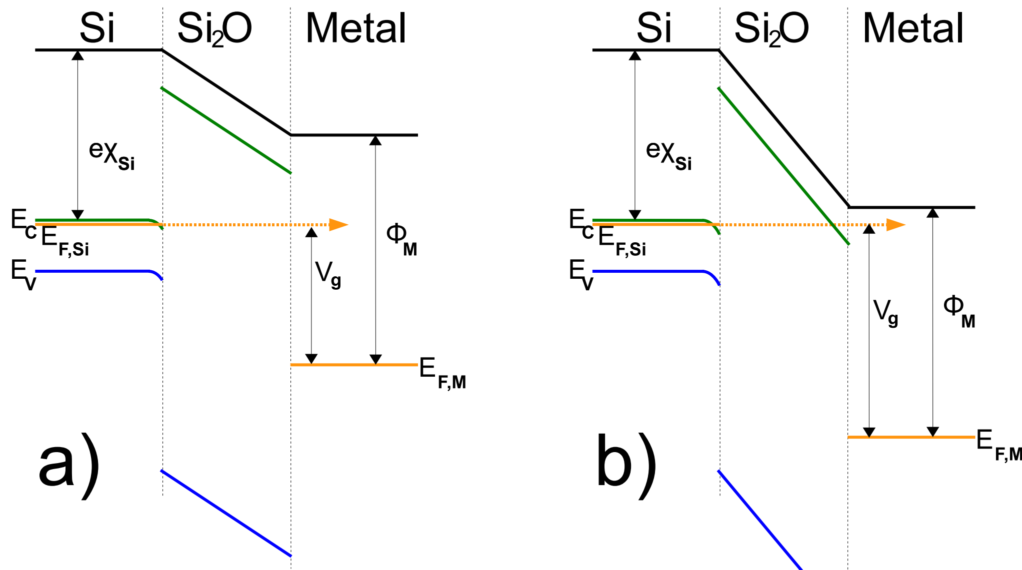

Figure 3.2: Band diagrams of the MOS structure with an applied positive gate voltage V_g. Electrons accumulate at the Si-SiO_2 interface, which leads to band bending. a) Electrons tunnel across the oxide and directly into the metal, direct tunneling. b) Electrons tunnel into the conduction band of the oxide, Fowler-Nordheim tunneling. Symbols as in Figure 3.1.

or in other words a gate voltage of $V_g = 0$ V is applied, the Fermi levels of Si and the metal will line up as shown in Figure 3.1b. This introduces a voltage drop across the oxide, equal to the difference between Φ_M and χ_{Si}. Applying a gate voltage of this magnitude but of opposite sign will lead to flat bands (no fields) in the MOS structure. Hence the flat band voltage, V_{FB}, can be defined as: $V_{FB} = \Phi_M/e - \chi_{Si}$. Trapped charge in the oxide is neglected, but would lead to an additional constant term. Since only transport of electrons into the metal is of interest here, only the case of a positive bias voltage applied to the metal film will be treated. Figure 3.2a and b depicts the band diagrams of the MOS structure under an applied positive gate bias voltage. Electrons are attracted to the semiconductor-oxide interface, therefore an accumulation layer is build up, which has a voltage drop across it, the so-called surface potential, ϕ_S. This effect is indicated by the band bending in Figure 3.2. The applied gate voltage will therefore be divided into three components, so that $V_g = V_{ox} + \phi_S + V_{FB}$, where V_{ox} is the voltage drop across the oxide.

IV (current-voltage) and CV (capacitance-voltage) measurements are valuable when evaluating the electrical and physical properties of the MOS devices, these are treated in [C]. A MOS device can be viewed as a capacitor with capacitance C_{MOS}, which again can be modeled as two capacitors

in series, one due to the oxide itself, C_{ox}, the other due to the accumulated charge in the accumulation layer, C_{S}, so that $(C_{\text{MOS}})^{-1} = (C_{\text{ox}})^{-1} + (C_{\text{S}})^{-1}$ (again neglecting trapped charges in the oxide). In the next section transport phenomena of relevance to IV and emission characteristics will be discussed.

3.2 Transport

Electrons originating from the conduction band of Si must traverse the whole MOS structure before they can end up at the metal-adsorbate or metal-vacuum interface, ready for interaction or emission. Here tunneling across the oxide and transport through the metal will be treated in a little more detail.

3.2.1 Tunneling

As depicted in Figure 3.2a and b, depending on the gate voltage applied, electrons will be able to tunnel through the whole oxide layer and directly into the metal, referred to as direct tunneling, or at higher gate voltages, they will tunnel into the conduction band of the oxide, this condition is known as Fowler-Nordheim (FN) tunneling. Onset of FN tunneling will occur at a gate voltage of $V_{\text{FN,on}} = \Phi_{\text{M}}/e - \chi_{\text{ox}}$, as seen from the geometry of Figure 3.2. Originally, Fowler and Nordheim [31] modeled field emission from a metal, assuming the Fermi-Dirac distribution of a free electron gas as the supply function and calculating the transmission coefficient for a triangular barrier applying the WKB (Wentzel-Kramer-Brillouin) approximation [32]. They arrived at an expression for the current density of the emitted electrons, J_{FN}, which in an updated terminology [33; 34] reads

$$J_{\text{FN}} = A F_{\text{ox}}^2 \exp\left(-\frac{B}{F_{\text{ox}}}\right) \tag{3.1}$$

with

$$A = \frac{e^3}{16\pi^2\hbar}\frac{m_{\text{Si}}}{m_{\text{ox}}\phi_0} \quad \text{and} \quad B = \frac{4\sqrt{2m_{\text{ox}}}}{3e\hbar}\phi_0^{3/2} \tag{3.2}$$

where F_{ox} is the electric field in the oxide, $F_{\text{ox}} = V_{\text{ox}}/t_{\text{ox}}$, t_{ox} being the oxide thickness, e is the electron charge magnitude and m_{Si} and m_{ox} are the electron effective masses in Si and in the oxide, respectively. ϕ_0 is the barrier height seen by a Fermi level electron in Si, so in this case we have $\phi_0 = \chi_{\text{Si}} - \chi_{\text{ox}} + (E_{\text{C}} - E_{\text{F}})/e = 3.17$ V. An FN-plot (or Fowler-plot),

$\ln(J/F_{ox}^2)$ vs. $1/F_{ox}$, yields a straight line if the electrons have tunneled by this mechanism.

Of course this classic formulation results from too simple models of the barrier and the supply function. Taking into account that the barrier is not triangular, but rounded off due to the image charge of the electron [35], and further introducing the actual distribution of electrons at the interface result in two correction parameters or functions, one for each of the two constants A and B [33; 34; 36]. This yields better quantitative agreement with experiment but is much more involved, so the qualitative agreement usually obtained for low temperatures by the original expression will suffice for our purpose [35–37].

3.2.2 Transport through Metal

For the application of MOS devices for HEFatS or as free electron emitters as discussed below, the energy distribution of the electrons at the metal-vacuum interface is important. Scattering events between an electron traveling through the metal and either metal electrons, phonons or scattering potentials due to imperfections are responsible for energy losses or attenuation of the emitted current. The occurrence of these events is statistical in nature, hence an exponential decay of the emission current I with metal thickness t_M is expected

$$I = I_0 \exp\left(-\frac{t_M}{\lambda}\right) \tag{3.3}$$

characterized by an electron mean free path λ, see for instance [38; 39]. At electron energies a few eV above the Fermi level or higher, electron-electron collisions dominate, and the mean free path for such events is highly dependent on the electron energy and varies strongly from metal to metal [39–41]. Effects from the amount of defects due to e.g. crystallite sizes in the metal film can also not be neglected [38]. The metal film used in the devices should consequently be as thin as possible in order to minimize losses. The dependence of metal film thickness of both Au films and the necessary Ti wetting layer on electron emission efficiency is investigated and discussed thoroughly in [B], and some results are presented in Section 6.2.1.

3.3 Tunnel Devices as Electron Emitters

By applying a device bias voltage a little higher than depicted in Figure 3.2b, tunneling electrons will have gained an energy higher than the vacuum level of the metal, and can therefore escape the work function of the metal and be emitted to vacuum. The operation of MIM devices as free electron emitters was first demonstrated in 1961 [42], and since then their characteristics have been studied extensively in terms of IV-characteristics and energy-resolved emission spectra, for instance [43–46]. The main advantage of this type of electron emitter is the robustness in the presence of gas, since high electric fields are only present inside the device, in the solid state. The pressure insensitive operation has been proven by other groups [47; 48] and studied as part of the HEFatS project [B].

The main drawback of the MIS or MIM electron emitter is the relatively low emission current density which can be achieved, and a lot of studies have concerned the improvement of this. One way to do this is to lower the work function of the top metal film by deposition of for instance Cs which increases the emission current by orders of magnitude [49–51], an effect also studied in the HEFatS project and reported in [B,C] and Section 6.4. As discussed in the previous Section 3.2.2, the metal film should be as thin as possible, but as already pointed out by Mead [42] this can lead to serious voltage drops across the surface of the emitter and consequently lower emission currents. Very rough metal films, even with small holes and cracks, provide spots of high emissivity [46; 52]. This can be refined by a very thin metal layer and a fine metal grid upon that [53]. The general picture, however, is that the absolute maximal transfer ratios (emission current/total transmitted current) are about 10 % and in general much lower, and the absolute values are low.

The homogeneous and highly directional emission of electrons over large areas is another very interesting property of the tunnel emitters which is utilized for Hot Electron Emission Lithography (HEEL), where a tunnel device is patterned so that it both serves as electron source and mask [54]. Easy integration with other Si-based components have made MOS emitters attractive for flat panel displays [55] and high-sensitivity image sensors [56].

The possible applications are numerous, for instance in the ionization unit of mass spectrometers as has been demonstrated by Paolo Malacrida and Martin Johansson within the HEFatS project. In Chapter 6 of this thesis, emission-IV characteristics, electron emission spectra as well as spatially resolved emission characteristics will be treated.

Chapter 4

Fabrication of MOS Devices

The MOS devices are fabricated in the cleanroom facilities at Danchip A/S at DTU. Each step in the fabrication process is a well-established standard procedure, and the large extend to which devices can be parallel-processed is highly advantageous. A new batch starts out with 25 Si wafers, each encompassing 20 devices, and along the process, smaller sub-batches can be taken out and processed further. The design as well as the process sequence were developed during the first months of the HEFatS project in 2005, and the essence of both has remained, but the gathered experience has led to a number of valuable updates.

4.1 Device Design and Wafer Layout

The ultimate application of the MOS devices for HEFatS in UHV places some requirements on their design. First of all, the size of the total active area of each device should be suitable for the surface science techniques employed, including the methods used for detecting products of hot electron induced reactions. The size chosen is a square of side length 1 cm. Furthermore, the devices will be transferred into UHV and electrical connections to the front and the back must be established, so the design also involves a sample holder in which the device can be transferred and a sample holder interface inside the UHV chamber, both of which will be discussed in Section 5.2.1.

A schematic top-view and cross-section of a single device is shown in Figure 4.1. A rectangular frame of thick SiO_2 ($\sim$750 nm) around the thin tunnel oxide serves as a mechanically stable underlayer for the top metal film in the area where the electrical contact is made, and it protects the device during handling.

Figure 4.2 shows the layout of a wafer with 20 devices and a number

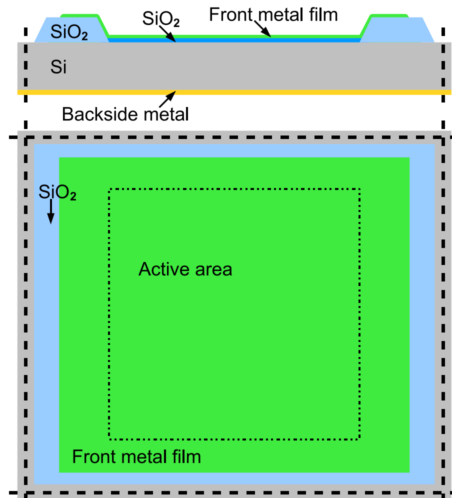

Figure 4.1: The structure of a device shown in cross section (above, not drawn to scale), and in top view (below).

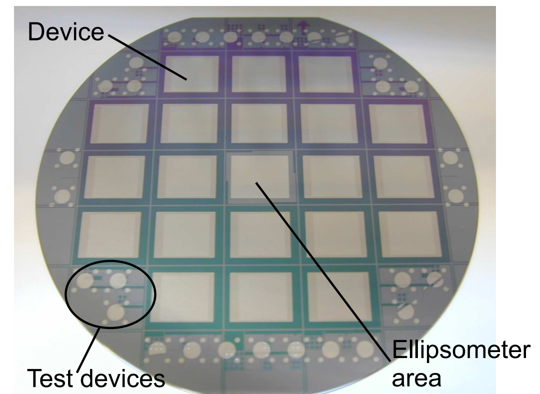

Figure 4.2: A processed Si-wafer with 20 devices, an ellipsometer area and several test devices.

of smaller test devices with areas ranging from 10^{-5} to 0.1 cm^2. The device in the center has no thick oxide frame and therefore provides a larger thin oxide area where the tunnel oxide thickness can be measured with an ellipsometer.

4.2 Process Sequence

This section will present the process sequence for fabricating the MOS devices step-by-step.

Silicon substrate

The Si substrates chosen for producing MOS devices are n-type, heavily doped with Sb to give a very low resistivity, less than 0.02 Ωcm. The wafers are single side polished with the (100) plane exposed and they have a diameter of 100 mm and a thickness of 525 μm. This orientation allows us to dice the wafer into individual devices by cleaving it along the (110) planes. Furthermore, the Si/SiO_2 interface in the [100] direction, shows superior electrical characteristics due to a minimum of defects [57].

Thick protection oxide

An oxide of approximately 750 nm thickness grown by wet thermal oxidation serves as a stable underlayer for contacting the front of the devices. Oxidation is done in a drive-in furnace at 1000°C in water vapor for 180 min followed by annealing at 800°C in N_2 for 20 min. The precise thickness is measured in order to predict the etching time in the following step.

Active area etch

The active area of 1×1 cm^2 is defined by etching away the thick oxide in a 5 % buffered HF (bHF) solution. The thick oxide to be retained is masked with photoresist. The etch rate of SiO_2 is ~80 nm/min. Overetching will lead to roughening of the Si surface which could lower the quality of the thin oxide and therefore the progress of the etching is followed closely. This can easily be done by visual inspection since SiO_2 is hydrophillic and Si is hydrophobic. After ~9 min of continuous etching the wafers are in turn lifted from the bath for inspection and etched for a short time until the surface becomes hydrophobic. Finally the photoresist is stripped in acetone.

Figure 4.3: Device after etching, before stripping the resist mask.

Thin oxide

Prior to the thin gate oxide growth, the wafers are cleaned by a standard RCA clean [58] including HF dips, the details are given in Appendix A. Contamination of the Si surface will affect the oxide growth rate and thereby the oxide quality, so oxidation is done in a dedicated drive-in furnace which is kept very clean by imposing severe restrictions on its use. Oxidation proceeds at 800°C in dry O_2 for 20 min followed by an anneal at 800°C in N_2 for 20 min. The wafers should be removed from the furnace immediately after the process has terminated, since small amounts of O_2, and maybe also water vapor, continue to oxidize the Si at the elevated idle temperature of the furnace (600°C). This leads to a thicker oxide of poorer quality, as may be seen from electrical measurements.

Figure 4.4: Device where the thin tunnel oxide has been grown.

Usually 10-15 wafers are processed in this step. Three blank wafers are placed at each end of the device wafers in the fused silica boat which goes

into the furnace. The growth rate and therefore also the resulting oxide thickness is critically dependent on the O_2 flow over each wafer, and this varies through the furnace, the most at the ends. The thickness of the oxide is measured on each wafer with ellipsometry, and it is seen to vary 5-10 Å around 55 Å.

Early in the project, the possibility of thinning the oxide in a very dilute ($\sim$0.1 %) HF was investigated. With ellipsometry the etch was confirmed to be homogeneous with an etch rate of 1-2 Å/min. In electrical measurements, however, the oxide was seen to have degraded, so this approach was abandoned.

Backside metallization

The native oxide on the backside is removed by a droplet of bHF which gradually etches away the oxide. Immediately after this, the backside metal is deposited by Physical Vapor Deposition (PVD) in one of two available e-beam evaporators, which both have a base pressure of 1×10^{-7} mbar. First a 10 nm thick Ti layer is deposited which serves as an adhesion layer for the 100 nm thick Au layer which is then deposited. Depending on the evaporator employed, this step can be done on a single wafer at a time, or on up to eight wafers.

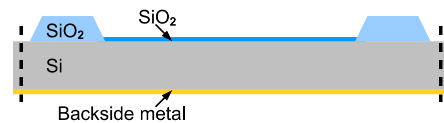

Figure 4.5: Device after backside metallization.

Front metal

The front metal film is deposited in the same e-beam evaporators as the backside contact, only these films are much thinner. Masking is done with a very thin Al shadow mask, which must be positioned very carefully in order not to touch and harm the oxide.

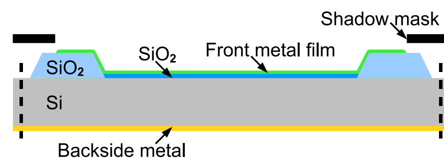

Figure 4.6: Device with front metal film deposited and shadow mask shown.

Masking was for a long time done with photolithography, followed by lift-off in an ultra-sonic acetone bath. This procedure works fine, but when we started surface studies in the UHV chamber, it turned out that the lift-off left vast amounts of organic species on the surface, which was then very hard to clean. The use of shadow masks is less time consuming, and produces much cleaner surfaces, this is further discussed in Section 6.3. The results presented in Chapter6 are primarily from samples with either 10 nm Ti and

100 nm Au, 5-7 Å Ti and 70 Å Au or 200 Å Pt. A wetting layer of Ti (or Cr) is necessary for Au devices, otherwise the Au peels off.

Dicing

The wafers can now be diced into the individual devices. This is done by scribing with a diamond in the lines between the rows of devices. This induces stress and defects in the crystal around the scribing line, enough to allow us to break the wafer when placing the particular scribing line over a sharp edge and applying a small pressure on the unsupported part. Scribing is done on a scribing bench where the wafer can be aligned, and parallel lines automatically scribed. The alignment of both the wafer and the diamond in the bench is critical, and it regularly happens that the wafer breaks at the wrong position and devices thereby are lost.

The original idea was to dry etch 200 μm deep, high-aspect ratio grooves in the wafer instead of scribing, but at this point we had to do it after the top metal deposition, and due to some unresolved problems with the sticking of the photoresist to the metal edges, the wafers where not allowed to go into the etching apparatus. The use of shadow masks for top metal deposition, however, has made it possible to etch the grooves at an earlier stage, so this procedure is currently being tested and it looks promising.

Chapter 5

Experimental Methods

This chapter describes the equipment applied in the various experiments and discusses the experimental techniques in general, and also, when needed, more specific details important for the particular experiment. The intend is to build a basis for evaluating the experimental results obtained and presented in Chapter 6. First the setup employed for electrical measurements in air will be treated, then follows an exposition of the details relevant for the UHV experiments.

5.1 Electrical Measurements

Electrical measurements like IV and CV characterization discussed in Chapter 3 can be performed in air as well as in the UHV chamber. Figure 5.1 shows photographs of the setup employed for measurements in air. One whole wafer or single devices are placed on the rotatable chuck on the x-y-table as seen in the figure. Contact to the front is achieved by lowering the Al plate with the probe(s) by means of a micrometer screw. The position of the probe can be observed through the magnifying optics also shown. The whole setup is encased in a large Cu box which can be closed completely in order to reduce electrical noise pickup, and wiring is done with coax cables as far as possible. The setup can be modified with a positively biased metal plate placed in front of the device, in order to pick up emitted electrons when measuring emission currents in air.

Electrical measurements are performed from a PC with a National Instruments DAQ-card and LabView software, which handles scanning of the device bias voltage and data acquisition. The device bias voltage is set directly from the DAQ-card, which limits the total current to 5 mA. The actual voltage is measured with the DAQ-card with $\sim$0.1 mV resolution. Currents

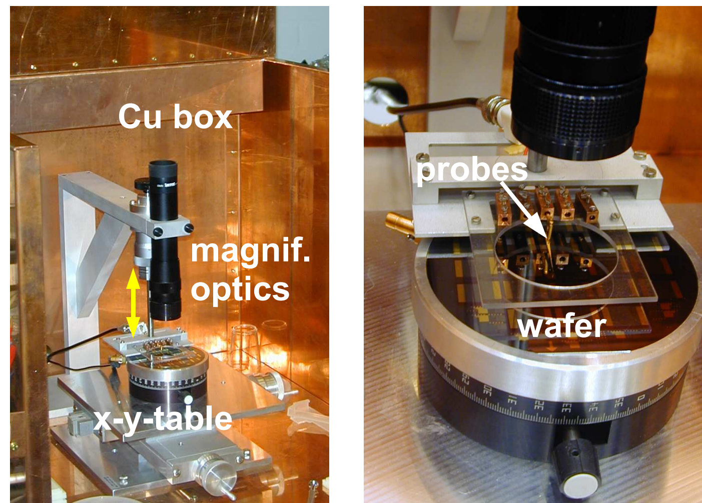

Figure 5.1: Photographs of the setup for electrical measurements in air. The left picture shows the x-y-table and the magnifying optics in full, and the yellow arrow indicates the movement of the arm holding the probes for the front contact. In the background the shielding Cu box is seen. The close-up in the right picture shows a wafer placed on the rotatable chuck and the mounting of the probes.

can be measured by either a Keithley 6485 Picoammeter or a Keithley 6514 System Electrometer, both of which are employed if both transmission and emission currents are measured.

5.2 UHV Experiments

All the surface scientific experiments, including electron emission in vacuum, composing this project are conducted in the same standard Ultra High Vacuum (UHV) chamber. The chamber has a base pressure below 10^{-10} mbar as measured with an ion gauge, and it is pumped by a turbomolecular pump. It further has a Ti sublimation pump, which is operated during night. A schematic overview of the chamber can be seen in Figure 5.2. The available equipment will now be briefly summarized, whereas more thorough descriptions and discussions of the techniques can be found in Sections 5.2.1-5.2.7.

At the center of the chamber is a sample holder interface, into which devices mounted in special sample holders can be transferred via the loadlock and the wobblestick (top of Figure 5.2). The loadlock features a garage with room for 15 devices and is pumped by a turbomolecular pump. The sample holder interface is mounted on a manipulator enabling translation

in all three dimensions, as well as rotation around an axis. Cables from the interface are connected to electrical feedthroughs to the outside.

The UHV chamber has a Hemispherical Analyzer (HSA) of 100 mm diameter (VSW HA100) controlled by a VSW HAC5000 controller, ratemeter and ESCA interface, and an X-ray gun with Mg and Al anodes (VSW Twin Anode X-ray Source) with a VSW control and high voltage supply, the gun being pumped by an ion pump. It further has two identical, differentially pumped ion guns (Perkin Elmer Phi 04-300) with one Perkin Elemer 11-067 Ion Gun controller. Ion gun 1 is mounted with He and Ar through leak valves and ion gun 2 has a leak valve with O_2 for cleaning purposes. A Baltzer 125 Quadrupole Mass Spectrometer (QMS) is mounted on top of the chamber. The original QME 125 high voltage and RF supplies and the preamplifier are used, it is however being controlled by a home-build unit with power supplies and National Instruments DAQ-cards and LabView software (all developed during the project by Lasse Thomsen). A double Microchannel Plate (MCP) with a phosphor screen (Del Mar MCP33-10) is mounted on a holder and arm designed by the institute workshop, so that it can be moved in and out of sight behind a large viewport. The MCP operation is controlled via a homebuild power supply. At the bottom of the chamber three metal evaporators are installed: A Cs-getter (company SAES), a Ti evaporator, and a Pt e-beam evaporator, which is unfortunately very unstable. All the sources are in water cooled housings, behind turnable flags. Further, the UHV chamber has a number of leak valves which allow for dosing various gases: ^{28}CO, ^{29}CO, NO, He, Ar and O_2 where the leak valves for the three latter gases are mounted via the ion guns. The gas bottles and lines are connected via a bakeable gas manifold pumped by a turbomolecular pump.

5.2.1 Sample Holder and Interface

Integrating semiconductor components like MOS devices in UHV experiments is a challenging task. In the first part of the project we focused on device design and subsequent fabrication, as discussed in Chapter 4, along with the design of a sample holder and interface for the UHV chamber, and the construction of a loadlock and a wobblestick. The UHV-related designing was done in close collaboration with the institutes workshop, who also build the equipment. With a few minor updates on the original design, we now have a very robust and well-functioning system. It consists of a simple sample holder on which the device is mounted. The sample holder can sit in the garage in the loadlock, be grabbed by the wobblestick and

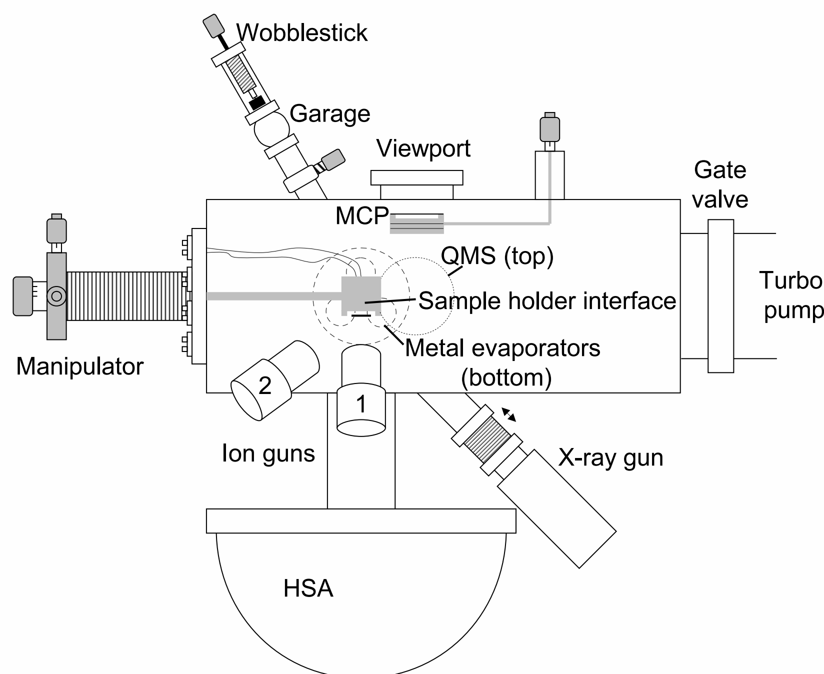

Figure 5.2: A schematic topview of the UHV chamber. In the middle the sample holder interface is depicted, which is mounted on a manipulator enabling translation in three dimensions and rotation around the manipulator axis. Devices mounted in a sample holder can be transferred into the sample holder interface from the loadlock and garage by means of the wobblestick. The UHV chamber further has a Hemispherical Analyzer (HSA) for energy-resolved electron and ion detection, an X-ray gun, two ion guns denoted 1 and 2, a Microchannel Plate (MCP), a Quadrupole Mass Spectrometer (QMS) at the top, and three metal evaporators (Cs, Ti and Pt) at the bottom.

transferred into the sample holder interface in the UHV chamber, where electrical contact can be established.

The sample holder is a thin stainless steel frame, shaped to slide easily into a pair of tracks in the sample holder interface, see Figure 5.3. A hole matches a pin on the wobblestick grab. The device is fixated by two Mo clips, which also serve as the electrical connections to the front metal film. Both the device and the clips are electrically isolated from the frame by small glass pieces, see inset in Figure 5.3. With this design, all connections can be made by spring loaded connector pins located beneath the sample as depicted in the schematic of the sample holder interface in Figure 5.4. The sample holder interface has a movable ceramics and Cu piece which is lifted up against the sample holder by activating an arm with the wobble-

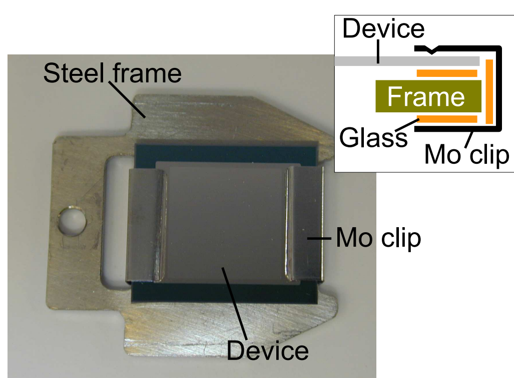

Figure 5.3: A device mounted on a sample holder. The sample holder steel frame, the Mo clips and the device are indicated. The inset shows how the device and the clips are isolated from the steel frame by small 2×10 mm^2, 0.5 mm thick glass pieces (orange).

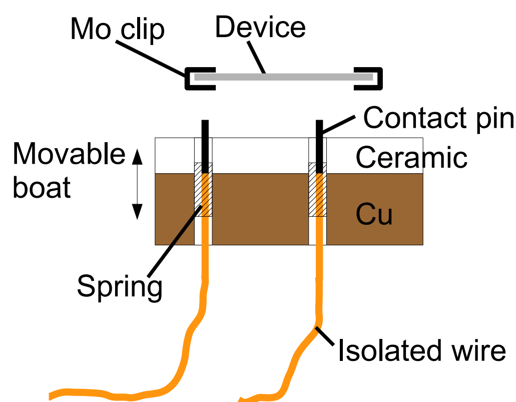

Figure 5.4: A conceptual drawing of the sample holder interface. A boat made of Cu and ceramics holds the spring loaded contact pins (only two are shown) which are connected to feedthroughs to the outside of the chamber by screened, isolated wires. When moving the boat upwards with the wobble-stick by means of an arm (not shown), contact to the device backside and the Mo clips can be achieved.

stick. This piece holds the three connector pins: one for each front contact and one to the backside and additionally a thermocouple which is pressed against the backside. It also has a filament (from a halogen bulb), which can be used for heating the sample. Screened wires from the front and back contact pins lead to electrical feedthroughs with BNC connectors on the outside, so that the device can be hooked directly up to the measuring equipment described in Section 5.1.

5.2.2 Temperature Measurements and Heating

For thermal desorption experiments it is desirable to heat the surface fast in a controlled manner and to record the exact temperature. This is however non-trivial for this system, and we have tested several methods. External heat sources like a filament or a heating button (an encapsulated filament) are inefficient and rather slow, and produces degassing, from themselves as well as the surroundings, which increases the background in the signal from the desorption products. A good way to heat the top metal film fast is to pass a current through it, minimizing heat-up of the surroundings. A more elegant solution would be to heat the device by passing a current

through the metal film on the backside, and a rebuild of the sample holder interface to facilitate this is being considered at the time.

As mentioned, the sample holder interface holds a thermocouple, which in order to be mechanically stable is covered by a small metal cap, that is pressed against the backside of the device. During heating, the front metal film and the thermocouple are far from thermal equilibrium, and the thermocouple readout is therefore not useful for determining the surface temperature.

A clever way to solve this problem is to use the front metal film itself as a resistance thermometer [59], especially in the case of Pt, since Pt has a nice linear temperature-resistance relationship in the temperature interval of interest (0°C-600°C [59]). Progress is done on fully incorporating this measuring method in the setup. After one heating cycle, the film and the contacts are well annealed, and subsequent heating cycles of equal power mostly produce identical resistance-time curves. Sudden jumps in the resistance to another level can appear, most likely due to rapid changes in the contact resistance. To avoid this, it would be advantageous to incorporate extra contacts on the sample holder, so that the voltage drop across the film could be measured on a separate pair of contacts, excluding the contribution from the voltage drop over the contacts, where the current is applied. Still, the temperature measurement will probably need calibration for each device, which can be done when it cools down, and thermal equilibrium between the metal film and the thermocouple can be assumed.

5.2.3 Thermally Induced Desorption

A very powerful tool for assessing the relative amounts of adsorbates on a surface is Temperature Programmed Desorption (TPD): The surface is heated at a constant rate and the desorption products are measured by mass spectrometry as a function of temperature. As long as the heating rate is constant, desorption energies and mechanisms can be determined from the desorption temperature and the curve shapes, respectively [1]. As discussed above, our setup does not allow for controlling the heating in order to obtain a constant temperature ramp (yet). Instead a constant bias voltage is applied, so the experiments discussed in this thesis will be referred to as TID (Thermally Induced Desorption) experiments, not TPD.

For the same reasons as discussed above, we are at the time not able to plot the TID-curves as a function of temperature in a satisfactory way, so they will all be plotted as a function of time. The time delay before heating is turned on can be timed very precisely. TID curves from the same de-

vice can be directly compared, but due to differences in contact resistance, film resistance and probably also small differences in surface morphology, heating rates for different devices will differ, and this influences the exact shape of the TID curves. Relative amounts of desorbate are determined by calculating TID integrals after subtraction of the background. The background level is taken as the mean of 10-20 points of the TID curve just before heating is turned on.

As a heritage from earlier experiments conducted in the chamber, the QMS was mounted with a long Cu snout with an opening of 3 mm in diameter. This is to ensure, that only species desorbing from the sample surface are detected. However, since we are only heating the metal film, we have eliminated other sources of desorbates, and at some point we removed the Cu snout in order to increase our sensitivity. This we were hoping to gain due to a reduced distance from the ionization volume in the QMS to the sample (from $\sim$10 cm to $\sim$3 cm) and a larger solid angle of detection. We did see a reduction in the background level due to an increased pumping speed in the QMS, but only a small increase in the TID signal.

5.2.4 X-ray Induced Photoelectron Spectroscopy

X-ray induced Photoelectron Spectroscopy (XPS) involves the energy resolved detection of photoelectrons excited by a monochromatic X-ray source. The electron transitions excited in the surface atoms produce distinct lines in the recorded spectra, which are unique for the present elements, on top of a background of secondary electrons. The mean free path of electrons in a solid depends on their kinetic energy as well as on the material, and determines the maximum depth from which electrons can escape, and therefore the depth which is probed in XPS. This is typically 5-20 Å, depending on the kinetic energy of the line observed [1; 41].

All spectra presented in this thesis are recorded with the $\mathrm{Mg}_{K\alpha}$ line exposure, which has the photon energy $\gamma = 1253.6$ eV. Intensity spectra of the kinetic energy, E_{Kin}, are recorded with the HSA system. The binding energy, E_{Bind} of an electron can be determined from $E_{\mathrm{Bind}} = \gamma - E_{\mathrm{Kin}} - \Phi_{\mathrm{A}}$, where Φ_{A} is the work function of the analyzer. Using the position of the Au $4f_{7/2}$ line as a reference, Φ_{A} has been determined to be 4.65 eV.

Relative line intensities are determined by comparing line integrals. These integrals are calculated from the raw data using the software CasaXPS which facilitates easy background subtraction. A Shirley background is subtracted from the Au and Pt 4f lines, whereas linear background subtraction is more adequate for the Cs 3d, C 1s and O 1s lines.

5.2.5 Ion Scattering Spectroscopy

In Ion Scattering Spectroscopy (ISS)[1] ions of a known kinetic energy are scattered of a surface and the resulting kinetic energy in a particular direction is measured. A binary elastic collision between the incoming ion and the target atom models the scattering event very well [60], due to a small interaction time. Furthermore, a very high neutralization probability effectively precludes ions from multiple scattering events to be detected. From the conservation of energy and momentum, an expression for the ratio between the outgoing, E_{out}, and incoming kinetic energy, E_{in} can be derived:

$$\frac{E_{\text{out}}}{E_{\text{in}}} = \left(\frac{\sqrt{M_{\text{target}}^2 - M_{\text{ion}}^2 \sin^2\theta} + M_{\text{target}} \cos\theta}{M_{\text{target}} + M_{\text{ion}}} \right)^2 \tag{5.1}$$

where M_{ion} and M_{target} are the masses of the ion and the target atom, respectively, and θ is the scattering angle. We apply He^+ with $M_{\text{ion}} = 4$ amu and $E_{\text{in}} = 1000$ eV, and we have $\theta = 135^\circ$ with detection along the surface normal. The fact, that only singly scattered ions survive, makes ISS one of the most surface sensitive techniques, only probing the topmost layer. A further discussion of the neutralization mechanisms and the interpretation of the ISS spectra is postponed to the treatment of the ISS results in Chapter 6. Exposure of devices to 1 keV He^+ ions during ISS measurements leads to breakdown of the oxide, more details in Section 6.3, so this method can only be applied on devices which are not intended for hot electron experiments.

Relative peak intensities are determined by calculating peak integrals. This is done with the CasaXPS software like the XPS integrals, and a Shirley background is subtracted from the Au and Pt peaks.

5.2.6 Work Function Measurements

The illumination of the device with X-rays produces, besides the high-energy photoelectrons utilized in XPS, a vast amount of secondary electrons at low energy. The work function of the surface, Φ, appears in a kinetic energy spectrum as an energy cut-off below which the electrons cannot escape the surface. Usually the device is biased to -25 V (with the front and back shorted), and then a kinetic energy spectrum around this energy is recorded with the HSA setup. Biasing the device negatively with respect to the analyzer is necessary when the work function of the device surface

[1]Or: Low-Energy Ion Scattering (LEIS)

is lower than the analyzer work function, and furthermore a huge electron signal is detected around 0 eV kinetic energy. Work function measurements can also be performed in the device-analyzer setup applied for obtaining energy-resolved emission spectra as discussed below in Section 5.2.7.

We can only determine the work function relative to the HSA work function which was determined from the position of the Au $4f_{7/2}$ line in XPS as described above. The width of the work function curves, however, makes the determination of absolute work functions meaningless. Work function changes can be extracted in several ways and are sufficient for our purpose. I have chosen the method of making a linear fit to the steep, linear part of the curves and determining the intersection with the energy axis. This method proved to be very robust, and it was seen to yield the same work function changes as when determining the inflection point of the curves from the second derivative.

5.2.7 Electron Emission Detection

Several approaches to investigating the electron emission characteristics of the devices have been implemented in the UHV chamber and applied during this project. This section first describes the measurements of the integrated emission currents, followed by a description of the setup for the energy-resolved emission spectra, and finally the Microchannel Plate (MCP) is treated, by means of which the spatial distribution of the emitted electrons over the surface can be studied. To avoid photoelectrons to be created in the device and obscure the spectra, every viewport on the chamber is blinded and all filaments are turned off during experiments, the latter also prevents the detection of stray electrons.

Integrated Emission Currents

Measuring the total emitted current from the device requires only a very simple setup: A metal plate at a positive bias voltage is placed in front of the device, parallel to its surface, and the plate is connected to ground via an ammeter, which measures the emission current. These measurements can be made both in vacuum and under higher pressures, even in air. In the UHV chamber a Cu plate of 3×3 cm^2 size was applied, which is mounted on the MCP holder, next to the MCP.

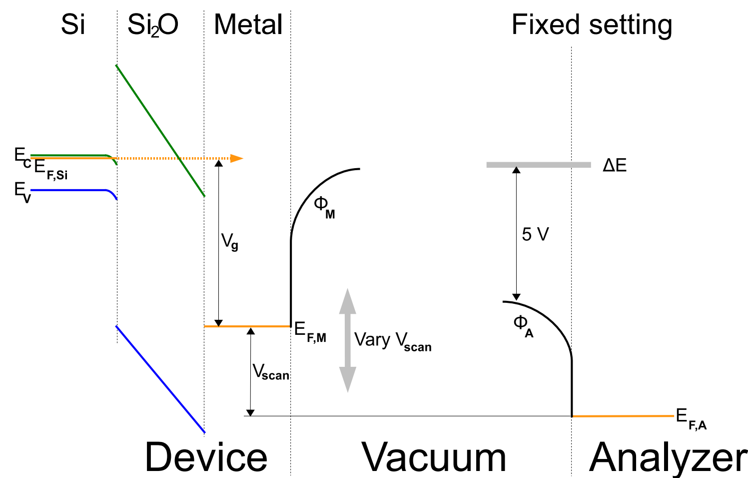

Figure 5.5: Energy diagram showing the principle of obtaining electron emission spectra. The left part shows the device with a constant applied bias voltage of V_g. The HSA to the right has fixed settings and detects 5 eV electrons at a pass energy of 1 eV, as indicated with the acceptance window ΔE. An energy spectrum is obtained by varying the voltage between the HSA end the device, V_{scan}.

Energy-Resolved Emission Spectra

The Hemispherical Analyzer (HSA) is designed for obtaining energy-resolved spectra of charged particles, and is also suitable for recording electron emission spectra. The electronics however are made for detecting the very weak ISS and XPS signals, so we had to set up our own. First of all, the detection from the channeltron is usually done in pulse-counting mode, which due to the strong signal is not applicable, so the channeltron was connected to a high voltage supply with floating output terminals and the current was measured with an ammeter on the ground side. Furthermore, the HSA control has some fixed settings for the pass energy, the lowest of which is 10 eV, but by going even lower, the resolution will be better and the signal will decrease. This was first realized by connecting individual DC voltage supplies to each component in the HSA, the lenses, the shells etc. Later a multipurpose control unit was build incorporating HV supplies and a National Instruments DAQ-card with dedicated LabView software, which is used for both these measurements and for the MCP stack. An additional trick employed is to keep the HSA on a fixed setting, and apply a bias voltage to the device which is scanned to complete a spectrum. The principle is illustrated in Figure 5.5.

The HSA is set up with a retardation potential of -4 V at the entrance and a pass energy of 1 eV, which results in the detection of 5 eV electrons

relative to the analyzer work function, in the very narrow window ΔE shown in Figure 5.5. A negative bias voltage, V_{scan}, on the device is varied, and in that way, an energy spectrum of the emitted electrons can be completed.

Microchannel Plate

A Microchannel Plate (MCP) is a thin plate with a periodic array of very thin channels. Each channel works as a Secondary Electron Multiplier (SEM) when a bias voltage is applied between the metallized surfaces of the plate. The MCP assembly consists of a stack of two MCPs (yields a higher gain, here up to 10^7 in total) and a phosphorous screen. The MCPs are biased by two individual HV supplies, up to 1100 V each, and the screen is biased with a floating terminals HV supply (up to 5 kV), so that the amplified emission current can be measured by an ammeter. It is the same as applied for the HSA channeltron when obtaining emission spectra. Higher voltages can be applied to the screen with a homebuild flyback HV supply, this sharpens the picture when low emission is being recorded. Photographs of the screen are taken with an XGA CCD camera through a $\times 10$ macro lens mounted with a tight collar in order to screen out daylight.

The MCP vendor (Del Mar Ventures, San Diego) states that a single MCP with pore size 10 μm like ours, projected on to a phosphor screen has a typical spatial resolution of 25 μm. It is larger for a double MCP since the higher gain leads to enhanced repulsion and spread-out of the electrons into more channels in the second MCP.

5.2.8 Cs Deposition

Cs is deposited from a commercially available getter source (company SAES) containing a mixture of Cs chromate and a reducing agent which releases Cs atoms when resistively heated. The getter is mounted with electrical connections inside a water-cooled Cu housing. It has a hole in the top which can be covered by a turnable flag for the timing of deposition. The getter was outgassed behind the flag for 2 min before deposition. Typical deposition times were from 30 s and up to 20 min and the driving current was usually 7.2 A. The deposition rate is constant for several hours of deposition, but towards the end of the lifetime of the getter, the current has to be increased.

Chapter 6

Results and Discussions

This chapter presents main results in the many-sided studies conducted as part of the HEFatS project and discusses their practical and scientific implications. First results related to the device functionality will be presented, and this involves IV-characteristics and electron emission studies. Then the prerequisite for surface scientific studies, namely the cleaning and resulting cleanness of Au and Pt surfaces will be discussed. Finally the results obtained so far on the (O-)CO/Pt system are presented and discussed, as are the potentials of other systems in our setup.

6.1 IV-Curves

An IV characteristic is a very simple way to assess the condition of the oxide of a device, whether it has the expected thickness or if it has been damaged or suffered a breakdown, and it can be done easily both in air or in vacuum. Figures 6.1 and 6.2 show IV curves from Ti/Au and Pt devices, respectively. The IV curves in Figure 6.1 are from different devices from three different wafers, the black curves are from a wafer with 10 nm Ti and 100 nm Au, the orange curves are from a wafer with 7 Å Ti and 70 Å Au and the blue curve is from a wafer with 5 Å Ti and 70 Å Au. Of course, metal film thicknesses within a precision of 2 Å cannot be deposited in the evaporators applied, so the Ti thicknesses of the two last wafers just indicate that one has a little more Ti than the other. All the IV curves in Figure 6.2 are from devices with 200 Å Pt, and the three colors again indicate different wafers.

As discussed in Section 3.1, the voltage drop across the oxide when applying a certain device bias voltage will depend on the flat band voltage of the device and hence on the metal work function. This implies that when plotting the transmission current versus the device bias voltage for

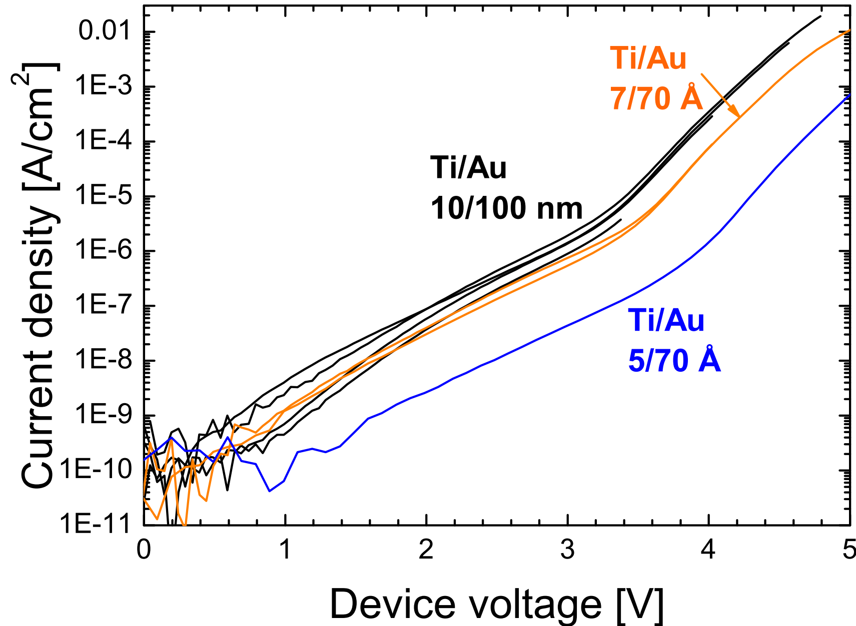

Figure 6.1: Transmitted current vs. device bias voltage for devices from three different wafers. Black curves: 10 nm Ti and 100 nm Au. Orange curves: 7 Å Ti and 70 Å Au. Blue curve: 5 Å Ti and 70 Å Au.

devices with different metals, the curves will be shifted proportional to the difference in metal work function at the oxide-metal interface. This effect can be clearly seen in Figure 6.1 where the curves are shifted to higher device bias voltages, as the Ti layer becomes thinner. With a Ti layer of 10 nm thickness (black curves) the metal work function at the oxide-metal interface must be that of Ti, but with a thickness in the single monolayer range, the apparent metal work function at the interface seems to gradually increase towards that of Au with decreasing Ti thickness. The kinks in the IV-curves at approximately 3.3 V and 4.1 V indicate the onset of FN-tunneling.

Another factor, that influences the current density greatly, is the oxide thickness, which we know varies from wafer to wafer. This is dealt with elaborately in [C]. Here this effect can be seen in Figure 6.2, where the oxide thickness is approximately 55 Å for the devices giving the green and the red curves, whereas the oxide thickness on the wafer from which the black curve stems was measured to be 62 Å. Such an increase in oxide thickness results in a markedly lower transmission current.

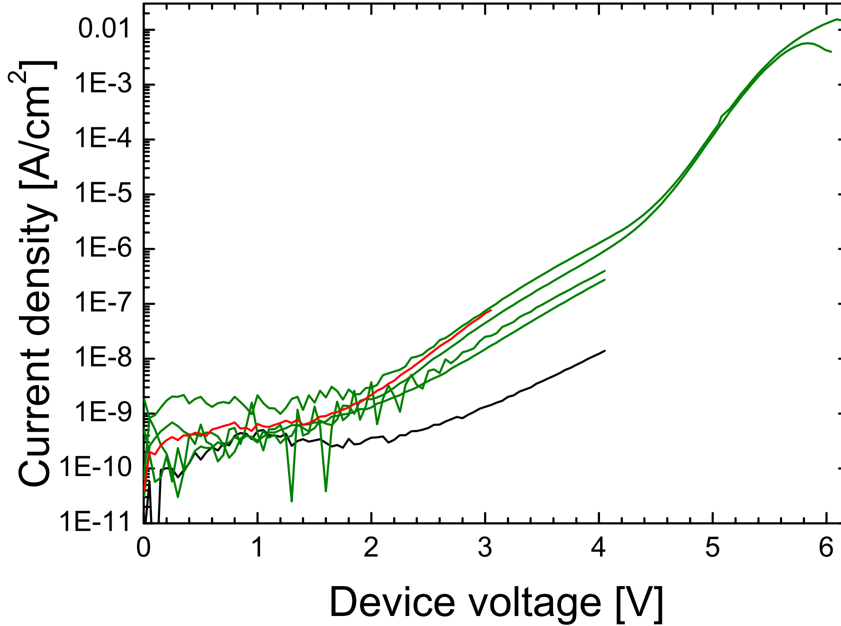

Figure 6.2: Transmitted current vs. device bias voltage for devices from three different wafers with 200 Å Pt. Each wafer is represented by a different color.

For comparison, representative IV curves for Ti/Au and Pt devices from Figure 6.1 and 6.2, respectively, are plotted together with curves from devices with 10 nm Cr and 10 nm Au in Figure 6.3. It should be noted, that the Cr/Au devices have an oxide thickness of 63 Å, so in terms of metal work function it is hard to compare to the other devices in this plot. The other plots indicate, that the metal work functions increase in the following order $\Phi_{\text{Ti}} < \Phi_{\text{Au}} < \Phi_{\text{Pt}}$, which is in agreement with the literature [30]. If we assume that the position of the kink in the IV-curves coincides with the onset of FN-tunneling, the metal work function can be calculated as $\Phi_{\text{M}} = V_{\text{FN,on}} + \chi_{\text{ox}}$ as discussed in Section 3.2.1. We have $\chi_{\text{ox}} = 0.9$ V and hence get: $\Phi_{\text{Pt}} = 5.3$ eV, $\Phi_{\text{Ti}} = 4.2$ eV, $\Phi_{\text{Ti 0.7,Au}} = 4.4$ eV, and $\Phi_{\text{Ti 0.5, Au}} = 4.8$ eV. Work functions values for these metals at the vacuum interface are reported to be 4.3 eV for Ti, 5.4 eV for Au and 5.7 eV for Pt [30], so our values show the right trend, though they are determined in a rather crude way.

Plotting the data in FN-plots is a way of determining the nature of the electron transport through the oxide, since a linear dependence in this sort of plot would be a signature of FN-tunneling as discussed in Section 3.2.1.

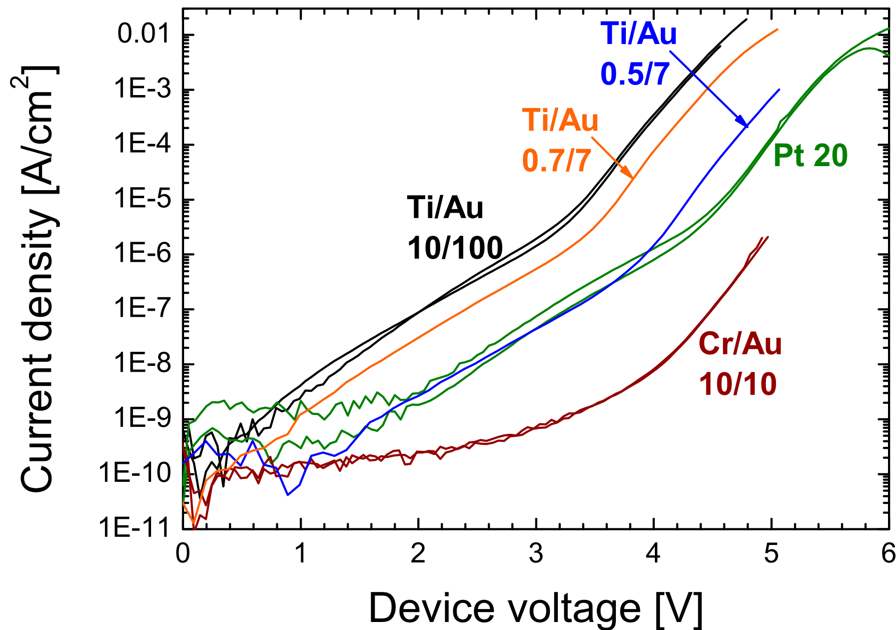

Figure 6.3: Transmitted current vs. device bias voltage for devices with different metal films. A shift in voltage of the curves due to differences in metal work function is clearly seen.

This is done in [A] for devices with 10 nm Ti and 100 nm Au, and indeed, the primary mechanism for electron transport above a certain bias voltage is shown to be FN-tunneling.

An interesting effect was encountered in the beginning of the project, when we produced devices with Al as the top metal film. They proved to be highly unstable and to break down at low device bias voltage as opposed to the Ti/Au devices. From the Ellingham diagram showing standard free energies of oxide formation for various metals vs. temperature [61] it is seen, that Al shows a higher affinity for O than Si. Al will therefore be able to reduce SiO_2 and if this happens at the metal-oxide interface of the device, this will lead to a much more complicated structure, which might resemble a double barrier structure (Si-SiO_2-Si-AlO_x-Al). Seen from the outside, it will probably behave like a thinner tunnel barrier, which would explain the behavior we observed. Ti will also show a small tendency towards reduction of SiO_2, whereas Cr will not. Whether this introduces a difference between Ti/Au and Cr/Au devices cannot be seen from the data, since the Cr/Au devices have a markedly thicker oxide

6.2 Electron Emission

Electron emission measurements are interesting in two aspects, both in order to explore the possibilities of utilizing our devices as free electron emitters but certainly also as a way to assess their value for HEFatS. The energy distribution of the electrons at the metal-adsorbate interface is crucial, but we cannot measure it below the work function of the metal, so we must rely on measurements above the work function, as will be presented below. It would be desirable to be able to lower the function in order to see the energy distribution at lower energies. We have lowered the work function of the metal film surfaces by deposition of Cs, but unfortunately this affected the oxide performance directly, changing the device characteristics completely. These experiments are therefore not treated in this section, but postponed to Section 6.4, as well as [B] and [C]. Also the homogeneity of emission across the surface is important, as will also be a further issue of this section.

6.2.1 Electron Emission in Air

This section will present a few results from experiments with emission in air which highlights some issues regarding electron transport in the metal film and the metal work function. Figure 6.4 shows simultaneously obtained emission and transmission currents from three different devices, one device has 200 Å Pt (green) and the others have 5 Å Ti and 70 Å Au (blue) and 7 Å Ti and 70 Å Au (orange). Even for dirty surfaces in air, the work function of Pt is seen to be markedly higher than for Au as deduced from the onsets of emission at 5.5 V and 4.5 V, respectively. Another interesting finding is the dramatic effect of the amount of Ti on the emission efficiency, which is also one of the main results in [B]. Just a small increase in the thickness of the Ti wetting layer will shift the transmission curve to lower bias voltages as discussed in Section 6.1, but it also leads to increased scattering of the tunneling electrons. Somehow Ti at the interface acts as very efficient scattering potentials, a mechanism which we do not have enough information to speculate about. A similar study of devices with Cr/Au could establish whether the oxidation of Ti and the induced reduction of SiO_2 affects this, since Cr would not reduce SiO_2 as discussed above in Section 6.1.

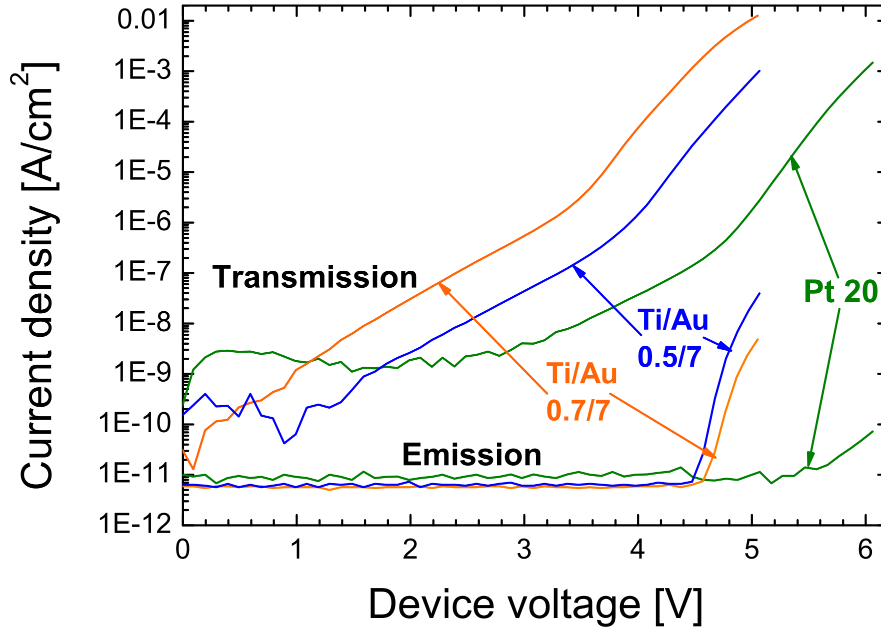

Figure 6.4: Simultaneously obtained transmission and emission currents vs. device bias voltage for three different devices in air. 200 Å Pt (green), 7 Å Ti/70 Å Au (orange) and 5 Å Ti/70 Å Au (blue). There is a difference in emission onset of 1 V between Au and Pt, and a large difference in emission efficiency between the two devices with Ti/Au.

6.2.2 Electron Emission Spectra

Energy resolved spectra of the electrons emitted from a device can be obtained with the HSA as described in Section 5.2.7. Figure 6.5 shows normalized emission spectra for five different applied device bias voltages from 5.0 V to 6.3 V. The device is smaller than usual, 2 mm^2, and has a 10 Å Ti/70 Å Au top metal film. Zero on the energy scale is the work function of the analyzer and the low energy cut-offs of the spectra implies that the work function of the device is 0.5 eV higher. The high energy flanks are similar for each spectrum and the displacement is seen to be proportional to the increase in device bias voltage, as is the displacement of the maximal peak. At the higher device bias voltages more features of the spectrum get visible, and next to the high peak, which we interpret as the ballistic electron peak, a shoulder of electrons which have lost ~0.8 eV appears. The emitted electron current varies by orders of magnitude over this range of applied bias voltages, so the channeltron voltage must be adjusted dur-

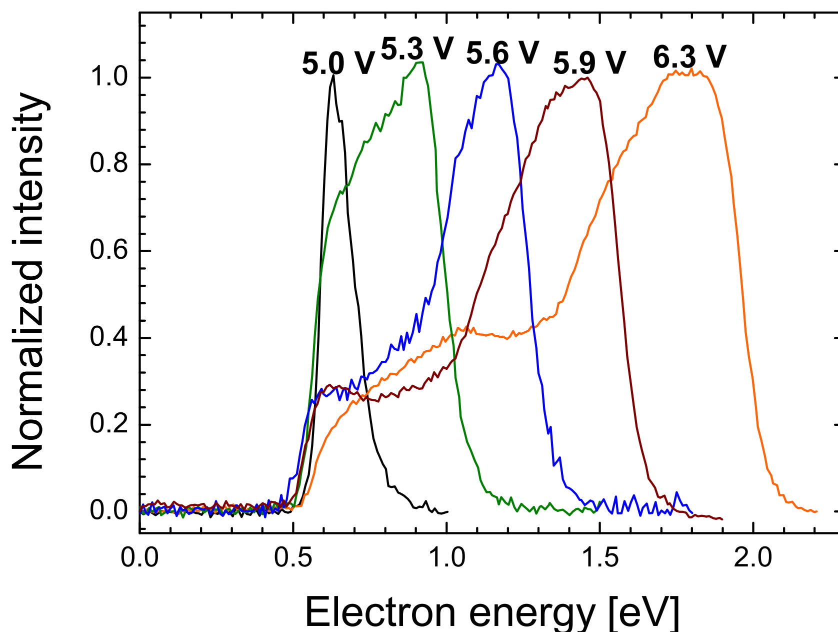

Figure 6.5: Normalized electron emission energy spectra from a device with applied bias voltages of: 5.0 V (black), 5.3 V (green), 5.6 V (blue), 5.9 V (dark red), and 6.3 V (orange). The electron energy is relative to the analyzer work function, and the cut-off at 0.5 eV is due to the device surface work function.

ing the experiment. The relative gain at voltages from 1700 V to 3500 V has been determined by calculating integrals for the spectra at each gain voltage for a constant device bias voltage, assuming a constant emission current. With these relative gain values, the spectra from Figure 6.5 can be re-scaled as plotted in Figure 6.6, where the integral of each spectrum is now proportional to the emission current. These spectra suggest that a major part of the hot electrons arrive at the metal-vacuum interface with their energy intact or having suffered only minor losses. This is an important prerequisite for studying the ability to selectivity enhance certain reactions by tuning the electron energy to the desired resonance.

6.2.3 Spatially Resolved Emission

The Microchannel Plate (MCP) assembly is applied for visualizing the distribution of emitted electrons over the active area of a device as described

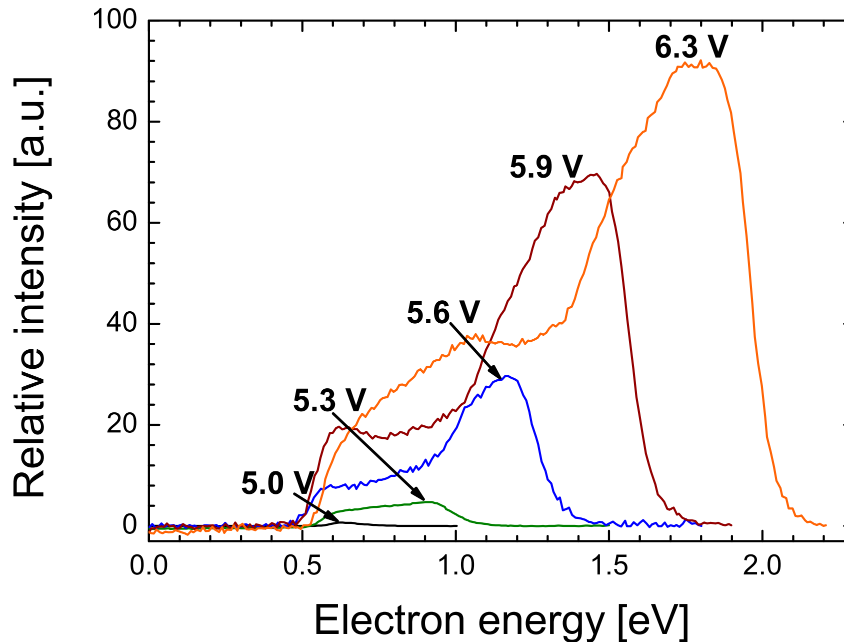

Figure 6.6: Electron emission spectra from Figure 6.5, re-scaled by the gain of the channeltron, so the relative integral represents the relative emitted current.

in Section 5.2.7. Figure 6.7 shows pictures obtained at increasing device bias voltage, from 4.50 V to 5.30 V. Pictures a) to g) are obtained with a total voltage of 1800 V across the MCP stack, which is lowered to 1500 V for picture h in order to prevent damage of the MCP. The device has a 55 Å oxide and a 200 Å Pt film which was not cleaned after insertion into UHV. At 4.50 V only noise can be seen, but at 4.55 V the outline of the active area is becoming visible, indicating the onset of electron emission. This is seen much more clearly in Figure 6.8, where the light intensity along a horizontal line across the device is plotted. Each value is a mean of the pixel-values along an orthogonal line. The shape of the emitting area as seen in the pictures in Figure 6.7 is not quadratic, but this is due to a shadow effect from the left mounting clip. Furthermore, a number of ring-shaped features can be observed in the pictures, the first one emerging at 4.55 V, with their number and intensity increasing with device bias voltage. We explain them as effects of small Si or dust particles present on the surface, which can be seen by the naked eye. Electrons emitted in close proximity to these particles will be deflected by the charge on the particle, resulting in small

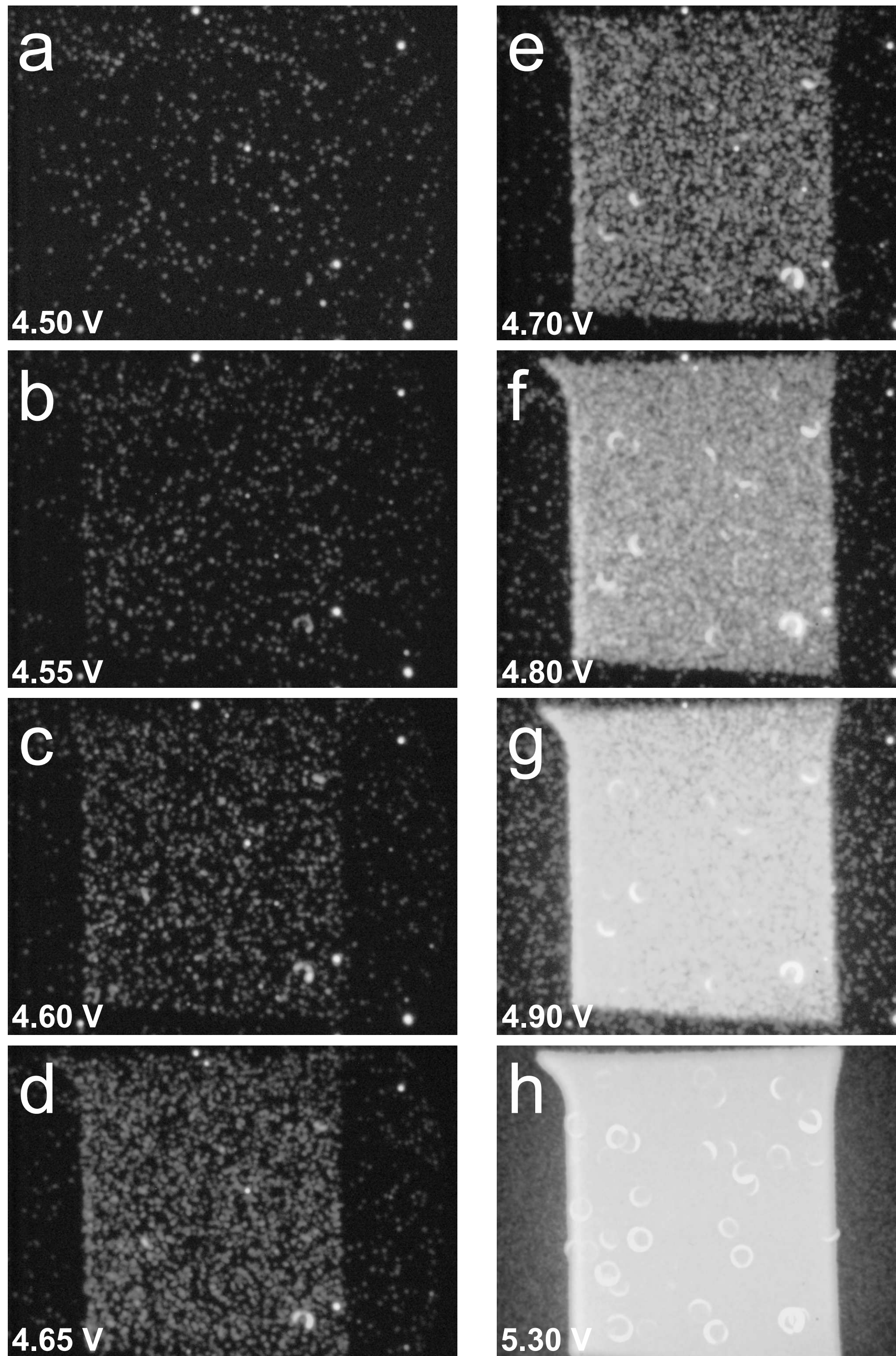

Figure 6.7: Pictures of the electron emission from a Au device as amplified by the MCP for increasing device bias voltage. a)-g) are recorded with a total voltage of 1800 V across the MCP stack, h) is with a total voltage of 1500 V.

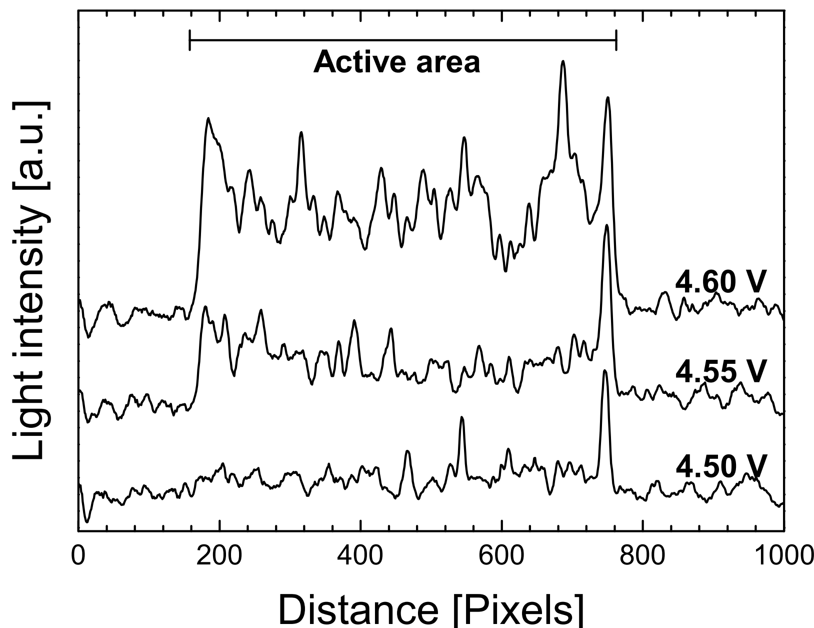

Figure 6.8: Plots of the light intensity along a horizontal line across the emission pictures a-c in Figure 6.7. The onset of emission is seen to occur between 4.50 V and 4.55 V device bias voltage, which determines the value of the lowest work function of the surface.

electron cones around the particle. The onset of electron emission is a little above 4.50 V on the uncleaned Pt surface, well below the reported work function of 5.7 eV for Pt [30], but this is expected for a surface covered by C compounds.

With the limitations of the resolution of the MCP stack discussed in Section 5.2.7, which is well above 25 μm, information about the homogeneity of emission is limited to the 50-100 μm range. On this scale a variation in emissivity is seen, which might be caused either by variations in the local work function or in the electron current arriving at the surface. The oxide thickness has been demonstrated to vary on a length scale of 10 μm [A], but for this to be the cause of the observed emission variations, the oxide should exhibit some rather abrupt thickness changes. Work function variations on a non-cleaned sample are however very likely, for instance along grain boundaries of the metal film. We have not been able to determine the microstructure of the metal films, but in high-resolution Scanning Electron Microscopy (SEM) they look very smooth and continuous also after a heat

treatment. A way to determine the origin of the variations would be to image the emission before and after cleaning of a device, and for various degrees of annealing of the metal film, and hope for a change of crystallite size during annealing. Ballistic Electron Emission Microscopy (BEEM) [62] would be the ideal technique for spatially resolved investigations of the oxide barrier, even down to the nm-scale. In BEEM electrons can be injected from an STM tip into the top metal film (or the other way round), and by varying their energy and detecting the resulting BEEM current in the bottom electrode (here Si), a measure of the oxide barrier at that particular spot can be deduced.

On the length scale of the device size there is also a small variation indicated by a slightly higher emissivity in the lower left part, as compared to the upper right part. Ellipsometer measurements on un-patterned wafers with only the thin oxide grown do indeed show variation in oxide thickness of a few Å across a wafer.

6.3 Cleanness of Metal Surfaces

The cleanness of the metal surfaces of the devices are of course of major importance when surface reactions are to be studied. XPS overview spectra show, that the constituents of the surface contamination are C and O, and TID spectra of a Pt device just set into UHV revealed a large amount of H_2, so, as would be expected, samples transferred from ambient air are covered by a layer of carbon hydrides, possibly partly oxidized and maybe also some H_2O. Unfortunately, the sensitivity of C detection in XPS is rather poor (sensitivity factors 0.21 for C 1s, 0.63 for O 1s and 1.9 for Au $4f_{7/2}$ [63]), so this method does not give a very good measure of the cleanness for submonolayer C coverages. In ISS, C is detected indirectly by the absence of signal, since it does not give a scattering line itself [64][1] but effectively blocks the metal atoms. The exposure to energetic He ions, however, is detrimental to the oxide, as discussed below.

In surface scientific studies, cleaning procedures includes sputtering with energetic noble gas ions, possible heating in O_2 followed by H_2 and finally annealing. Sputtering is not applicable in our case, because of the delicate SiO_2 layer in the device. According to our tests, the ion energy should be below 1 keV not to cause breakdown in the oxide. Exposure to 500 eV Ar ions did not alter the IV characteristics of a device with 3 Å Ti/50 Å Pt, whereas an exposure time of only 1 min to 1 keV Ar ions lead to

[1] If not bound carbidic.

an increase in current by a factor of 10, and further exposure lead to oxide breakdown. At such low energies, the sputter yield is too small for cleaning purpose, both on Au and Pt. The exposure to 1 keV He ions during ISS measurements was seen to have the same effect on the IV characteristics as 1 keV Ar ions. A reasonable explantation would be that the ions still have some energy after traversing the thin metal film, so they will create defects in the oxide, and the increasing number of defects with ion dosage leads to a soft breakdown.

The next two sections will describe the cleaning procedures developed for Au and Pt surfaces, respectively.

6.3.1 Au Cleaning

When cleaning Au surfaces we wanted to take advantage of the nobleness of Au, and use a chemical solution to oxidize the carbon film just prior to insertion of devices into the loadlock. Inspired by the oxidizing solutions applied in the cleanroom for wafer cleaning, four solutions where tested, followed by rinsing in water: RCA I, RCA II, pure H_2O_2 30% and pirañha. The RCA solutions are described in Appendix A and were used at room temperature as was H_2O_2. Pirañha is a mixture of H_2SO_4 98% and H_2O_2 30% in the relation 3:1 which spontaneously warms up to 70-80°C upon mixture. Comparison of XPS spectra of Au films cleaned by one of these solutions showed by far the best results with RCA I. Oxidation times of 1 to 10 min were tested, and we settled on 4 min. Figure 6.9 shows XPS spectra of the C 1s and the O 1s lines for various treatments of the sample. The spectra have been normalized by the integral of the Au 4f lines and offset by a constant for clarity. Comparing 1 (dark red) to 2 (orange) and 3 (blue) to 4 (green) in the figure, it is seen how the RCA I solution clearly oxidizes the present C, thereby removing a major part of it.

In order to remove the residual C contamination after insertion into UHV, the effect of 500 eV oxygen ions produced in ion gun 2 was tested, and this method proved very efficient in 'burning' the rest of the C containing film, see curve 5 (black) in Figure 6.9. It did not affect the electrical properties of the device. This treatment did not oxidize the Au surface, in contradiction to earlier studies [65; 66], but we explain this by the higher doses [65] as well as energies [66] applied as compared to our case, and that C oxidation is probably preferred over Au oxidation. So with our objective of cleaning the sample, we stop the ion exposure when the C contamination has been oxidized, but before we start oxidizing the film. Further tests along the same line of applying highly reactive components to the sur-

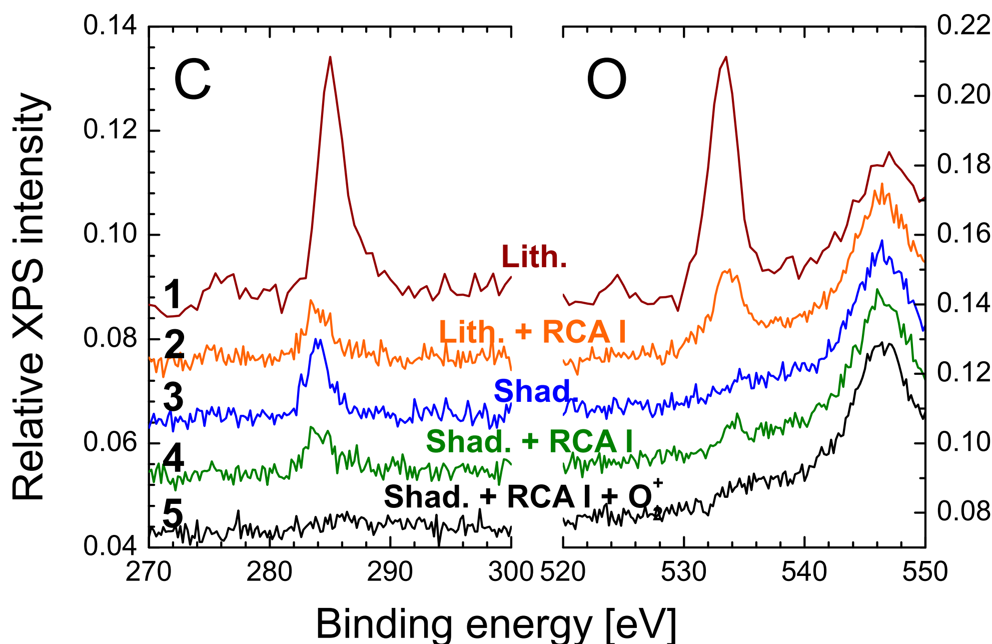

Figure 6.9: XPS spectra of the C 1s line at 285 eV (left) and the O 1s line at 534 eV (right) from samples cleaned in different ways. The line at 546 eV is the Au $4p_{3/2}$ line. The spectra are divided by the integral of the Au 4f lines for comparison, and each offset by a constant for clarity. 1 - Dark red: Photolithography mask, as set into UHV. 2 - Orange: Photolithography mask followed by RCA I cleaning. 3 - Blue: Shadow mask, as set into UHV. 4 - Green: Shadow mask followed by RCA I cleaning. 5 - Black: Shadow mask followed by RCA I cleaning and O_2^+ sputtering.

face were not successful. In an apparatus available in the cleanroom, the sample was exposed to an oxygen plasma, but this only led to F contamination from the machine. Exposure to H atoms from an atomic hydrogen source (described in [F]) mounted on the chamber had no effect either.

A very clear improvement of the cleanness followed the development and application of shadow masks, replacing the lithography masking procedure for metal deposition. This is clearly seen in Figure 6.9, where the dark red (1) and the blue (3) spectra are from samples not cleaned in any way, where masking was done by photolithography and shadow mask, respectively. The amount of C on the sample is clearly reduced by omitting the photolithography mask and lift-off. Figure 6.10 shows ISS spectra of samples which have been cleaned by RCA I followed by O_2^+ sputtering, but one was made with shadow mask (black curve), the two others with

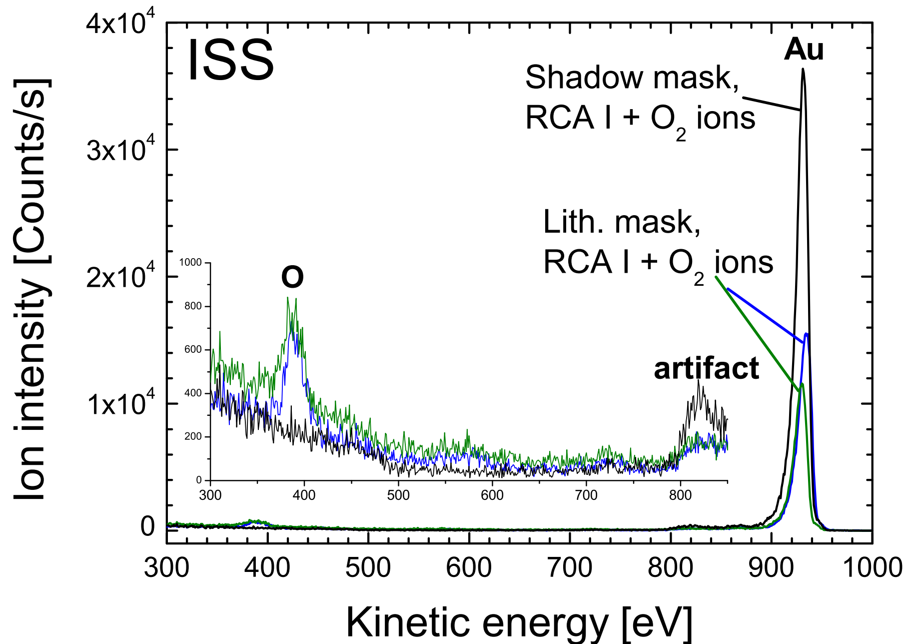

Figure 6.10: ISS spectra of samples cleaned by RCA I and O_2^+ sputtering, one produced with shadow mask (black) and the other two with photolithography mask (green and blue). The inset shows a magnification of the spectrum from 300 eV to 850 eV. The Au peak is seen at 933 eV, an O peak at 395 eV and an artificial peak at 820 eV, see discussion in Section 6.3.3.

photolithography masks. The latter were sputtered for twice as long, 30 min. Results from the Cs on Au studies presented later in this chapter are obtained from a device made with the shadow mask.

6.3.2 Pt Cleaning

Since Pt is so much more reactive than Au, the procedure for cleaning it must necessarily be different. Pre-cleaning the surface in an oxidizing solution was no success, probably because Pt will quickly take up C compounds from the air before it is put into the loadlock. It can however easily be cleaned by heating it in O_2 in the chamber, as long as the surface has been exposed to ambient pressures of O_2 no longer than 1 day prior to cleaning. We observed a correlation between the time the devices had been under vacuum in the loadlock and how well they could be cleaned after we had

worked on a few devices which were impossible to clean by the usual procedure. Venting the loadlock with air and pumping down again seemed to work, therefore an O_2-bottle was installed on the loadlock, so that we can expose the samples to 0.5 bar O_2 prior to insertion into UHV under more controlled conditions than with ambient air. We suggest that at high pressures, O_2 can get down to the Pt surface through the C compounds and help initiating the oxidation when later heating the sample in low pressures of O_2 in the chamber. This adsorbed O_2 will however disappear over time in the pumped-out loadlock.

Figure 6.11 shows typical curves measured with the QMS of the CO (green) and CO_2 (black) desorption vs. time during heating in O_2. O_2 is let in to a pressure of 5×10^{-7} mbar before the measurement is started, and heating is started after 160 s by applying 6 V across the Pt film. The O_2 leak valve is closed after 480 s as can be seen from the O^{2+} signal (blue) (O_2^+ and O^+ signals saturate while dosing), and heating is turned off after 540 s at a thermocouple reading of 188°C. Immediately after turning on the heating, sharp features from both CO and CO_2 are observed, which are probably due to direct desorption of these two molecules, whereas the smoother features at higher temperatures are interpreted as the product of oxidation of larger C compounds.

After this treatment, the surface is clean as judged by ISS and TID. Figure 6.12 shows a typical ISS spectrum of a cleaned Pt surface recorded at 120°C in order to prevent CO adsorption. A small amount of O is present on the surface, but by comparing to the Pt peak it is seen to be a very small fraction of a monolayer. CO from the chamber background quickly adsorbs on the surface while cooling down, so XPS spectra recorded from the cleaned sample always show a small amount of C and O. Since heating is done by applying a bias voltage across the film, heating during XPS would lead to some shift and broadening of the peaks. TID spectra, however, obtained after having dosed ^{29}CO from right after cleaning and during cool-down to 45°C, show features from both terraces and steps, indicating a clean Pt surface. The CO TIDs will be discussed more intensively in Section 6.5.

6.3.3 Interpretation of Additional Features in ISS Spectra

As we investigated the surfaces with ISS, some unexpected features appeared in the spectra, which I will try to account for here. The spectra from both clean Au and clean Pt presented above have a small peak at around 820 eV, see Figure 6.10 and 6.12, respectively. At first it was explained as

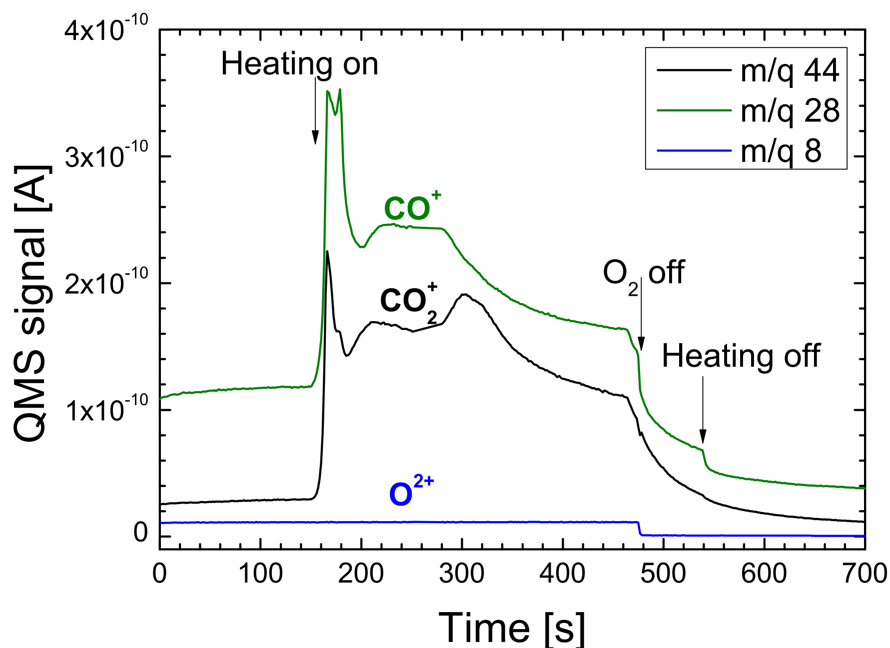

Figure 6.11: QMS signals vs. time for three different mass-charge ratios (m/q) during cleaning of a Pt surface. O_2, O^{2+} (blue), at a pressure of 5×10^{-7} mbar is let into the chamber before the measurement starts. After 160 s heating is started, and CO (green) and CO_2 (black) is observed to desorb. The O_2 leak valve is closed after 480 s and heating is turned off after 540 s at a thermocouple reading of 188°C.

Cu or Mo from the surroundings (also in [A]), but the energy match is not quite satisfactory (Cu 808 eV, Mo 867 eV) and these surfaces are most likely oxidized and C-covered. Subsequent measurements have shown, that the peak intensity increases when the raster amplitude of the ion beam is decreased, which also speaks against it being the holder. The magnitude of the peak does not increase with ion exposure, so it is not a result of the deposition of material during scanning. The morphology of a surface can give rise to several effects like changes in relative peak intensities by the tilting of the sample or appearance of peaks in certain geometries [60; 67]. Our geometry would allow for scattering from the second atom layer in the surface or in general from atoms beneath the topmost layer at steps, which would lead to a small energy loss of the scattered ion [60]. We expect the Au and Pt films to be similar enough in terms of crystallite size and surface morphology for the same scattering events to occur.

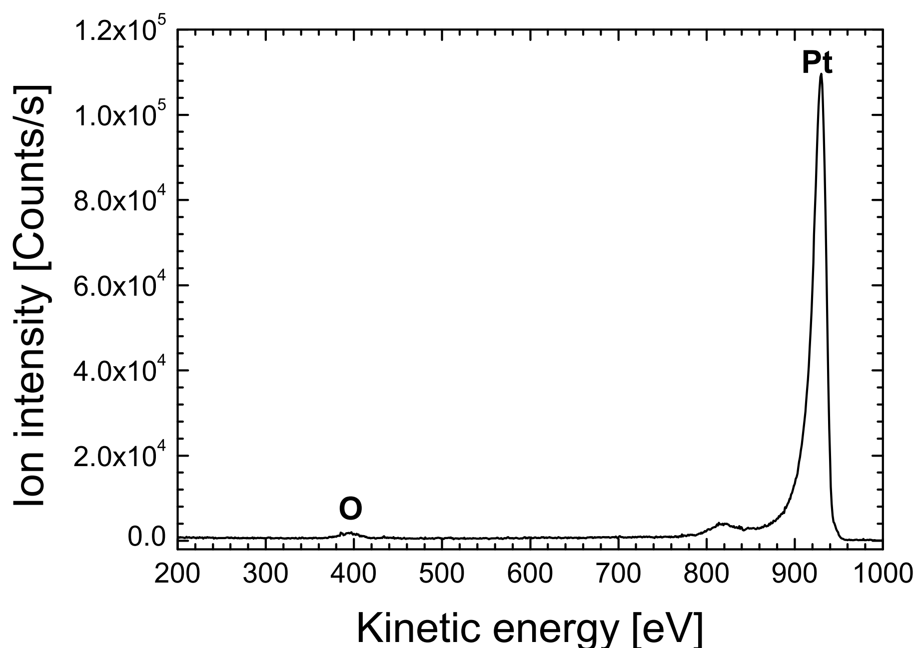

Figure 6.12: ISS spectrum from a cleaned Pt surface kept at 120°C to avoid CO adsorption. The Pt elastic peak is at 932 eV in correspondence with Equation 5.1. A small amount of O is detected at ∼395 eV, which is lower than the expected 417 eV, but it can nonetheless be seen from ISS spectra obtained from CO dosed Pt-surfaces to be O.

Another rather frustrating peak appeared when we were obtaining consecutive ISS spectra of a CO saturated Pt surface in order to evaluate the sputter effect. It appears a little above 400 eV and increases in intensity while moving down in energy the longer the sample is exposed to the ion beam. In Figure 6.19 in Section 6.5 the peak is seen around 300 eV (blue curve) in the second of two consecutive scans of the CO saturated Pt surface. Testing the influence of all variable parameters on this peak on the clean Pt surface has led to the conclusion, that it stems from charging of the thick protective oxide not covered by metal on each side of the device's active area.

6.4 Cs on Au

The deposition of sub-monolayer coverages of alkali metals on other metal surfaces is known to decrease the work function of the surface substantially. The work function is experimentally observed to decrease fast to a minimum value which is below the work function of the bulk alkali and which occurs at a certain fraction of a monolayer (ML). The work function then increases to the alkali metal work function at the completion of a full monolayer [68–70]. This behavior can be modeled by negative charge donation from the adsorbate alkali to the substrate metal which effectively lowers the barrier at the surface. As the coverage increases in the beginning, more and more atoms can donate a certain amount of charge to the substrate resulting in a rapidly decreasing work function. At some coverage, however, each atom will only be able to donate smaller amounts of charge due to the already donated charge and this is where the minimum work function occurs [69; 70].

We would like to exploit this phenomenon to lower the work function of our devices in order to get emission at lower energy and hopefully learn more about the energy distribution. We have chosen Cs, since it has the lowest work function ($\Phi_{Cs} = 2.1$ eV [30]) of the alkali metals. We have characterized the Cs/Au surface in terms of work function, Cs coverage and emission onset as will be discussed below, and these results are also published in [A]. Further studies of the effect of oxygen on the Cs overlayer will also be described here.

As discussed in Section 5.2.5, ISS is an extremely surface sensitive method, and can therefore be applied for determining overlayer coverages up to one monolayer. Unfortunately we were not able to detect Cs by ISS in our geometry, we only saw an attenuation of the Au signal with increasing Cs coverage. Figure 6.13 shows ISS spectra of the clean Au surface (black) and the surface after a Cs deposition series (green). Cs would yield an elastic scattering peak at 902 eV, which is not seen, whereas the size of the Au peak at 933 eV is highly reduced after Cs deposition. The effect of Cs deposition on the Au peak is shown in more detail in the inset of Figure 6.14, where the ISS spectra for each cycle of the Cs deposition series are plotted together.

The neutralization probability of an energetic ion approaching a surface is known to be very dependent on the surface work function, since different neutralization mechanisms will be available. At high work functions, charge transfer between the noble gas ions and the target can be ascribed to collision induced and Auger processes, whereas at lower work functions resonant processes can occur [67; 71]. Resonant neutralization by ion scat-

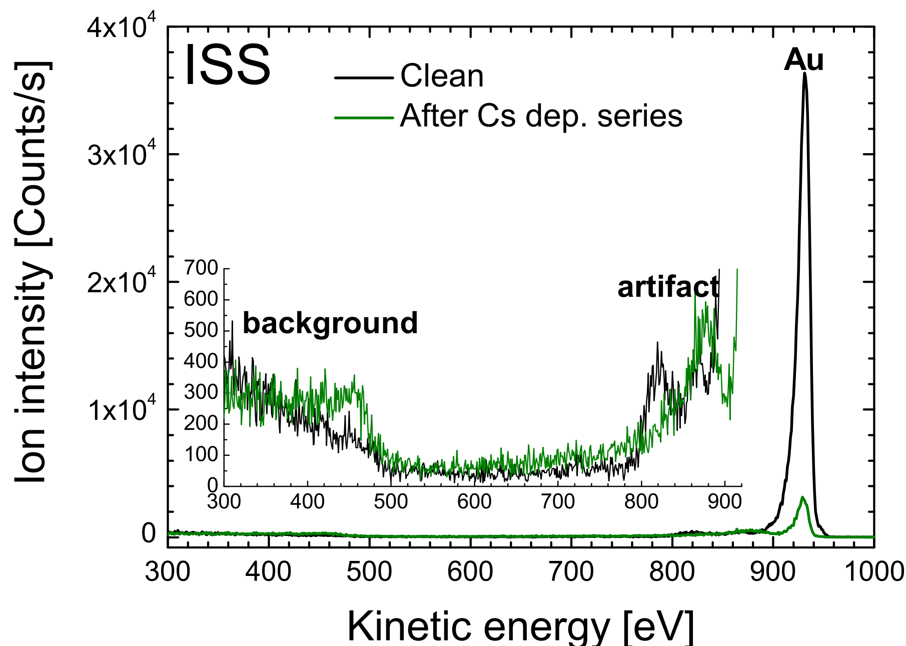

Figure 6.13: ISS spectra from a clean Au surface (black) and from the same surface after a Cs deposition series (green). Cs does not give rise to a peak, but it effectively covers the Au, the signal of which diminishes. The inset shows a magnification of the spectra in the 300 eV to 900 eV range. The background of the clean sample is discussed above in Section 6.3.

tering from alkali atoms is seen to be very efficient and leads to very low ion yields from alkali adsorbates on transition metals [67; 71–75]. Also in this case, actual ion yields are very dependent on the exact geometry, for instance K on Pt has been reported only to be visible in ISS spectra at grazing incidence angles [72], and the relative ion yield from Cs on Ni was seen to drop by a factor of 30 when going from a grazing to a near normal exit angle [75]. These results are consistent with our finding, that we cannot detect Cs with an incidence angle of 45° and a scattering angle of 135°. Our approach has therefore been to determine the Cs coverage from the attenuation of the Au signal in ISS.

The whole Cs deposition series consists of cycles of these steps: 1) Cs deposition, 2) work function measurement, 3) XPS spectra of the Au 4f, Cs 3d and O 1s lines, 4) ISS spectrum, 5) repeat work function measurement, 6) repeat XPS spectra. The exposure to 1 keV He^+ ions during the ISS

measurement leads to a small decrease in the amount of Cs on the surface due to sputtering. Therefore work function and XPS measurements are done both before and after ISS and averages of the extracted values are used. Figure 6.14 shows the integral of the ISS Au peak vs. the amount of Cs deposited as measured in XPS. The latter value is quantified by taking the Cs $3d_{5/2}$ line integral divided by the Au 4f line integral. This assumes negligible attenuation of the Au 4f signal due to the Cs overlayer, which at these low coverages is reasonable. The relative Cs 3d signal does indeed increase proportionally to the total deposition time, so it is a good measure of the Cs coverage, which can be obtained without ruining the oxide as the ion exposure in ISS does. The ISS Au integral is seen to fall off linearly with Cs coverage in the beginning and then it levels off. This behavior suggests immobility of the Cs atoms on the Au surface, and the growth of multilayers before the Au surface is totally covered. A linear fit to the points 2 to 7 of this graph is represented by a blue line in the figure and it intersects the abscissa at a relative XPS Cs signal of 0.22, which we designate as 1 ML, in the sense that above this coverage, multilayers of Cs will grow.

Figure 6.15 shows the change in work function vs. Cs coverage as measured with XPS. The work function decreases rapidly, almost linearly, at low coverages and levels out at higher coverages. This is consistent with the literature [68–70], even though we do not observe a minimum. This might very well be because of the lack of long range order on our polycrystalline metal films. Other measurement series have been extended to higher coverages without the appearance of a minimum. The individual measurements from which the work function is determined are shown in the inset. The change of shape of the curves at low work function is due to saturation effects in the channeltron, even though we did what we could to reduce the signal.

The graph in Figure 6.15 shows the same behavior as the ISS Au integral vs. Cs coverage presented in Figure 6.14, and plotting the ISS Au integral vs. the work function change does indeed indicate a linear relationship, see inset of Figure 5 in [A]. There is some dispute in the literature as to whether the average work function [71; 74] or the local electrostatic potential [73] is probed by the ion beam, and some experiments point to that grazing exit angles favors an average effect whereas a near normal exit angle indicates local effects [75]. It seems, however, in general to be the case, that the substrate signal decreases with increasing coverage, without being affected by the work function change [71; 75]. This adds credibility to our way of determining the monolayer coverage from the ISS Au signal attenuation, and indicates that the linear relationship between the ISS Au signal and the work function change is not necessarily a direct physical dependence.

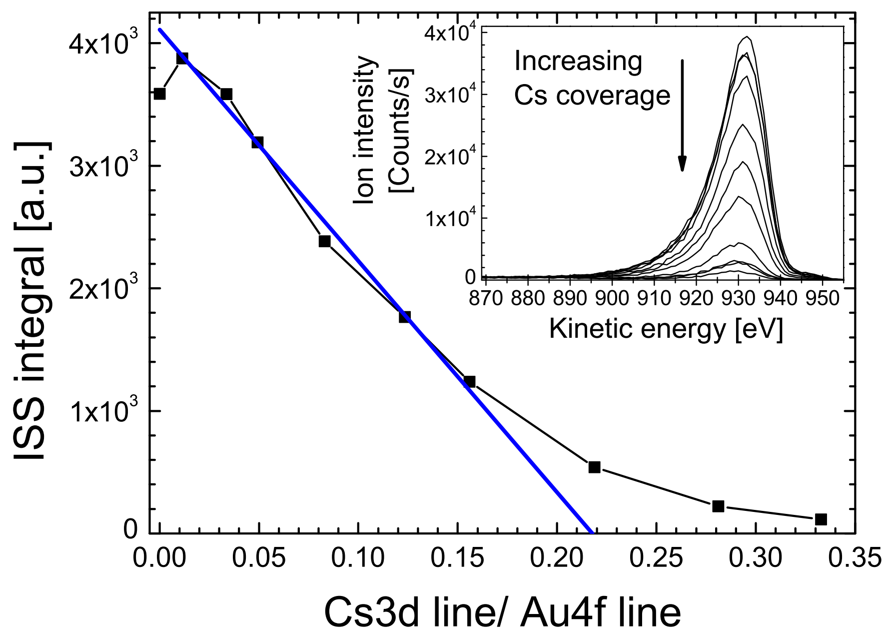

Figure 6.14: ISS Au peak integral vs. the XPS Cs $3d_{5/2}$ integral divided by the Au 4f integral. The latter value is proportional to the Cs coverage. The inset shows the ISS spectra of the Au peak for each point in the graph. The blue line is a linear fit to the points 2-7 in the graph, and the intersection of this with the abscissa is interpreted as a measure of the Cs coverage corresponding to 1 ML.

Work function and electron emission spectra were obtained on the clean Au surface and for two coverages of Cs. The spectra can be seen in Figure 6.16, where work function curves are orange and emission spectra are black (grey). Curve A is from the clean Au surface at 4.7 V device bias voltage, B is taken at 3.8 V after deposition of 0.87 ML Cs, C is taken at 2.2 V after deposition of additional Cs to a total coverage of 1.74 ML, and D is from this latter surface after a waiting time of 80 min, taken at a device bias voltage of 2.4 V. The curves for D are off-set negatively and the emission curve is shown in grey to make it distinguishable from C. The low-energy cut-offs in the emission spectra are seen to coincide very nicely with the work function.

As mentioned above, the aim of this part of the project was to learn about the electron energy distribution at energies lower than the metal film work function by the aid of Cs. Unfortunately, the deposition of Cs

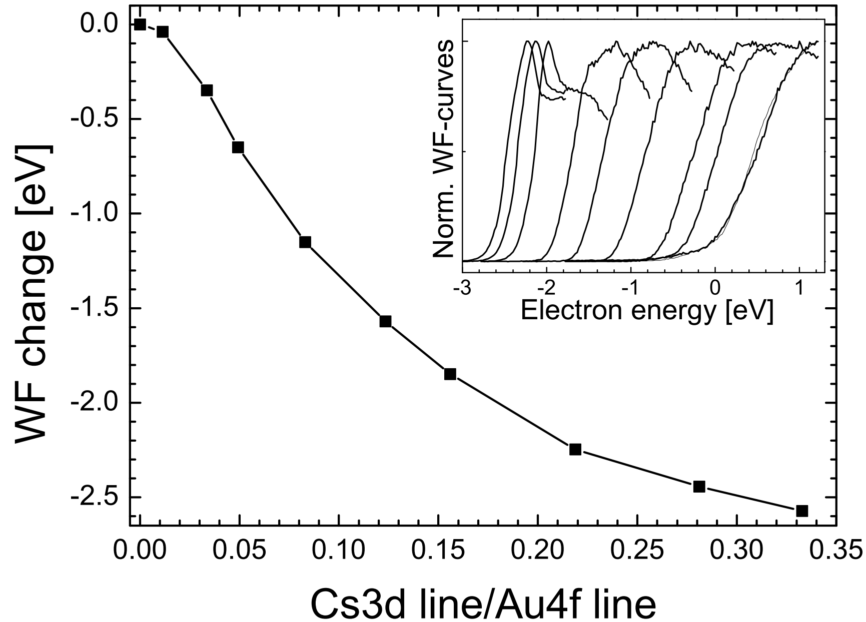

Figure 6.15: Work function of the surface vs. the XPS Cs $3d_{5/2}$ integral divided by the Au 4f integral. The inset shows the secondary electron energy spectra from which the work function values are determined.

on the Au film was seen to alter the electrical characteristics of the device dramatically, as can be seen in [B], Figure 6. The oxides were seen to suffer breakdown very fast and at low bias voltages, so the device bias voltages applied when obtaining the curves presented in Figure 6.16 were about the highest we were able to go for the time spans needed for the measurements. An increase of both the transmission and emission currents as well as a reduced maximum device bias voltage before instability sets in was also observed by Cohen [49]. Cs and Au alloy [76] so the change in electrical characteristics might very well by caused by migration of Cs to the oxide-Au interface and the resulting change of work function. Alkali atoms are further known to create highly mobile and undesirable charges in SiO_2, thereby degrading its quality [57].

LaRue et al. [77] have done related surface science studies of a Cs dosed Au(111) surface, and when this sample sits in UHV, they observe a slow increase in work function of 0.2 eV over 130 min, very similar to our results, compare C and D in Figure 6.16. They speculate that it might be

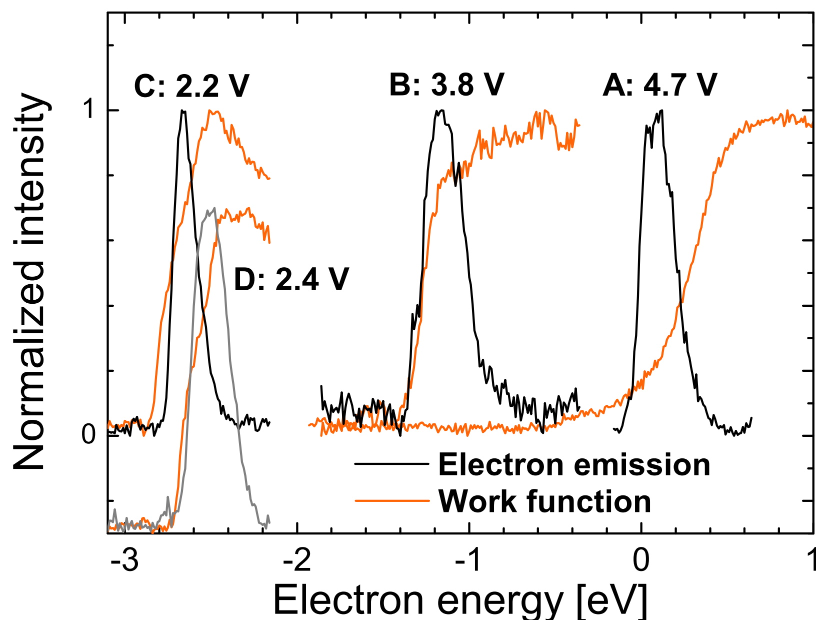

Figure 6.16: Work function (orange) and electron emission curves (black/grey) for four different surfaces A-D. All curves are normalized to a height of 1 for easier comparison. The energy scale is relative to the work function of the clean Au surface. A: Clean Au surface, device bias voltage 4.7 V. B: ∼0.87 ML Cs deposited on the Au surface, device bias voltage 3.8 V. C: ∼1.74 ML Cs in total deposited on the Au surface, device bias voltage 2.2 V. D: Previous surface after 80 min in UHV, device bias voltage 2.4 V. This curve is shifted downward for clarity. The curves show coincidence in work function and low energy cut-off of the emission curves.

the background in the chamber which slowly oxidizes the Cs overlayer. We have done some additional measurements, attempting to clarify this. The measurement series treated above was extended by performing XPS, ISS and work function measurements after the sample was left in the chamber overnight, and after subsequent dosing of first 6 L O_2 followed by 60 L O_2. Figure 6.17 shows XPS spectra of the O 1s line and the Cs 3d lines with the following colors: Left overnight (black), 6 L O_2 (green) and 60 L O_2 (blue). In the left part of the figure the O 1s lines are shown both before and after the ISS scan, and the spectra are off-set by a constant for clarity. The Cs spectra in the right part have been scaled by a factor which is the Cs $3d_{5/2}$ integral divided by the Au 4f integral, these numbers are listed in color-code in the figure. The last XPS spectrum of the Cs 3d lines taken before

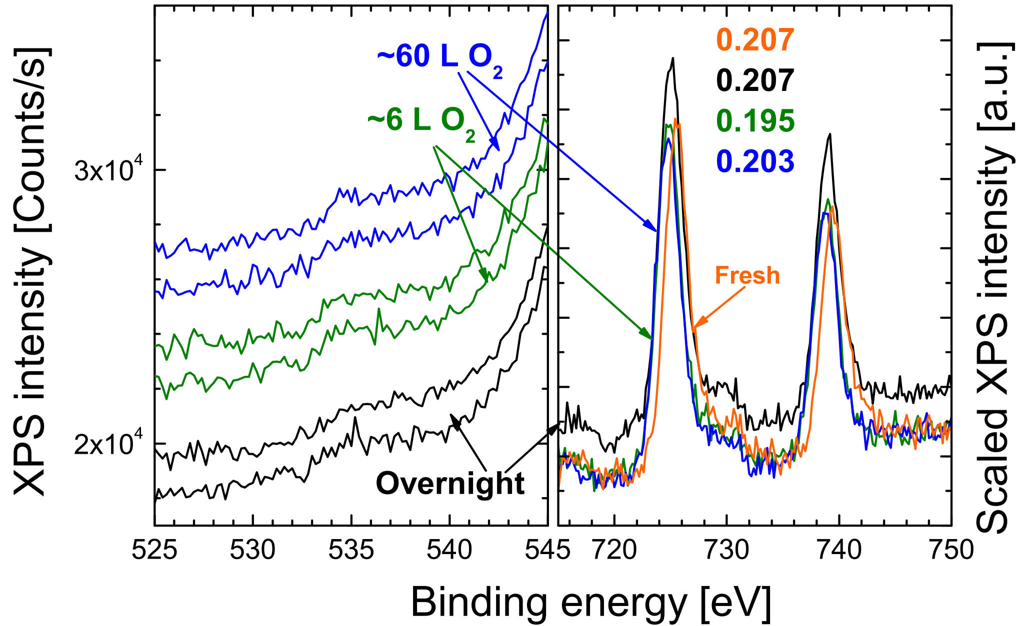

Figure 6.17: The effect of prolonged exposure to the chamber background as well as doses of O_2 on the XPS spectra of the O 1s and Cs 3d lines. The O 1s spectra to the left are off-set by a constant for clarity and both the spectra prior to and after ISS for each treatment are shown. The Cs 3d spectra to the right are scaled by the Cs $3d_{5/2}$ integral divided by the Au 4f integral (numbers given in figure), and only the spectrum obtained prior to the ISS measurement is shown. The last spectrum obtained at the end of the Cs deposition series is shown (orange). Then follows spectra after a night long UHV background exposure (black), and then exposures of 6 L O_2 (green) and further 60 L O_2 (blue).

the sample was left overnight is shown for comparison (orange). There is no detectable increase in the O 1s line intensity due to oxidation of the Cs overlayer and the relative Cs line intensities listed do hardly change, indicating that desorption of Cs is not the reason either. A small line shift of $\sim$1 eV of the Cs 3d lines to lower binding energies can be observed, but this alone cannot serve as an indication of oxidation, though Hrbek et al. [78] see a decrease in binding energy of 1.6 eV upon full oxidation of a 5 ML thick Cs film.

Time spend in UHV or the exposure to O_2 is seen to have an effect on the ISS spectra as well as on the work function as seen in Figure 6.18. ISS spectra obtained after the different treatments described are plotted in this figure with the same color-code as in Figure 6.17. The Au peak

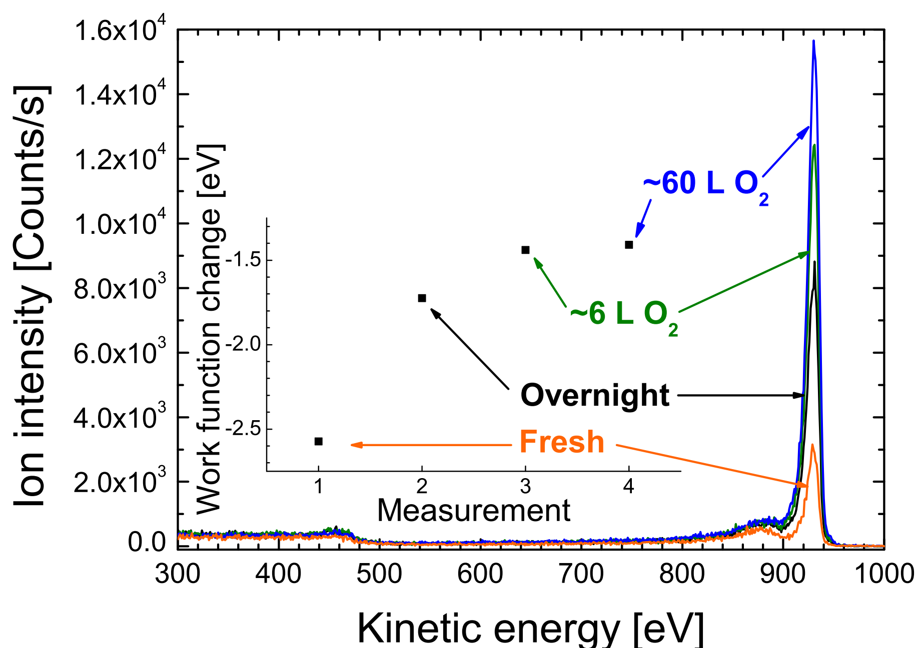

Figure 6.18: ISS spectra obtained after the same treatments as in Figure 6.17 with the same color-code. The inset shows the work function after each treatment relative to the work function of the clean sample at the beginning of the whole Cs deposition series.

height is seen to increase for each measurement, but no O can be detected. The inset shows the work function relative to that of the clean surface in Figure 6.15. It is clear that both the background in the chamber and O_2 exposure increases the work function, we do however not se any sign of oxidation of the Cs overlayer or desorption of Cs, so the exact mechanism is still unclear.

6.5 CO and O/O_2 on Pt

In order to be able to conduct experiments on various adsorbate-substrate systems we need clean surfaces. The detection of the desired adsorbate and comparison with results from the literature from systems with well-defined single crystals, can serve as proof of the cleanness of our device surfaces and their quality.

Figure 6.19 shows ISS spectra of a cleaned (green) and CO saturated Pt

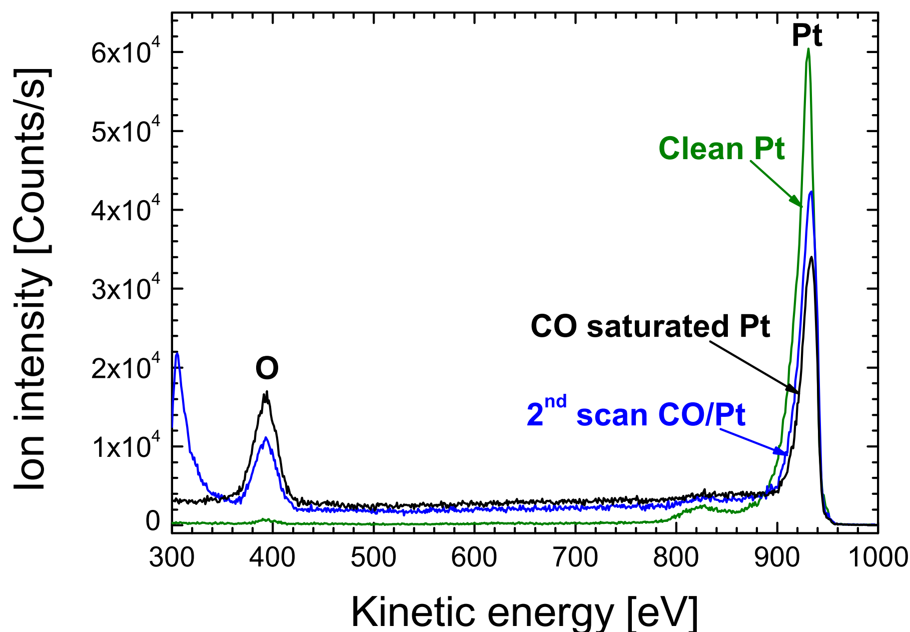

Figure 6.19: ISS spectra from a clean Pt surface (green), from the same surface saturated with CO (black) and a repeated scan (blue) to see the effect of sputtering of the surface. The adsorbed CO gives rise to an O peak at 395 eV and an attenuation of the Pt peak as compared to the clean surface. The CO coverage is seen to decrease with ion exposure, simply because CO molecules are sputtered off.

surface (black), and a repeated scan of the CO/Pt surface (blue) to see the effect of sputtering on the CO coverage. It takes about 12 min to complete a scan like this. The ISS spectrum of the freshly dosed, CO saturated surface is in terms of relative peak heights, shapes and background almost identical to spectra obtained in a neighboring UHV chamber, with very similar equipment and the same scattering geometry, on a CO saturated Pt(111) surface. This we regard supporting evidence, that the Pt surface is clean. The feature seen in the second scan of the CO/Pt surface (blue) is the charging effect discussed in Section 6.3.3.

Also the thermally induced desorption spectrum of ^{29}CO is interpreted as the fingerprint of a clean Pt surface. Figure 6.20 shows four TID spectra, successively obtained from the same sample. Thermal desorption spectra from a Pt(111) surface close to the saturation coverage of CO of 0.5 ML show a peak from CO desorbing from terraces at $\sim$110°C-140°C, depend-

ing on the heating rate, and a smaller peak at about 250° is CO desorbed from step sites [79–81]. Our TID curves show the same features as these spectra from more well-defined surfaces, which indicates that we do have a clean surface with a majority of (111) facets. Due to the lack of proper temperature measurements and control, we cannot extract more information from these measurements. The thermocouple temperature is ∼115°C when heating is turned off after 90 s in these measurements, but this value is an absolute lower limit to the real surface temperature and the heating rate is most likely not constant.

For this experiment dosing was done at 5×10^{-7} mbar for 1 min when the sample had cooled down to 44°C and during dosing the temperature dropped further 2°C. This gave reproducible uptakes as can be seen from the similarity of the graphs. Dosing at lower temperatures gave a strong dependence of the uptake on the exact temperature. When the sample is cooling, we are confident that the surface is in thermal equilibrium with the thermocouple, so that the temperature measurement can be trusted. The curves in Figure 6.20 are obtained after the following waiting times after dosing and in this order: 6 min (black), 6 min (green), 35 min (blue) and 165 min (orange). Curve integrals are given in the legend. This experiment demonstrates the reproducibility of these measurements from the same device, and further the stability of the adsorbed CO overlayer which sticks to the surface even after almost three hours. This latter fact enables us to do "batch" experiments for investigating HEFatS.

The principle of HEFatS "batch" experiments is to expose the adsorbates on the surface to hot electrons for a certain time span, and then detect the resulting products afterwards. This result is then compared to the result of a reference experiment of the same duration but without hot electron exposure. The result of the experiment conducted so far involving a CO saturated Pt surface exposed to hot electrons at a device bias voltage of 4.8 V for one hour is shown in Figure 6.21. The ^{29}CO TID curve from the freshly cleaned, CO-dosed sample is shown in black, and this measurement is repeated once as shown by the green curve. Then the reference experiment was made, where the device is just left in UHV for 1 hour after dosing before recording the TID curve shown in blue. Finally the device was run at 4.8 V for 1 hour with CO on the surface and then the TID curve shown in orange was obtained. During hot electron exposure the device current increased from 0.2 mA to 0.6 mA, but the bias voltage was sustained. In terms of reproducibility, the TID curves are not so good, because at this point we were dosing CO to a much lower device temperature (∼28°C) than in the experiments presented in Figure 6.20. Therefore the TID integrals, shown in the legend of the figure, are probably not comparable. It

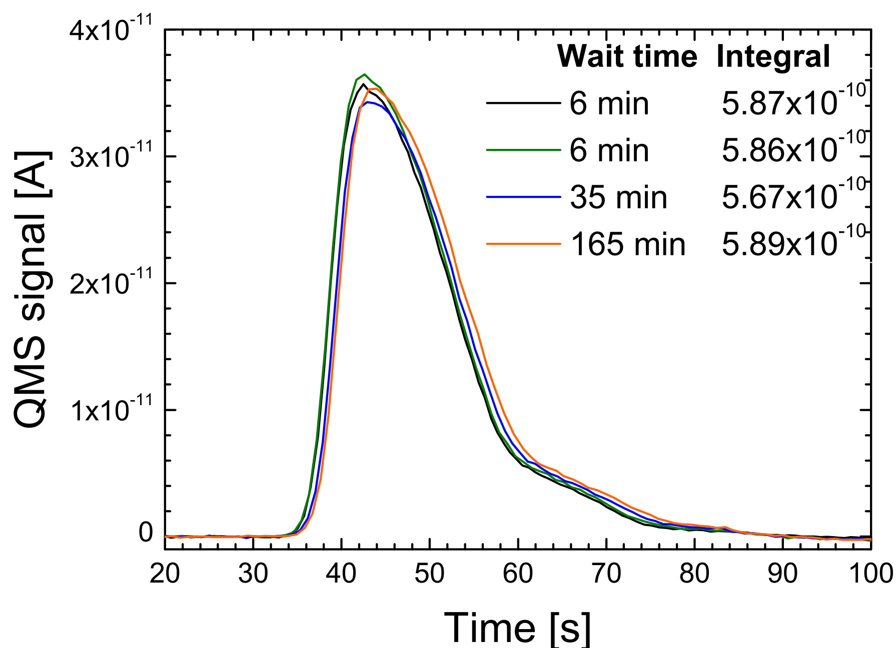

Figure 6.20: Four TID measurements taken by subsequent cycles of CO-dosing, heating along with mass detection and cool down on the same device. Dosing was done at 5×10^{-7} mbar for 1 min when the sample had cooled down to 44°C. The legend shows the waiting time for each measurement as well as the corresponding calculated TID integrals.

seems however, that there is one visible effect of the hot electron exposure and this is a change in curve shape. It is observed that heating the sample with the same power, as was done in this case, produces TID curves of very similar shape. It can however not be ruled out, that the hot electron current changes the morphology of the Pt film, which could lead to the observed change in TID curve shape. This experiment is frustratingly inconclusive, and should be repeated, but since CO desorption is a hard process to induce, we went on to investigate the effect on co-adsorbed O and CO.

Adsorbing O_2 dissociatively on Pt at room temperature should be straightforward, but it turned out not to be in our system. O_2 adsorption on various Pt surfaces has been extensively studied in the literature, for instance Pt(111) [82–84] and stepped surfaces [85; 86]. Above 150 K O_2 is seen to adsorb dissociatively with an initial sticking coefficient of 0.04-0.08 at 300 K on Pt(111) which is higher on stepped surfaces, but decreases

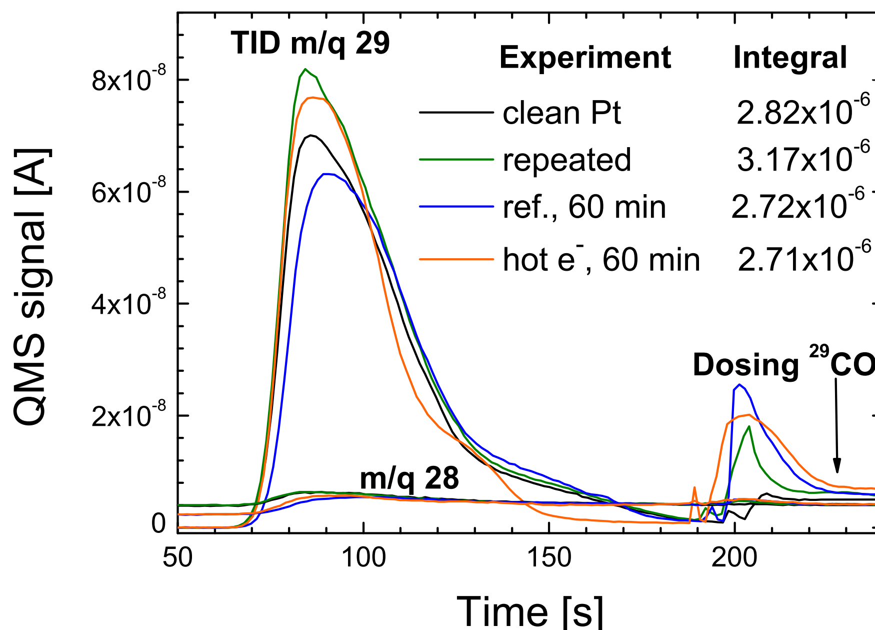

Figure 6.21: Comparison of ^{29}CO TID curves from a cleaned sample (black and green) to curves obtained after 1 hour of waiting time (blue) or hot electron exposure at 4.8 V (orange). Unfortunately CO dosing was done down to room temperature, so the reproducibility was not good as seen from the curves and the integrals. Comparing to Figure 6.20, the black, green and blue curves should be identical. The curve obtained after hot electron exposure is different in shape. The gain of the detector was increased to an absolute maximum for these measurements and this explains the large signals.

rapidly with coverage [84]. The saturation coverage lies somewhere between 0.2 and 0.5. Despite the decrease in sticking coefficient, saturation is attainable with reasonable exposures [85; 86]. There is general agreement, that dissociation and subsequent adsorption proceeds from a weakly bound, molecular chemisorbed state [82–84].

With these results in mind and our other experiments proving that we do have a clean Pt surface, it was quite surprising, that we have not been able to adsorb any reasonable amount of O on the surface. So far we have tried dosing in the chamber at pressures from 5×10^{-7} mbar to 5×10^{-5} mbar and exposures of thousands of L, both at room temperature and at 120°C to minimize CO adsorption from the chamber background. Only long exposure on the heated sample gave a just detectable signal in ISS, which is probably not due to CO because of the elevated temperature.

Otherwise ISS, XPS nor measurements of the mass signal of $^{45}CO_2$ when heating the O_2 dosed surface in ^{29}CO gave any indications of adsorbed O. O_2 exposures at ambient pressures of 0.2 bar-0.5 bar in the loadlock were even more fruitless. A quickly constructed experiment compared XPS O 1s lines after dosing 50 L O_2 without and with simultaneous exposure to hot electrons at a device bias voltage of 6 V. The background for this was to interact with the weakly bound molecular state which either becomes a precursor state for dissociation by transfer of negative charge from the surface, or is in itself negatively charged [84]. No detectable O-uptake was however seen. When writing this, we have neither solved the problem of getting O_2 to adsorb on Pt, nor have we identified the problem. One suspicion is the effect of contaminants on the surface or in the chamber which we have not been able to detect, like for instance an effect of the H_2 background.

Direct detection of desorption or reaction products is of course preferable and would yield the most information on the mechanisms of HEFatS. With the current setup we are not able to detect ^{29}CO desorption from a Pt device at a bias voltage of 4.8 eV directly with the QMS and this might well be a question of sensitivity. When testing, the gain of the SEM was set to the highest possible, and it was run in both standard current mode and in pulse count mode. At the time of writing this, a lock-in amplifier is being implemented for increasing the sensitivity.

6.6 Discussion of Systems for HEFatS

Throughout this project numerous ideas have come up concerning applicable test reactions. The desorption of NO from transition metal surfaces, for instance Pt, is a popular reaction in laser- and electron-stimulated femtochemistry at surfaces [11; 87]. We have done some preliminary experiments with NO on Pt, but we have encountered some difficulties with this system. First of all NO on Pt is not as stable at room temperature as CO on Pt and CO from the background will replace NO on the surface over time. This makes batch experiments more challenging. Furthermore, TID experiments with NO are by far not as reproducible and predictable as CO, and we have seen the apparent composition of the desorbates vary a lot between experiments. Experiments are being conducted to try to resolve the spectra, where there seem to be two sources of mass 28, one being CO the other N_2, though NO is not expected to dissociate on Pt at room temperature [88]. The QMS itself produces a signal of mass-to-ratio 28 of 3 % of the NO signal.

An essential problem with the current setup is the limited temperature range in which we can operate, especially towards the low temperature side. If the reactions are stable at room temperature, higher energies are needed for the hot electron induced reactions to occur. Of course the ultimate goal is to enhance the reactivity of "hard" reactions, not reactions which proceed spontaneously at room temperature. It would however be favorable to be able to unambiguously establish an effect of the tunneling hot electrons and then move on to more and more difficult reactions.

Some very interesting systems in that aspect are the alkyl halides (like methane or ethane with substitutions of one or more H's by the halides: F, Cl, Br or I). Chlorinated hydrocarbons were the choice of system for Sharpe, Palmer et al. [19] for inducing reactions in the gas phase by electrons from MIM electron emitters. These molecules are known to decompose by both low-energy electron [89] and photon interactions [90; 91], so they would make good test reactions. I have however not been able to find any reports on one of these systems being stable up to room temperature. It is the same problem with the compounds 2,4,6-trinitrotoluene (TNT) [92] and nitromethane [93; 94] on Pt, which we have also considered.

Chapter 7

Conclusion and Outlook

During this Ph.D. project a wide variety of experimental studies have been conducted as presented in this thesis. MOS devices for HEFatS and electron emission have been designed, produced and characterized. Characterization involves both tests of their functionality as hot electron sources as well as surface scientific studies of their surface. The accomplishments and conclusions are the following:

- MOS devices for producing hot electrons were designed and fabricated. The process sequence for producing them in the Danchip cleanroom facilities was developed, tested and optimized.
- A device holder and a sample holder interface were developed along with a loadlock- and sample transfer system for an existing UHV apparatus. The implementation of the MOS devices in UHV experiments was successful.
- The MOS devices were characterized by IV-curves which show Fowler-Nordheim tunneling characteristics at elevated device bias voltages, indicative of the tunneling of energetic electrons. Comparison of devices with different metals showed the expected shift of the IV curves due to different work functions.
- The energy distribution of the hot electrons at the metal-vacuum interface shows favorable, since a major part of the electron intensity has lost none or little energy as compared to the primary energy. This was seen from energy-resolved emission spectra, however with a cut-off at the metal work function.
- Pictures of the electron emission obtained with a Microchannel Plate stack with a phosphor screen show good homogeneity of emission

across the device surface. On the length scale of 50-100 μm there is some variation in emissivity, which is probably from the microstructure of the metal film or the surface local work function.

- Electron emission was observed in air, proving the devices' robustness in gas. The emission efficiencies are however low.

- Procedures for cleaning the surfaces of the top metal films of the devices were developed and cleanness of both Au and Pt films satisfactory for surface scientific studies was achieved. The cleaning sequence for Au films involves oxidation in a solution (RCA I) followed by mild O_2^+ sputtering in the UHV chamber. Pt films on the other hand should be exposed to ambient pressures of O_2 prior to insertion and can then be cleaned by heating in a background of O_2 in the chamber.

- Cs adsorption on Au was studied in terms of ISS, XPS and work function measurements. The relative Cs/Au XPS intensity corresponding to one monolayer of Cs as determined from ISS was found.

- The onset energy of electron emission was seen to follow the decrease in work function upon Cs adsorption. Unfortunately, Cs was seen to degrade the device oxide and alter the IV-characteristics, so we could not get information on the hot electron energy distributions at low energies. This also implies, that Cs deposition is not a viable method for increasing emission current for technical applications.

- CO adsorption on devices with Pt films was studied and thermal desorption experiments showed good agreement with literature reports on well-defined Pt single crystals. CO was also seen to be very stable on the surface at room temperature, and thermal desorption curves showed good reproducibility.

- Experiments with exposing CO on Pt to hot electrons did not prove a detectable effect of the hot electrons, possible because of lack of sensitivity, and were therefore inconclusive.

- NO adsorbed on Pt was not very stable at room temperature, and the desorbate compositions observed in thermal desorption experiments were seen to change, so right now this system seems less suited for HEFatS experiments on our devices.

7.1 Outlook

At the time of writing there are a number of things in progress with regards to detecting HEFatS on our devices. The possibility of measuring desorption induced by hot electrons directly is being explored by the implementation of lock-in technique for detection. Batch experiments of CO desorption from Pt can also be repeated with improved reproducibility of the CO dosing. The NO/Pt system is also being studied further.

A way of increasing the sensitivity for desorbing products would be to place a clean metal surface in close proximity to the device, which would adsorb all desorbed species from the device during hot electron exposure. A thermal desorption spectrum could then be made from this "integrator" at the end of the experiment. On the longer timescale one could consider the implementation of cooling of the devices in the chamber in order to gain access to other test reactions. The alkyl halides discussed in Section 6.6 decompose with a large probability of creating negatively charged halide ions which could be detected directly by the MCP, and there might be other reactions which produce charged products.

Appendix A

RCA Clean

Sequence

- RCA-1
- HF
- RCA-2
- HF

Each step is followed by rinsing in DI water.
The details for each step are given in the table below [58].

	RCA-1	RCA-2	HF
Purpose	Removal of organic species, metals and particles	Removal of alkali ions, metal complexes and metals	Removal of oxide
Solution	H_2O, NH_4OH(25-29 %), H_2O_2(30 %) (5:1:1)	H_2O, HCl(37 %), H_2O_2(30 %) (5:1:1)	5 % HF
Temperature	70-80°	70-80°	Room temperature
Time	10 min	10 min	30 s

Bibliography

[1] I. Chorkendorff and J. W. Niemantsverdriet, *Concepts of Modern Catalysis and Kinetics*. Wiley-VCH, 2003.

[2] P. Sabatier, "Hydrogenation et deshydrogenation par catalyse," *Berichte der Deutschen Chemischen Gesellschaft* **44** (1911) 1984.

[3] J. W. Gadzuk, "Inelastic resonance scattering, tunneling and desorption," *Phys. Rev. B* **44** (1991) 13466–13477.

[4] J. W. Gadzuk, "Resonance-assisted Hot Electron Femtochemistry at Surfaces," *Phys. Rev. Lett.* **76** (1996) 4234–4237.

[5] J. W. Gadzuk, "Resonance-assisted, hot-electron-induced desorption," *Surf. Sci.* **342** (1995) 345–358.

[6] N. Chakrabarti, V. Balasubramanian, N. Sathyamurthy, and J. W. Gadzuk, "Photoinduced desorption in NO/Pt: A time-dependent quantum mechanical study," *Chem. Phys. Lett.* **242** (1995) 490–498.

[7] J. A. Misewich, T. F. Heinz, and D. M. Newns, "Desorption induced by multiple electronic transitions," *Phys. Rev. Lett.* **68** (1992) 3737–3740.

[8] J. Gavnholt, T. Olsen, M. Engelund, and J. Schiøtz, "Δ self-consistent field method to obtain potential energy surfaces of excited molecules on surfaces," *Phys. Rev. B* **78** (2008) 075441.

[9] T. Olsen, J. Gavnholt, and J. Schiøtz, "Hot-electron-mediated desorption rates calculated from excited-state potential energy surfaces," *Phys. Rev. B* **79** (2009) 035403.

[10] J. Gavnholt, A. Rubio, T. Olsen, K. S. Thygesen, and J. Schiøtz, "Hot-electron-assisted femtochemistry at surfaces: A time-dependent density functional theory approach," *Phys. Rev. B* **79** (2009) 195405.

[11] S. A. Buntin, L. J. Richter, R. R. Cavanagh, and D. S. King, "Optically driven surface reactions: Evidence for the role of hot electrons," *Phys. Rev. Lett.* **61** (1988) 1321–1324.

[12] F. Budde, T. F. Heinz, M. M. T. Loy, J. A. Misewich, F. de Rougemont, and H. Zacharias, "Femtosecond time-resolved measurement of desorption," *Phys. Rev. Lett.* **66** (1991) 3024–3027.

[13] M. Bonn, S. Funk, C. Hess, D. N. Denzler, C. Stampfl, M. Scheffler, M. Wolf, and G. Ertl, "Phonon- versus electron-mediated desorption and oxidation of CO on Ru(0001)," *Science* **285** (1999) 1042–1045.

[14] B. C. Stipe, M. A. Rezaei, and W. Ho, "Atomistic studies of O_2 dissociation on Pt(111) induced by photons, electrons, and by heating," *J. Chem. Phys.* **107** (1997) 6443–6447.

[15] P. A. Sloan and R. E. Palmer, "Two-electron dissociation of single molecules by atomic manipulation at room temperature," *Nature* **434** (2005) 367–371.

[16] W. Haidinger and J. Figar, "The acceleration of a catalyzed reaction by hot electrons," *Chem. Phys. Lett.* **11** (1971) 545–551.

[17] J. Figar and W. Haidinger, "Activity enhancement and selectivity change in propene oxidation by the catalytic effect of hot electrons," *Chem. Phys. Lett.* **19** (1973) 564–570.

[18] W. Haidinger, "Process for catalyzing chemical reactions." 4,092,227 United States Patent, 1976. Original Swiss patent 16476/71 from 1971.

[19] R. G. Sharpe, S. J. Dixon-Warren, P. J. Durston, and R. E. Palmer, "The electronic catalyst: dissociation of chlorinated hydrocarbons by metal-insulator-metal electron emitters," *Chem. Phys. Lett.* **234** (1995) 354–358.

[20] R. G. Sharpe and R. E. Palmer, "The gas sensitivity of device and emission currents in an electroformed MIM device," *J. Phys. D: Appl. Phys.* **29** (1996) 837–842.

[21] T. Wadayama, A. Kojim, and A. Hatta, "Bias-voltage-induced decomposition of 2-methyl-1,4-naphthoquinone on Ag/AlO_x/Al tunnel junction," *Appl. Phys. A* **79** (2004) 1891–1894.

[22] T. Wadayama and M. Yokawa, "Hot-electron assisted reaction of p-nitrobenzoic acid adsorbed on metal-insulator-metal tunnel junction's electrode surface," *Chem. Phys. Lett.* **428** (2006) 348–351.

[23] D. Diesing, G. Kritzler, M. Stermann, D. Nolting, and A. Otto, "Metal/insulator/metal junctions for electrocemical surface science," *J. Solid State Electrochem.* **7** (2003) 389–415.

[24] N. Koshida, T. Ohta, and B. Gelloz, “Operation of nanosiliscon ballistic electron emitter in liquid water and hydrogen generation effect,” *Appl. Phys. Lett.* **90** (2007) 163505.

[25] H. Nienhaus, H. S. Bergh, B. Gergen, A. Majumdar, W. H. Weinberg, and E. W. McFarland, “Electron-hole pair creation at Ag and Cu surfaces by adsorption of atomic hydrogen and deuterium,” *Phys. Rev. Lett.* **82** (1999) 446–449.

[26] B. Gergen, H. Nienhaus, W. H. Weinberg, and E. W. McFarland, “Chemically induced electronic excitations at metal surfaces,” *Science* **294** (2001) 2521–2523.

[27] J. Y. Park and G. A. Somorjai, “The catalytic nanodiode: Detecting continous electron flow at oxide-metal interfaces generated by a gas-phase exothermic reaction,” *Chem. Phys. Chem.* **7** (2006) 1409–1413.

[28] X. Liu, B. Roldan Cuenya, and E. W. McFarland, “A MIS device structure for detection of chemically induced charge carriers,” *Sensors Actuators B* **99** (2004) 556–561.

[29] D. A. Neamen, *Semiconductor Physics and Devices: Basic Principles*. McGraw-Hill, 3 ed., 2003.

[30] H. L. Skriver and N. M. Rosengaard, “Surface energy and work function of elemental metals,” *Phys. Rev. B* **46** (1992) 7157–7168.

[31] R. H. Fowler and L. W. Nordheim, “Electron emission in intense electric fields,” *Proc. R. Soc. A* (1928) 173–181.

[32] B. H. Bransden and C. J. Joachain, *Quantum Mechanics*. Pearson Education, Ltd., 2 ed., 2000.

[33] M. Lenzlinger and E. H. Snow, “Fowler-Nordheim tunneling into thermally grown SiO_2,” *J. Appl. Phys.* **40** (1969) 278–283.

[34] Z. A. Weinberg, “On tunneling in metal-oxide-silicon structures,” *J. Appl. Phys.* **53** (1982) 5052–5056.

[35] L. W. Nordheim, “The effect of the image force on the emission and reflexion of electrons by metals,” *Proc. R. Soc. A* **121** (1928) 626–639.

[36] R. G. Forbes, “Physics of genralized Fowler-Nordheim-type equations,” *J. Vac. Sci. Technol. B* **26** (2008) 788–793.

[37] R. H. Good Jr. and E. W. Müller, *’Field emission’, Elektronen-Emission Gasentladungen I*, vol. 21 of *Handbuch der Physik*. Springer-Verlag, 1956.

[38] C. R. Crowell and S. M. Sze, “Ballistic mean free path measurements of hot electrons in Au films,” *Phys. Rev. Lett.* **15** (1965) 659–661.

[39] H. Kanter, “Slow-electron mean free paths in aluminum, silver, and gold ,” *Phys. Rev. B* **1** (1970) 522–536.

[40] J. J. Quinn, “Range of excited electrons in metals,” *Phys. Rev.* **126** (1962) 1453–1457.

[41] Z. J. Ding and R. Shimizu, “Inelastic collisions of kV electrons in solids,” *Surf. Sci.* **222** (1989) 313–331.

[42] C. A. Mead, “Operation of tunnel-emission devices,” *J. Appl. Phys.* **32** (1961) 646–652.

[43] D. J. DiMaria and M. V. Fischetti, “Vacuum emission of hot electrons from silicon dioxide at low temperatures,” *J. Appl. Phys.* **64** (1988) 4683–4691.

[44] K. Yokoo, S. Sato, G. Koshita, I. Amano, J. Murota, and S. Ono, “Energy distribution of tunneling emission from Si-gate metal-oxide-semiconductor cathode,” *J. Vac. Sci. Technol. B* **12** (1994) 801–805.

[45] H. Adachi, “Emission characteristics of metal-insulator-metal tunnel cathodes,” *J. Vac. Sci. Technol. B* **14** (1996) 2093–2095.

[46] H. J. Fitting, T. Hingst, and E. Schreiber, “Breakdown and high-energy electron vacuum emission of MIS-structures,” *J. Phys. D: Appl. Phys.* **32** (1999) 1963–1970.

[47] K. Yokoo, H. Tanaka, S. Sato, J. Murota, and S. Ono, “Emission characteristics of metal-oxide-semiconductor electron tunneling cathode,” *J. Vac. Sci. Technol. B* **11** (1993) 429–432.

[48] H. Mimura, Y. Neo, H. Shimawaki, T. Matsumo, and K. Yokoo, “Emission characteristics and applications of semiconductor field emitters,” *Appl. Surf. Sci.* **244** (2005) 498–503.

[49] J. Cohen, "Tunnel emission into vacuum," *J. Appl. Phys.* **33** (1962) 1999–2000.

[50] J. Drucker and P. K. Hansma, "Emission of energetic electrons from tunnel junctions," *Phys. Rev. B* **30** (1984) 4348–4350.

[51] H. Mimura, Y. Neo, H. Shimawaki, Y. Abe, K. Tahara, and K. Yokoo, "Improvement of the emission current from a cesiated metal-oxide-semiconductor cathode," *Appl. Phys. Lett.* **88** (2006) 123514.

[52] A. Govyadinov, T. Novet, D. Pidwerbecki, S. Ramamoorthi, J. Smith, J. Chen, C. Otis, D. Neiman, and P. Benning, "Polysilicon metal-insulator-semiconductor electron emitter," *J. Vac. Sci. Technol. B* **23** (2005) 853–863.

[53] J. Cohen, "Tunnel emission into vacuum II," *Appl. Phys. Lett.* **1** (1962) 61–62.

[54] M. Poppeller, E. Cartier, and R. M. Tromp, "Hot Electron Emission Lithography: A method for efficient large area e-beam projection," *Microelectronic Engineering* **46** (1999) 183–186.

[55] N. Negishi, T. Nakada, K. Sakemura, Y. Okuda, H. Satoh, A. Watanabe, T. Yoshikawa, K. Ogasawara, and N. Koshida, "Characterization of an advanced high efficiency electro-emission device," *J. Vac. Sci. Technol. B* **23** (2005) 682–686.

[56] N. Negishi, T. Sato, Y. Matsuba, R. Tanaka, T. Nakada, K. Sakemura, Y. Okuda, A. Watanabe, T. Yoshikawa, K. Ogasawara, M. Nanba, S. Okazaki, K. Tanioka, E. N., and N. Koshida, "Development of a super-high-sensitivity image sensor using 640×480 pixel active-matrix high-efficiency electron emission device," *J. Vac. Sci. Technol. B* **26** (2008) 711–715.

[57] J. D. Plummer, M. D. Deal, and P. B. Griffin, *Silicon VLSI Technology - Fundamentals, Practice and Modeling*. Prentice Hall, 2000.

[58] W. Kern, *Handbook of Semiconductor Wafer Cleaning Technology - Science, Technology, and Applications*. William Andrew Publishing/Noyes, 1993.

[59] L. Michalski, K. Eckersdorf, J. Kucharski, and J. McGhee, *Temperature Measurement*. John Wiley & Sons Ltd, 2 ed., 2001.

[60] H. Niehus, W. Heiland, and E. Taglauer, “Low-energy ion scattering at surfaces,” *Surf. Sci. Rep.* **17** (1993) 213–303.

[61] F. D. Richardson and J. H. E. Jeffes, “The thermodynamics of substances of interest in iron and steel making from 0°C to 2400°C,” *J. Iron Steel Inst.* **160** (1948) 261–270.

[62] M. Prietsch, “Ballistic-electron emission microscopy (BEEM): Studies of metal/semiconductor interfaces with nanometer resolution,” *Phys. Rep.* **253** (1995) 163–233.

[63] C. D. Wagner, W. M. Riggs, L. E. Davis, and J. F. Moulder, *Handbook of X-Ray Photoelectron Spectroscopy*. Perkin Elmer Coorporation, Physical Electronic Division, 1979.

[64] L. C. A. van den Oetelaar, S. N. Mikhailov, and H. H. Brongersma, “Mechanism of neutralization in low-energy He^+ ion scattering from carbidic and graphitic carbon species on rhenium,” *Nucl. Instr. and Meth. B* **85** (1994) 420–423.

[65] J. J. Pireaux, M. Liehr, P. A. Thiry, J. P. Delrue, and R. Caudano, “Electron spectroscopic characterization of oxygen adsorption on gold surfaces II: Production of gold oxide in oxygen DC reactive sputtering,” *Surf. Sci.* **141** (1984) 221–232.

[66] J. M. Gottfried, N. Elghobashi, S. L. M. Schroeder, and K. Christmann, “Oxidation of gold by oxygen-ion sputtering,” *Surf. Sci.* **523** (2003) 89–102.

[67] H. H. Brongersma, M. Draxler, M. de Ridder, and P. Bauer, “Surface composition analysis by low-energy ion scattering,” *Surf. Sci. Rep.* **62** (2007) 63–109.

[68] R. Błaszczyszyn, M. Błaszczyszyn, and R. Męclewski, “Work function of the adsorption system of potassium on tungsten,” *Surf. Sci.* **51** (1975) 396–408.

[69] N. D. Lang, “Theory of work-function changes induced by alkali adsorption,” *Phys. Rev. B* **4** (1971) 4234–4244.

[70] R. W. Verhoef and M. Asscher, “The work function of adsorbed alkalis on metals revisited: A coverage-dependent polarizability approach,” *Surf. Sci.* **391** (1997) 11–18.

[71] R. Cortenraad, A. W. Denier van der Gon, H. H. Brongersma, S. N. Ermolov, and V. G. Glebovsky, "Work function dependent neutralization of low energy noble gas ions," *Phys. Rev. B* **65** (2002) 195414.

[72] P. Wenter and N. Memmel, "Anomalous adsorption of potassium on Pt(111): A study by low-energy ion scattering," *Surf. Sci.* **513** (2002) L419–L424.

[73] M. Beckschulte and E. Taglauer, "The influence of work function changes on the charge exchange in low-energy ion scattering," *Nucl. Instr. and Meth. B* **78** (1993) 29–37.

[74] M. J. Ashwin and D. P. Woodruff, "Charge exchange processes in Li^+ and He^+ ion scattering from alkali adsorbates on Cu(110)," *Surf. Sci.* **244** (1991) 247–258.

[75] L. Q. Jiang, Y. D. Li, and B. E. Koel, "Trajectory dependent neutralization of low energy Li^+ scattered from alkali adsorbates on Ni(111)," *Phys. Rev. Lett.* **70** (1993) 2649–2652.

[76] J. A. Rodriguez, J. Hrbek, Y. W. Yang, M. Kuhn, and T. K. Sham, "Photoemission and thermal desorption studies of Cs-Au and Li-Au films on Ru(001)," *Surf. Sci.* **293** (1993) 260–274.

[77] J. L. LaRue, J. D. White, N. H. Nahler, Z. Liu, Y. Sun, P. A. Pianetta, D. J. Auerbach, and A. M. Wodtke, "The work function of submonolayer cesium-covered gold: A photoelectron spectroscopy study," *J. Chem. Phys.* **129** (2008) 024709.

[78] J. Hrbek, Y. W. Yang, and J. A. Rodriguez, "Oxidation of cesium multilayers," *Surf. Sci.* **296** (1993) 164–170.

[79] G. Ertl, M. Neumann, and K. M. Streit, "Chemisorption of CO on the Pt(111) surface," *Surf. Sci.* **64** (1977) 393–410.

[80] P. R. Norton, J. W. Goodale, and E. B. Selkirk, "Adsorption of CO on Pt(111) studied by photoemission, thermal desorption spectroscopy and high resolution dynamic measurements of work function," *Surf. Sci.* **83** (1979) 189–227.

[81] C. T. Campbell, G. Ertl, H. Kuipers, and J. Segner, "A molecular beam investigation of the interactions of CO with a Pt(111) surface," *Surf. Sci.* **107** (1981) 207–219.

[82] H. P. Bonzel and R. Ku, "On the kinetics of oxygen adsorption on a Pt(111) surface," *Surf. Sci.* **40** (1973) 85–101.

[83] C. T. Campbell, G. Ertl, H. Kuipers, and J. Segner, "A molecular beam study of the adsorption and desorption of oxygen from a Pt(111) surface," *Surf. Sci.* **107** (1981) 220–236.

[84] A. C. Luntz, M. D. Williams, and D. S. Bethune, "The sticking of O_2 on a Pt(111) surface," *J. Chem. Phys.* **89** (1988) 4381–4395.

[85] J. L. Gland and V. N. Korchak, "The adsorption of oxygen on a stepped platinum single crystal surface," *Surf. Sci.* **75** (1978) 733–750.

[86] N. Freyer, M. Kiskinova, G. Pirug, and H. P. Bonzel, "Oxygen adsorption on Pt(110)-(1$\times$2) and Pt(110)-(1$\times$1)," *Surf. Sci.* **166** (1986) 206–220.

[87] U. Heiz, J. Xu, J. W. Gadzuk, and J. T. Yates Jr., "NO electronic desorption processes from step sites on Pt(112): A comparison between photo- and electron-stimulated desorption ," *J. Chem. Phys.* **101** (1994) 4373–4378.

[88] H. Falsig, J. Bligaard, T. Rass-Hansen, A. L. Kustov, C. H. Christensen, and J. K. Nørskov, "Trends in catalytic NO decomposition over transition metal surfaces," *Topics Cat.* **45** (2007) 117–120.

[89] X. L. Zhou, P. M. Blass, B. E. Koel, and J. M. White, "Low energy electron induced chemistry: CH_3Cl on Ag(111)," *Surf. Sci.* **271** (1992) 427–451.

[90] V. A. Ukraintsev, T. J. Long, and I. Gowl, T. Harrison, "Photoinduced dissociative electron attachment of CH_3Br on Pt(111): The role of the local work function," *J. Chem. Phys.* **96** (1992) 9114–9121.

[91] X. L. Zhou and J. M. White, "Alkyl halide photochemistry on Ag(111): II. Methyl bromide," *Surf.Sci.* **241** (1991) 259–269.

[92] H. C. Peebles, J. M. White, F. J. Conrad, and J. W. Rogers Jr., "Desorption and decomposition of 2,4,6-trinitrotoluene adsorbed on Pt(111)," *Appl. Surf. Sci.* **20** (1985) 512–526.

[93] S. Y. Hwang, A. C. F. Kong, and L. D. Schmidt, "CH_3NO_2 decomposition on Pt(111)," *Surf. Sci.* **217** (1989) 179–198.

[94] N. Saliba, J. Wang, B. A. Bansenbauer, and B. E. Koel, "Adsorption and reaction of nitromethane(CH_3NO_2) on Pt(111)," *Surf. Sci.* **389** (1997) 147–161.

List of Symbols

Symbol	Description
A	Constant in Fowler-Nordheim expression
B	Constant in Fowler-Nordheim expression
C_{MOS}	Capacitance of MOS structure
C_{ox}	Capacitance of oxide layer
C_{S}	Capacitance of accumulation layer
γ	Photon energy
ΔE	Energy window of detection of HSA
$\Delta E(\tau_{\mathrm{R}})$	Energy gain of adsorbate
e	Electron charge magnitude
E_{Bind}	Binding energy
E_{C}	Conduction bandedge
E_{g}	Band gap
$E_{\mathrm{in}}/E_{\mathrm{fin}}$	Energy of electron when tunneling into/out of adsorbate
$E_{\mathrm{in}}/E_{\mathrm{out}}$	Kinetic energy of incoming/outgoing ion
E_{F}	Fermi level
E_{Kin}	Kinetic energy
E_{V}	Valence bandedge
F_{ox}	Electric field in oxide
$\hbar$	Reduced Planck's constant
θ	Scattering angle
I	Current
J_{FN}	Fowler-Nordheim current density
λ	Electron mean free path
M_{ion}	Mass of ion
m_{ox}	Electron effective mass in SiO_2
m_{Si}	Electron effective mass in Si
M_{target}	Mass of target atom
N_{d}	Doping density
t_{M}	Thickness of metal
t_{ox}	Thickness of oxide
τ_{R}	Residence time of electron on adsorbate

V_-	Potential energy for negative-ion state
V_0	Potential energy for electronic ground state
V_{FB}	Flat band voltage
$V_{\mathrm{FN,on}}$	Voltage for onset of Fowler-Nordheim tunneling
V_{g}	Gate voltage
V_{ox}	Voltage drop across oxide
V_{scan}	Scanning voltage on sample
Φ	Work function
ϕ_0	Barrier height
Φ_{A}	Work function of analyzer
Φ_{M}	Work function of metal
ϕ_{S}	Surface potential
χ_{ox}	Electron affinity of SiO_2
χ_{Si}	Electron affinity of Si

List of Abbreviations

BEEM	Ballistic Electron Emission Microscopy
CCD	Charge-Coupled Device
CINF	Center for Individual Nanoparticle Functionality
CV	Capacitance-voltage
DAQ	Data Acquisition
DC	Direct current
DFT	Density Functional Theory
DIET	Desorption Induced by Electronic Transitions
DIMET	Desorption Induced by Multiple Electronic Transitions
DTU	Technical University of Denmark
ΔSCF	Δ Self-Consistent Field
FN	Fowler-Nordheim
HEEL	Hot Electron Emission Lithography
HEFatS	Hot Electron Femtochemistry at Surfaces
HSA	Hemispherical Analyzer
HV	High Voltage
ISS	Ion Scattering Spectroscopy (same as LEIS)
IV	Current-voltage
LEIS	Low-Energy Ion Scattering (same as ISS)
MCP	Microchannel Plate
MIM	Metal-Insulator-Metal
MIS	Metal-Insulator-Semiconductor
MOS	Metal-Oxide-Semiconductor
PVD	Physical Vapor Deposition
QMS	Quadrupole Mass Spectrometer
RF	Radio Frequency
SEM	Secondary Electron Multiplier or Scanning Electron Microscopy
STM	Scanning Tunneling Microscopy

TID	Thermally Induced Desorption
TPD	Temperature Programmed Desorption
UHV	Ultra High Vacuum
WKB	Wenzel-Kramer-Brillouin
XGA	Extended Graphics Array (1024×768 pixels resolution)
XPS	X-ray Induced Photoelectron Spectroscopy

List of Papers

List of included papers [A]-[C]

[A] G. Nielsen, L. B. Thomsen, M. Johansson, O. Hansen, I. Chorkendorff, "Electron emission from MOS electron emitters with clean and cesium covered gold surface", *Appl. Surf. Sci.* **255** (2009) 7657-7662.

[B] L. B. Thomsen, G. Nielsen, S. B. Vendelbo, M. Johansson, O. Hansen, I. Chorkendorff, "Electron emission from ultralarge area metal-oxide-semiconductor electron emitters", *J. Vac. Sci. Technol. B* **27** (2009) 562.

[C] L. B. Thomsen, G. Nielsen, S. B. Vendelbo, M. Johansson, O. Hansen, I. Chorkendorff, "Ultralarge area MOS tunnel devices for electron emission", *Phys. Rev. B* **76** (2007) 155315.

List of other papers [D]-[H]

[D] M. Johansson, E. Skúlason, G. Nielsen, S. Murphy, R. M. Nielsen, I. Chorkendorff, "Hydrogen adsorption on palladium and palladium hydride at 1 bar", submitted to *Surf. Sci*, 2009.

[E] J. Engbæk, G. Nielsen, J. H. Nielsen, I. Chorkendorff, "Decomposition of lithium amide and imide films on nickel", *Surf. Sci.* **601** (2007) 830.

[F] J. Engbæk, G. Nielsen, J. H. Nielsen, I. Chorkendorff, "Growth and decomposition of lithium and lithium hydride on nickel", *Surf. Sci.* **600** (2006) 1468-1474.

[G] F. Abild-Pedersen, O. Lytken, J. Engbæk, G. Nielsen, I. Chorkendorff, J. K. Nørskov, "Methane activation on Ni(111): Effects of poisons and step defects", *Surf. Sci.* **590** (2005) 127.

[H] M. Andersen, O. Lytken, J. Engbæk, G. Nielsen, N. Schumacher, M. Johansson, I. Chorkendorff, "Search for new catalysts from a fundamental basis", *Catalysis Today* **100** (2005) 191.

Paper A

Applied Surface Science 255 (2009) 7657–7662

Contents lists available at ScienceDirect

Applied Surface Science

journal homepage: www.elsevier.com/locate/apsusc

Electron emission from MOS electron emitters with clean and cesium covered gold surface

Gunver Nielsen [a], Lasse Bjørchmar Thomsen [a], Martin Johansson [a], Ole Hansen [a,b], Ib Chorkendorff [a,*]

[a] Center for Individual Nanoparticle Functionality (CINF), Department of Physics, Technical University of Denmark, DK-2800 Kgs. Lyngby, Denmark
[b] Department of Micro- and Nanotechnology, Technical University of Denmark, DTU Nanotech Building 345E, DK-2800 Kgs. Lyngby, Denmark

ARTICLE INFO

Article history:
Received 26 February 2009
Received in revised form 14 April 2009
Accepted 14 April 2009
Available online 21 April 2009

Keywords:
Electron emission
Work function
MOS
UHV

ABSTRACT

MOS (metal-oxide-semiconductor) electron emitters consisting of a Si substrate, a SiO_2 tunnel barrier and a Ti (1 nm)/Au(7 nm) top-electrode, with an active area of 1 cm^2 have been produced and studied with surface science techniques under UHV (ultra high vacuum) conditions and their emission characteristics have been investigated. It is known, that deposition of an alkali metal on the emitting surface lowers the work function and increases the emission efficiency. For increasing Cs coverages the surface has been characterized by X-ray Photoelectron Spectroscopy (XPS), Ion Scattering Spectroscopy (ISS) and work function measurements. Energy spectra of electron emission from the devices under an applied bias voltage have been recorded for the clean Au surface and for two Cs coverages and simultaneous work function curves have been obtained. The electron emission onset is seen to appear at the surface work function. A method for cleaning the ex situ deposited Au top electrodes to a degree satisfactory to surface science studies has been developed, and a threshold for oxide damage by low-energy ion exposure between 0.5 and 1 keV has been determined.

© 2009 Elsevier B.V. All rights reserved.

1. Introduction

Free electron emitters find application in many technological and scientific branches. Tunnel emitters have been investigated and developed for several decades for applications where hot cathodes and field effect emitters [1] cannot be applied. Hot cathodes suffer from outgassing, extensive heat generation and light emission and they can only be operated in vacuum. The use of field effect emitters eliminates most of these drawbacks, but they too are not robust in the presence of gas, due to ionization of the gas molecules by the emitted electrons which can lead to either discharges or sputtering of the cathode [1].

Tunnel emitters consist of two electrodes (metal or semiconductor) separated by an insulating layer. When a bias voltage is applied between the two electrodes, electrons will be able to tunnel through the insulator, and if the bias voltage is high enough they may gain sufficient energy to escape the work function of the top-electrode, which should be as thin as possible to reduce energy loss by scattering.

In the early sixties electron emission from MIM (metal-insulator-metal) devices was demonstrated [2–4]. Extensive studies of both MIM and MIS (metal-insulator-semiconductor) tunnel emitters produced in various ways have contributed to the understanding of the transport mechanisms and emission characteristics of tunnel emitters and explored ways to improve the efficiency [5–16]. A well known and commonly used way of improving the emissivity of the devices is lowering the work function of the top-electrode by cesiation [15,16]. The shortcomings of this type of electron emitters are the emission efficiency and the lifetime, whereas the insensitivity to gas pressure has been demonstrated [16,17]. The versatility of this type of cold cathode is demonstrated in the various uses, like for instance maskless e-beam lithography [18], electron sources in electron microscopes [19] and for flat panel displays [11].

MIM and MIS tunnel devices as well as Schottky diodes have recently attracted much attention as detectors for currents of chemically induced hot carriers. Detection of such chemicurrents has been reported from molecular adsorption events on MIS devices [20,21], associative desorption events on MIM devices [22] and oxidation reactions on Schottky diodes [23]. Also the response of tunnel devices to carrier excitation by ion impact is a field of interest [24,25].

We have developed Si–SiO_2–Au MOS (metal-oxide-semiconductor) devices to be used for hot electron femtochemistry at surfaces (HEFatS) [26]. These devices have an ultra-large oxide area of 1 cm^2 in order to generate a detectable amount of products from hot electron induced reactions at the surface. The MOS-devices show excellent electrical properties [27], and their capability as

* Corresponding author. Tel.: +45 45 25 31 70; fax: +45 45 93 23 99.
E-mail address: ibchork@fysik.dtu.dk (I. Chorkendorff).

0169-4332/$ – see front matter © 2009 Elsevier B.V. All rights reserved.
doi:10.1016/j.apsusc.2009.04.046

electron emitters has also been investigated [17]. Studies of emission spectra of the devices can reveal how energetic the electrons available for inducing surface reactions are, and by lowering the work function of the devices, electrons at lower energy can be emitted to vacuum. This article presents an investigation of Cs deposited on thin Au-films using surface science techniques, along with more detailed studies of the emission characteristics of devices with well-defined, clean and Cs covered Au surfaces.

2. Experimental

2.1. Fabrication of tunnel emitters

The tunnel emitters investigated in this work were fabricated in the Danchip cleanroom facilities at the Technical University of Denmark using standard silicon processing technologies. The substrates are heavily doped n-type (0.025 Ωcm, Sb-doped) Si wafers. A 0.75 μm thick oxide was grown by wet thermal oxidation at 1000 $^\circ$ C to serve as a stable underlayer for making electrical contact to the devices. The thick oxide was etched back in buffered hydrofluoric acid (bHF) in order to open 1 cm $\times$ 1 cm large active areas. Masking was done by standard photolithography. The tunnel oxide was grown in dry oxygen at 800 °C, and annealed at the same temperature for 20 min in nitrogen. This yields a high quality oxide with a thickness of $\sim$5–6 nm. The top-electrode is a Ti wetting layer only 1 nm thick and a thin gold film, 7 nm thick, deposited by physical vapor deposition (PVD) in an e-beam evaporator at a base pressure of 1×10^{-6} mbar. The area was defined by a shadow mask. The process is described in more detail in [27]. A schematic drawing of the cross section of a single device is shown in the inset of Fig. 1. After scribing and dicing of the wafers the devices were cleaned for 4 min in RCA I [29] solution at room temperature and rinsed in water, before insertion into UHV. This cleaning procedure removes a major part of the carbon containing film covering the gold surface, and makes it possible to clean the top metal surface in situ to a degree satisfactory for surface science studies.

2.2. UHV chamber

All experiments were carried out in a standard ultra high vacuum (UHV) chamber with a base pressure of 8×10^{-11} mbar, see Fig. 1. The chamber is equipped with a loadlock system and a wobblestick, facilitating quick exchange of samples without breaking vacuum. Through the sample stage on the manipulator there are isolated connections to the front contacts on both sides of the device and to the back electrode, a thermocouple in contact with the backside and a shielded tungsten filament underneath the sample capable of heating the sample to 550 K. The UHV chamber further includes a hemispherical analyzer (HSA) (VSW HA100), an X-ray gun with Mg and Al anodes (VSW Twin Anode X-ray Source), a Quadrupole Mass Spectrometer (Baltzer 125), a Cs-getter (SAES) mounted in a water cooled housing with a flag, and two identical differentially pumped ion guns (Perkin Elmer Phi 04-300). One ion gun is operated when doing Ion Scattering Spectroscopy (ISS), the other one has a smaller incidence angle on the sample and is used for cleaning the sample with low-energy oxygen ions. Operation in O_2 slowly burns the filament, so the ion current cannot be kept constant and the filaments are replaced frequently.

X-ray Photoelectron Spectroscopy (XPS) spectra were obtained using the Mg anode for excitation and at a constant pass energy through the HSA of 50 eV. The work function of the analyzer has been determined from the position of the Au $4f_{7/2}$ line, and this value determines the position of the binding energy scale. Work function measurements on the sample were performed by energy analysis of the low-energy cut-off of the secondary electrons produced by irradiation with X-rays from the Mg anode. The sample was biased negatively to ~ -25 V relative to the grounded HSA entrance. A small negative bias voltage is needed for the

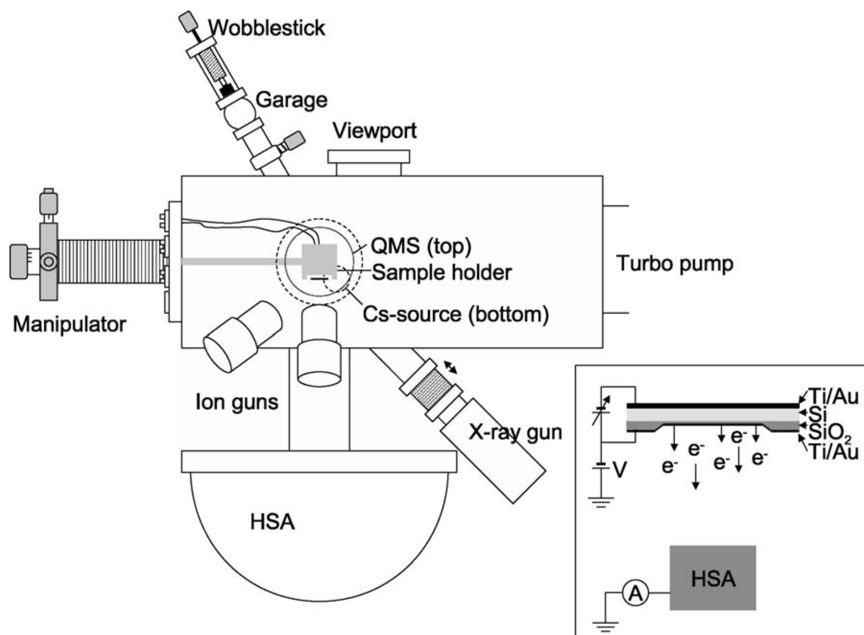

Fig. 1. A schematic overview of the UHV chamber. Samples mounted in special sample holders facilitating electrical contact and electrical isolation from the chamber are transferred from the garage to the sample stage in the center of the chamber using the wobblestick. The sample stage can be moved in all three directions and rotated 360°. The chamber has a hemispherical analyzer (HSA), two identical, differentially pumped ion guns and an X-ray gun placed on one side. A Cs-getter is mounted in a water cooled Cu-housing at the bottom of the chamber. The chamber further has a Quadrupole Mass Spectrometer (QMS) at the top of the chamber. The inset (not drawn to scale) depicts the structure of a single device consisting of a Si-substrate, a very thin SiO_2 tunnel barrier and the thicker contact pads, and the top and bottom metallization. By applying a bias voltage to the device, electrons can be emitted into vacuum and detected by the HSA, only shown schematically. The detected electrons are amplified by the channeltron at the end of the HSA and the current is detected by an ammeter. The front of the device is biased negatively relative to ground/the HSA.

emitted electrons to overcome the work function of the analyzer when this is larger than the work function of the emitting surface. A higher bias voltage should minimize the effects of space charge and magnetic fields on the paths of the electrons to the analyzer, but is in practice not necessary, since equivalent spectra could be obtained along with the emission spectra at a much lower relative bias voltage.

ISS was performed with 1 keV He ions at a constant pass energy of the HSA of 125 eV. Ion currents of around 80 nA to the sample were achieved, and once the temperature of the ion gun had been allowed to stabilize with the filament on, this current was constant. It could be controlled to within a few percent by regulating the He pressure according to the ion gauge readings. The extractor voltage was only turned on when recording spectra, in this way care was taken to limit the ion exposure time of the sample in order to minimize sputtering effects. The scattering angle was 135° with detection along the surface normal. Cs deposition was done by driving a constant current of 7.2 A through the getter. Before each dose the getter was outgassed for 2 min and the timing of the doses was controlled by turning a flag in front of the getter, dosing from 30 s and up to 20 min.

The emitted electrons were detected using the HSA, set up for a pass energy of 1 eV which was only possible using a home build, LabVIEW controlled voltage supply. The selection energy of the HSA was kept constant during measurements and the bias on the top-electrode relative to the HSA was scanned to complete an energy spectrum of the emitted electrons. This is equivalent to normal operation, where the sample is grounded, and the retarding potential of the HSA is scanned, but technically much easier to set up in this special case. The entry plate of the HSA which controls the retardation of the electrons was kept at −4 V with respect to ground, so that an electron accelerated to 5 eV with respect to the Fermi level of the Si substrate would be retarded to 1 eV kinetic energy and detected. An energy diagram of the sample and the analyzer is shown in Fig. 2 a, and for clarity Fig. 2 b shows an emission spectrum and the corresponding work function measurement. During these measurements all filaments and light sources in the chamber were turned off and all viewports were blocked, in order to minimize the background of electrons at these low kinetic energies and to eliminate the signal from photoexcited electrons, which we could otherwise detect from the device.

2.3. Cleaning the Au surface

One of the challenges when producing samples under cleanroom conditions and transferring them to UHV for surface science studies is the cleanliness of the sample surfaces. XPS spectra confirmed that the primary contaminant was C-species. The thin SiO_2-films are very delicate, so the normal cleaning procedures applied to metal surfaces in UHV like Ar sputtering followed by heating in O_2 and/or H_2 were not successful. We found that the energy of the Ar ions should be very low not to damage the oxide, exposure to 500 eV Ar ions left the IV-characteristics of the device unaltered, whereas only 1 min exposure to 1 keV ions increased the diode current by one order of magnitude and further exposure led to a soft breakdown. The method of ion implantation in the Si technology for obtaining various doping profiles also suffers from these unwanted effects, and the common solution to this is annealing to high temperatures [28]. The sputter efficiency was very low at these energies, so this method was abandoned. The sample holder only allowed heating to around 650 K, and at this temperature neither O_2 nor H_2 had any impact on the C overlayer, probably because Au is too noble. However, the nobleness of Au makes it possible to clean the samples in an oxidizing agent immediately before insertion into UHV. Testing the RCA I (H_2O:H_2O_2 30%:NH_4OH 29% in the relation 5:1:1), RCA II (H_2O:H_2O_2 30%:HCl 37% in the relation 5:1:1) and pirañha (H_2SO_4 98%:H_2O_2 30% in the relation 3:1) solutions [29] at room temperature showed good results with RCA I, followed by rinsing in water. The next step was to employ activated O_2 molecules to clean the surface in situ, and this was achieved by sputtering at 500 V in O_2. This energy was chosen on the background of the results from Ar sputtering, and the oxygen ions proved very efficient in removing the surface C without affecting the electrical characteristics of the devices. By ISS we could verify that this treatment leaves only a small fraction of a monolayer of carbon on the surface and negligible amounts of oxygen, see Fig. 3, black line. Though ISS proved that the Au-surface was clean, we were not able to eliminate the C 1s peak in the XPS spectrum, most likely due to C incorporated in the film, so we could not quantify the C-coverage by XPS. XPS spectra did confirm, that the Au surface was not oxidized by the oxygen ions, which contradicts the results presented in [30,31], both groups saw oxidized Au after exposure to 500 eV [30] and 1–5 keV [31] oxygen ions. We explain this by the fact, that the

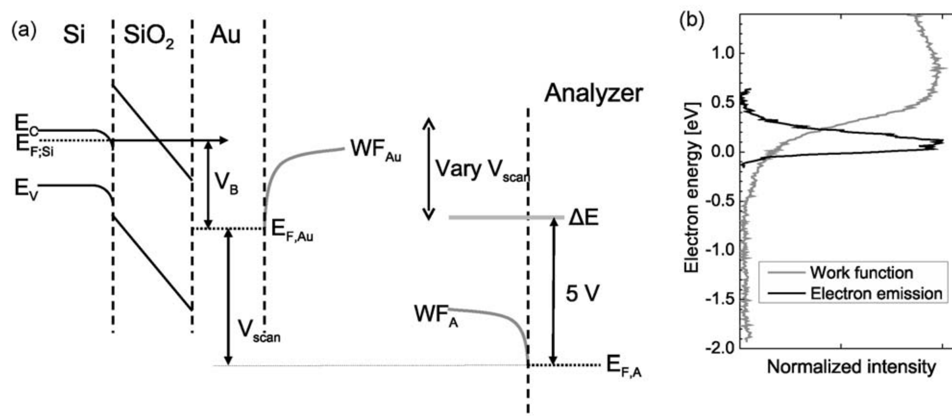

Fig. 2. (a) Energy diagram depicting the energy levels of the sample and the analyzer when obtaining electron emission spectra. E_F, E_C and E_V designate the Fermi level, the conduction band and the valence band, respectively. The sample is biased by V_B, and when this is high enough, electrons tunneling through the oxide have sufficient energy to escape the work function, *WF*, of the Au surface. The analyzer is set up to measure electrons of 5 eV kinetic energy at a pass energy of 1 eV, so it has a window open of width ΔE (approximately 1% of 1 eV = 10 meV), 5 eV above the analyzer Fermi level. The sample floats at a voltage V_{scan} relative to the analyzer, and by scanning this voltage, an energy spectrum of the emitted electrons from the sample can be completed. (b) A work function measurement of the clean Au-film (grey) is shown along with the emission spectrum at 4.7 V device bias (black). The energy scale is relative to the work function of the clean Au surface.

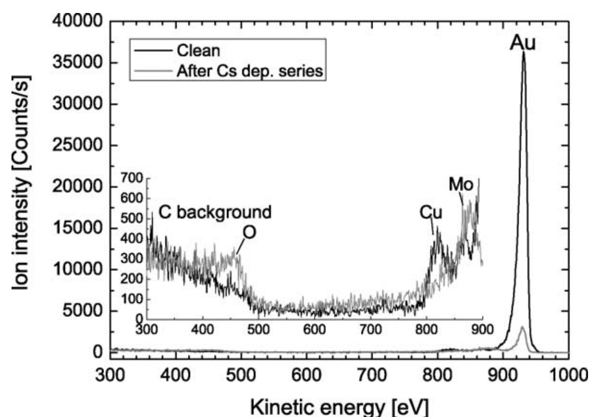

Fig. 3. ISS spectra demonstrating the cleanliness of the sample, the inset shows a magnification of the region from 300 eV to 850 eV. Black: after oxygen ion treatment and prior to Cs deposition. The sample has a small C contamination and no oxygen. Grey: after a series of Cs depositions, total duration of the measurements around 6 h. Oxidation of the Cs overlayer is seen to be almost negligible in XPS spectra of the O 1s line recorded after each Cs dose.

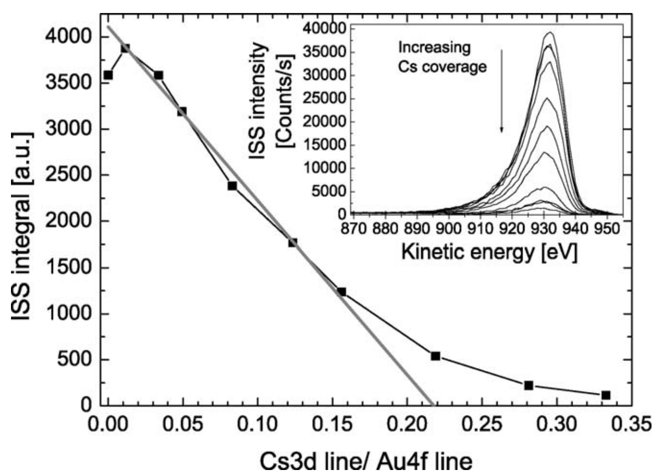

Fig. 4. The decrease in the integral of the Au-peak in the ISS spectra with increasing Cs coverage. The Cs coverage is quantified by XPS as the integral of the Cs $3d_{5/2}$ line divided by the integral of the Au 4f lines, assuming negligible attenuation of the Au signal at these low Cs coverages. The plot shows a linear relationship at low coverage. The inset shows the ISS spectra of the Au line as it drops in intensity with increasing Cs coverage.

oxygen ions will preferentially react with the surface C, and since our goal was to clean the surface, we stopped when this was achieved, so we exposed the Au surface to much smaller doses (a factor of $\sim$100 times smaller as compared to [31]).

3. Results and discussion

3.1. ISS on Cs/Au-film

The surfaces of the Au top-electrodes were investigated with XPS and ISS, both prior to and in between Cs-depositions. Since ISS probes only the topmost atom-layer of a surface it is a more powerful tool when checking the cleanliness of the sample and also in determining coverages of adsorbed species. Fig. 3 compares the full ISS-spectrum of the freshly cleaned sample (black line), with the spectrum after a finished Cs-deposition series (grey line). In the range from 300 eV to 850 eV the spectra have been magnified in the inset. Some signal from the sample holder and the mounting clips (Cu and Mo) is obtained since the ion beam was defocused to cover the whole sample, in order to avoid uneven sputtering of Cs.

The probability for He ions to survive the collision with surface atoms depends strongly on various factors, like geometry, the element of the target atom and shadowing effects from adsorbates [32]. Also the work function of the surface is rather important, since it determines the possible neutralization mechanisms the ions are subject to. Lowering of the work function to a certain level makes resonant neutralization possible, in addition to Auger and collision-induced neutralization [32,33]. Exactly how the survival probability of the scattering ions depends on the work function seems to vary strongly with scattering geometry and primary ion energy [34,35], but in general the survival probability decreases with work function, so that alkali metals give only very small signals in ISS [32–36]. We were not able to detect any signal from the deposited Cs-atoms, so our approach to determining the absolute Cs-coverage was from attenuation of the Au signal.

Also the exposure to 1 keV He ions during ISS proved to be detrimental to the oxide. The device current has increased after 1 keV He ion exposure and a soft breakdown occurs after exposure times comparable to those for 1 keV Ar ion exposure, so this method could not be applied on samples which were to be used for electron emission. Therefore the correlation between the relative XPS line intensity of the Cs 3d-line and the ISS attenuation was determined. Fig. 4 shows this relation as the integral of the ISS Au-peak versus the integral of the Cs $3d_{5/2}$ line normalized with the integral of the Au 4f lines, assuming the attenuation of the XPS Au-signal due to Cs deposition to be negligible. The integrals are calculated from the raw data after background subtraction (Cs-line: linear background, Au-lines and ISS Au-peak: Shirley background, as implemented in the CasaXPS software). There is a linear relationship at sub-monolayer coverages which flattens out at higher coverages. It should be noted, that the relationship between the relative XPS Cs-line intensity and the deposition time is linear, so the quantification by XPS is a direct measure of the coverage. The grey line in Fig. 4 represents a linear fit to the points 2–7. The first point from the clean Au surface is omitted, as it shows an unexplainable low intensity, and we judge the next six points to represent the linear decrease in ISS intensity. The linear fit intersects the abscissa at 0.22 which is the relative Cs $3d_{5/2}$-line intensity corresponding to one monolayer. The exposure to the He ion beam leads to some sputtering, so the XPS spectra as well as the work function were recorded both before and after each ISS spectrum and the average was used. The difference is considerable, $\sim$20%, at low coverages but drops to a few percent at high coverages.

For each data point in Fig. 4 the XPS O 1s line was recorded, and we could not detect any oxidation in this manner. The behavior with an apparent small increase in ISS signal for the smallest Cs dose could not always be reproduced, and we do not have information enough to speculate about its origin.

3.2. Work function of cesiated Au-film

The position of the energy cut-off of the secondary electrons escaping the Au-surface represents the work function, an example of a work function curve can be seen in Fig. 2 b, grey line. The work function is determined by making a linear fit to the steep part of the curve and calculating the intersection with the energy axis. This method has proven very robust, it is not very sensitive to the number of data points included in the fit, and it yields the same results as determining the inflection point of the curve from the first order derivative, since we are only interested in work function changes. Here it is practical to use the work function of the cleaned Au-surface as the reference.

In Fig. 5 the change in work function is plotted versus the Cs-coverage as quantified by XPS. The behavior of the curve resembles

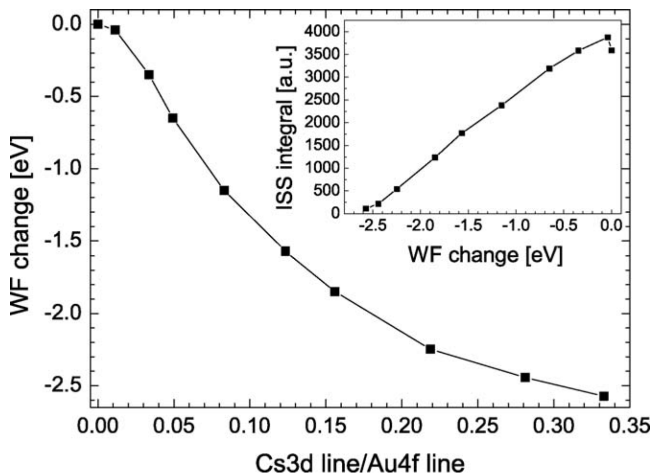

Fig. 5. The decrease in work function with increasing Cs coverage quantified by XPS. The work function is seen to decrease linearly with Cs coverage in the regime at low coverages. The inset shows the integral of the Au peak in the ISS spectra vs. the change in work function. There is an apparent linear relationship, see Section 3 in the text. At the relative Cs XPS line intensity of 0.22 which we interpret as one monolayer, the work function is seen to level out.

that of the ISS intensity as can also be seen in the inset showing the ISS intensity versus the work function change. Studies of work function change with alkali metal coverage on single crystals show a minimum at a distinct coverage, dependent on the alkali metal studied [37,38], the explanation being a maximal polarization of the adsorbates by donation of negative charge to the substrate. This occurs for a certain overlayer structure and is an indication of long range order in the alkali metal layer. We do not see this minimum occur in any of our measurement series, which have also been extended to higher coverages than the one shown here, but this is expected, since the Au-films are poly-crystalline, and the apparent work function will probably be an average of different facets.

Our measurements show an apparent linear dependence of the attenuation of the ISS Au signal with work function. It has been shown in the literature, that the dominating neutralization mechanisms at high work functions (Auger and collision induced) are independent on work function, whereas the resonant neutralization probability depends on the macroscopic or average work function [33,36]. Cortenraad et al. [33], however, see a continuous decrease in ISS signal from the substrate, and only a work function dependent signal from the Ba add-atoms for the same scattering geometry as in the present study. So the fact, that we determine the Cs coverage from the attenuation of the Au signal data points at low coverage adds credibility to the result, that 1 ML of Cs corresponds to a relative Cs XPS line intensity of 0.22.

3.3. Electron emission

Having established the characteristics of the Au and cesiated Au-surfaces in terms of cleanliness, work function and Cs-coverage, more detailed studies of the electron emission could be performed. In order to investigate the correlation between the state of the electrode surface and the emission characteristics of the devices, energy spectra of the emitted electrons along with measurements of the work function for four different surfaces are obtained.

As discussed in Section 2.2, Fig. 2 a explains the principle of the electron emission measurements. Fig. 2 b shows the work function of the clean Au-surface (grey) along with the emission spectrum at a device bias of 4.7 V (black). In these measurements the work function curves are obtained with the same sample/analyzer set up as for the emission measurements, only with the front and back electrodes shorted, and photoelectron excitation by X-rays. Zero on the energy axis is the measured work function of the clean Au-surface, determined from the work function curve as explained above. The work function curve is seen to be rather broad, which we explain by the presence of different Au sites on the surface of the poly-crystalline Au-film. The work function of different facets can from theoretical calculations vary up to 0.75 eV and experimental values are around 5.40 eV [39]. The position of the 4.7 V emission peak relative to the work function curve indicates, that electrons are being emitted from the surface at low-work function sites.

Fig. 6 shows the emitted electron distributions and the work function curves from (A) a clean Au surface (the same measurement as in Fig. 2b), (B) the Au surface with a Cs coverage of ~ 0.87 ML, (C) the Au surface with a Cs coverage of ~ 1.74 ML, and (D) the cesiated Au surface after being left for 80 min under UHV conditions. For each emission spectrum the device bias voltage that gives the onset of emission is chosen. The decrease in work function with increasing coverage can be followed and the work function curves get markedly sharper, which could be because the Cs-overlayer makes the overall work function much more homogeneous or because certain low-work function sites dominate the emission. The electron emission spectra confirm that as the work function is lowered, hot electrons can be emitted at lower device bias voltage. The position of the peak corresponds very well

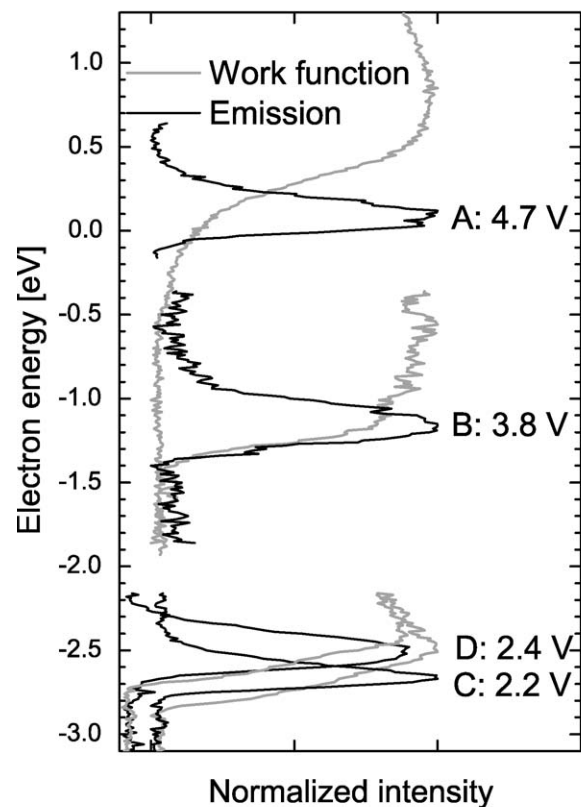

Fig. 6. Electron emission energy spectra (black) and work function measurements (grey) recorded for four different states of the surface. A: Clean Au-surface (the same measurement as in Fig. 2(b)) at a device bias voltage of 4.7 V. B: ~ 0.87 ML Cs/Au surface, device bias voltage 3.6 V. C: ~ 1.74 ML Cs/Au surface, device bias voltage 2.2 V. D: Previous surface after 80 min in UHV, device bias voltage 2.4 V. This curve is shifted to the left for clarity. It is observed how the bias voltage for which tunnel electrons begin to escape the surface is lowered along with the lowering of the work function.

to the applied bias, and for the cesiated surfaces the low-energy cut-off in electron intensity follows the work function very nicely. Consequently, much higher emission currents can be achieved by lowering the work function as reported in [17], where integrated emission current vs. device bias voltage curves from similar devices are presented. By cesiation of the surface, an emission efficiency of 4.3% at 4 V device bias voltage can be achieved. For the same device without Cs the emission efficiency at 5 V device voltage is $\sim 10^{-4}$. It is not possible to apply as high bias voltages on the cesiated devices compared to the clean devices, since Cs reduces their reliability. As discussed in [17], Cs migrates through the Au and into the SiO_2–Ti–Au-interface and possibly further into the SiO_2, compromising the stability of the oxide under bias voltage. It further changes the IV-characteristics of the devices by changing the work function, probably both at the metal-vacuum and the metal-oxide interfaces. For technical applications, therefore, other work function lowering agents or top-electrode metals should be investigated.

Leaving the cesiated Au surface in vacuum for 80 min increases the work function slightly. This was also seen by LaRue et al. [40] and they speculate, that this can either be due to reaction with the background pressure of for instance O_2 or water, or desorption of Cs.

4. Conclusion

The MOS devices work as electron emitters when applying a bias across the oxide, which is high enough for the electrons to overcome the work function of the top-electrode. Deposition of Cs effectively lowers the work function of the Au top-electrode up to 1 ML of Cs, without the appearance of a minimum, most likely because the Au-film is poly-crystalline. Kinetic energy spectra of the emitted electrons at the onset of emission for different Cs coverages confirm that the low energy cut-off of the electron emission is determined by the work function. This implies, that changing the device bias voltage by the same amount as the work function yields qualitatively identical emission spectra.

We have further developed a procedure for cleaning MOS electron emitters with Au top-electrodes produced on Si-wafers in a cleanroom, involving cleansing in an oxidizing agent before insertion in UHV, followed by in situ cleaning with 500 eV O-ions produced in a normal ion gun, which makes the devices suitable for surface science studies. This low ion energy does not affect the functionality of the devices whereas exposure to 1 keV Ar ions which is often applied for sputter cleaning, as well as exposure to 1 keV He ions during ISS leads to a soft breakdown in the devices, meaning that the device current gradually increases with ion exposure, so that a certain ion dose results in a total breakdown. The threshold energy for ions being able to damage the oxide after passage of the 7 nm Au top-electrode lies between 0.5 and 1 keV.

Acknowledgment

The work presented has been founded by the Danish National Research Foundation as part of their grant for the Center for Individual Nanoparticle Functionality.

References

[1] N.S. Xu, S.E. Huq, Mater. Sci. Eng. R 48 (2005) 47.
[2] C.A. Mead, J. Appl. Phys. 32 (1961) 646.
[3] J. Cohen, J. Appl. Phys. 33 (1962) 1999.
[4] J. Cohen, Appl. Phys. Lett. 1 (1962) 61.
[5] J.-S. Kim, T. Hoshi, K. Sawada, M. Ishida, J. Vac. Sci. Technol. B 22 (2005) 1358.
[6] M. Mańkoš, R.M. Tromp, M.C. Reuter, E. Cartier, Phys. Rev. Lett. 76 (1996) 3200.
[7] H. Mimura, Y. Neo, H. Shimawaki, T. Matsumoto, K. Yokoo, Appl. Surf. Sci. 244 (2005) 498.
[8] K. Yokoo, H. Tanaka, S. Sato, J. Murota, S. Ono, J. Vac. Sci. Technol. B 11 (1992) 429.
[9] J. Ikeda, A. Yamada, K. Okamoto, Y. Abe, K. Tahara, H. Mimura, K. Yokoo, J. Vac. Sci. Technol. B 16 (1998) 818.
[10] H. Adachi, J. Vac. Sci. Technol. B 14 (1996) 2093.
[11] K. Sakemura, N. Negishi, T. Yamada, H. Satoh, A. Watanabe, T. Yoshikawa, K. Ogasawara, N. Koshida, J. Vac. Sci. Technol. B 22 (2004) 1367.
[12] K. Yokoo, S. Sato, G. Koshita, I. Amano, J. Murota, S. Ono, J. Vac. Sci. Technol. B 12 (1993) 801.
[13] A. Govyadinov, T. Novet, D. Pidwerbecki, S. Ramamoorthi, J. Smith, J. Chen, C. Otis, D. Neiman, P. Benning, J. Vac. Sci. Tecnol. B 23 (2005) 853.
[14] D.J. DiMaria, M.V. Fischetti, J. Appl. Phys. 64 (1988) 4683.
[15] J. Drucker, P.K. Hansma, Phys. Rev. B 30 (1984) 4348.
[16] H. Mimura, Y. Neo, H. Shimawaki, Y. Abe, K. Tahara, K. Yokoo, Appl. Phys. Lett. 88 (2006) 123514.
[17] L.B. Thomsen, G. Nielsen, S.B. Vendelbo, M. Johansson, O. Hansen, I. Chorkendorff, J. Vac. Sci. Technol. B 27 (2009) 562.
[18] M. Poppeller, E. Cartier, R.M. Tromp, Microelectron. Eng. 46 (1999) 183.
[19] B. van Someren, M.J. van Bruggen, Y. Zhang, C.W. Hagen, P. Kruit, J. Phys.: Conf. Series 34 (2006) 1092.
[20] X. Liu, B. Roldan Cuenya, E.W. McFarland, Sens. Actuat. B Chem. 99 (2004) 556.
[21] B. Roldan Cuenya, H. Nienhaus, E.W. McFarland, Phys. Rev. B 70 (2004) 115322.
[22] B. Mildner, E. Hasselbrink, D. Diesing, Chem. Phys. Lett. 432 (2006) 133.
[23] J.Y. Park, G.A. Somorjai, Chem. Phys. Chem. 7 (2006) 1409.
[24] S. Meyer, D. Diesing, A. Wucher, Nucl. Instrum. Method B 230 (2005) 608.
[25] M.P. Ray, R.E. Lake, S.A. Moody, V. Magadala, C.E. Sosolik, Rev. Sci. Instrum. 79 (2008) 076106.
[26] J.W. Gadzuk, Phys. Rev. Lett. 76 (1996) 4234.
[27] L.B. Thomsen, G. Nielsen, S.B. Vendelbo, M. Johansson, O. Hansen, I. Chorkendorff, Phys. Rev. B 76 (2007) 155315.
[28] J.D. Plummer, M.D. Deal, P.B. Griffin, Silicon VLSI Technology—Fundamentals, Practice and Modeling, Prentice Hall, Upper Saddle River, 2000.
[29] W. Kern, Handbook of Semiconductor Wafer Cleaning Technology—Science, Technology and Applications, Noyes, New York, 1993.
[30] J.J. Pireaux, M. Liehr, P.A. Thiry, J.P. Delrue, R. Caudano, Surf. Sci. 141 (1984) 221.
[31] J.M. Gottfried, N. Elghobashi, S.L.M. Schroeder, K. Christmann, Surf. Sci. 523 (2003) 89.
[32] H.H. Brongersma, M. Draxler, M. de Ridder, P. Bauer, Surf. Sci. Rep. 62 (2007) 63.
[33] R. Cortenraad, A.W. Denier van der Gon, H.H. Brongersma, S.N. Ermolov, V.G. Glebovsky, Phys. Rev. B 65 (2002) 195414.
[34] M. Beckschulte, E. Taglauer, Nucl. Instrum. Method B 78 (1993) 29.
[35] P. Wenter, N. Memmel, Surf. Sci. 513 (2002) L419.
[36] M.J. Ashwin, D.P. Woodruff, Surf. Sci. 244 (1991) 247.
[37] R. Błaszczyszyn, M. Błaszczyszyn, R. Meclewski, Surf. Sci. 51 (1975) 396.
[38] R.W. Verhoef, M. Asscher, Surf. Sci. 391 (1997) 11.
[39] H.L. Skriver, N.M. Rosengaard, Phys. Rev. B 46 (1992) 7157.
[40] J.L. LaRue, J.D. White, N.H. Nahler, Z. Liu, Y. Sun, P.A. Pianetta, D.J. Auerbach, A.M. Wodtke, J. Chem. Phys. 129 (2008) 024709.

Paper B

Electron emission from ultralarge area metal-oxide-semiconductor electron emitters

Lasse B. Thomsen, Gunver Nielsen, Søren B. Vendelbo, and Martin Johansson
Department of Physics, Center for Individual Nanoparticle Functionality (CINF), Technical University of Denmark, DK-2800 Kongens Lyngby, Denmark

Ole Hansen
Department of Physics, Center for Individual Nanoparticle Functionality (CINF), Technical University of Denmark, DK-2800 Kongens Lyngby, Denmark and Department of Micro- and Nanotechnology, Technical University of Denmark, DTU Nanotech, Building 345 East, DK-2800 Kongens Lyngby, Denmark

Ib Chorkendorff[a]
Department of Physics, Center for Individual Nanoparticle Functionality (CINF), Technical University of Denmark, DK-2800 Kongens Lyngby, Denmark

(Received 6 November 2008; accepted 12 January 2009; published 6 March 2009)

Ultralarge metal-oxide-semiconductor (MOS) devices with an active oxide area of 1 cm^2 have been fabricated for use as electron emitters. The MOS structures consist of a Si substrate, a SiO_2 tunnel barrier (~5 nm), a Ti wetting layer (3–10 Å), and a Au top layer (5–60 nm). Electron emission from the Au metal layer to vacuum is realized from these devices by applying bias voltages larger than the work function of the Au layer. The emission is characterized for Au layers with thicknesses ranging from 5 to 60 nm nominally. The emission efficiency changes from close to 10^{-6} to 10^{-10}. The Ti wetting layer is varied from 3 to 10 Å which changes the emission efficiency by more than one order of magnitude. The apparent mean free path of ~5 eV electrons in Au is found to be 52 Å. Deposition of Cs on the Au film increased the electron emission efficiency to 4.3% at 4 V by lowering the work function. Electron emission under high pressures (up to 2 bars) of Ar was observed. © *2009 American Vacuum Society.* [DOI: 10.1116/1.3079649]

I. INTRODUCTION

In many scientific and technological applications electron emitters are necessary.[1] Traditionally free electrons have been generated from hot filaments,[2] where a tungsten wire is heated by a direct current until some of the electrons gain enough energy to escape the work function of the filament. Such filaments have several drawbacks such as their size, extensive heating of surroundings, outgassing,[3] high intensity light emission, and poor control of the direction of the emitted electrons. For many years it has been a goal to develop low cost,[1] preferably silicon-based, cold-cathode electron emitters, which could be integrated on chip.

Today most on-chip cold-cathode electron emitters in application are of the field effect type.[1,4] In such devices the high fields generated at geometrically sharp tips are used to draw out electrons from solid state to vacuum. These emitters can only be operated under vacuum conditions since the devices cannot stand the high fields at the tips under high pressure due to formation of discharges between the anode and the tip.

The work presented in this article investigates the electron emission characteristics of a metal-oxide-semiconductor (MOS) electron emitter.[5–9] This type of emitter works by biasing an ultrathin tunnel barrier which is sandwiched between two electrodes, a semiconductor and a metal layer. When the bias voltage across the tunnel barrier is larger than the work function of the metal layer, electrons are emitted to vacuum.[6,10,11] The electrons are scattered in the metal layer,[12,13] so to achieve a high efficiency of electrons emitted to vacuum relative to the electrons transported through the tunnel barrier the metal layer should be kept as thin as possible while still uniform. In practice electron emission can be realized from metal layers a few tens of nanometers thick and below.

The MOS type of cold-cathode electron emitter is free from many of the drawbacks which traditional and field-effect emitters suffer from. MOS electron emitters will theoretically have no outgassing, generate no significant amount of heat, they can be made extremely small, and be operated under a wide range of conditions.[14] As demonstrated in this work the emitters can operate in the range from vacuum up to at least atmospheric pressure. Furthermore these emitters can easily be fabricated in any shape and size to give emission in a given pattern, which is utilized in hot electron emission lithography.[15] Furthermore the turn-on and turn-off rates of the MOS electron emitters are only limited by the resistance capacitance (RC) product of the devices. The weak points of the MOS electron emitter are the low emission current density—here we report up to 36 nA cm^{-2}—and possible breakdown of the insulator tunnel barrier during operation.[16–19] Insulator breakdown will rapidly decrease the emission efficiency and in the end render the device useless.

To increase the emission current of the MOS emitter the devices presented in this work are ultralarge with an active area of 1 cm^2. It is a significant challenge to produce MOS

[a]Electronic mail: ib.chork@fysik.dtu.dk

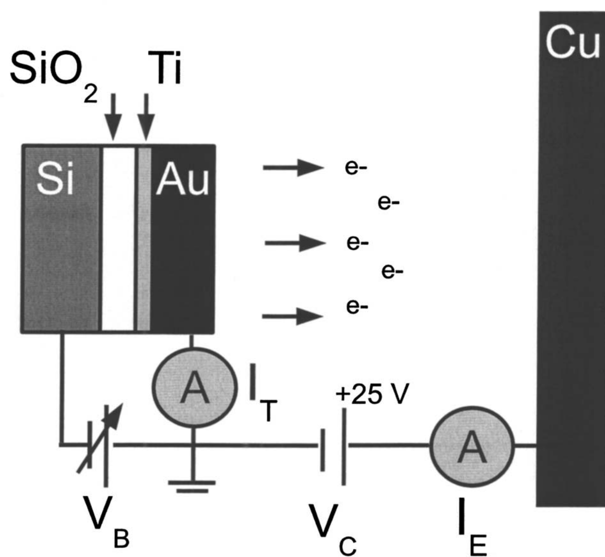

FIG. 1. Schematic of the electron emission setup. On the left hand side the MOS electron emitter is depicted with the Si substrate, thermally grown oxide tunnel barrier, Ti wetting layer, and the Au film on top. Under large forward bias (V_B > 4.6 V) electrons are emitted from the Au surface and are attracted to the Cu collector which is biased positively (V_C=25 V) with respect to the Au surface. The transmission, the current through the layers of the MOS electron emitter, which is not emitted to vacuum (I_T) is measured by an ampere meter, while the current to the Cu collector (I_E) is measured by an electrometer. The distance from the Au surface of the MOS electron emitter to the Cu collector plate is approximately 2 mm.

emitters with an active area of 1 cm^2 since the SiO_2 tunnel barrier must be close to defect free in order to get a reasonable emission efficiency. When scaling up the area of the thin tunnel oxide the number of statistical defects leading to oxide breakdown increases rapidly.[17] Nonetheless, for our application of investigating surface chemistry enhanced by hot electrons,[20–22] an ultralarge area is necessary to be able to detect gas phase or surface adsorbed reaction products on the MOS electron emitters. The MOS electron emitter is implemented with a *n*-type Si wafer as substrate, a thermally grown SiO_2 layer (5 nm) as the tunneling barrier, a thin (3–10 Å) Ti wetting layer, and a Au (5–60 nm) layer as the top electrode.[23]

In this work we report on the electron emission characteristics from our MOS electron emitters to vacuum, and how the emission is influenced by changing the Au and Ti layer thicknesses. Furthermore we have investigated emission under high pressure (2 bars) and the efficiency of a MOS electron emitter with a cesiated Au film.

II. EXPERIMENT

A. Structure and fabrication of MOS electron emitters

The experiments carried out in this work have all been done on the same type of basic device, Fig. 1; a metal oxide semiconductor consisting of a highly Sb doped Si (001) substrate (<25 mΩ cm), on which an ultrathin dry thermal silicon dioxide (SiO_2) layer is grown (∼5 nm). The metal top layer consists of a physical vapor deposition film of a thin (3–10 Å) Ti wetting layer and a Au layer (5–60 nm). The MOS electron emitters presented in this article are fabricated in the clean room facilities at Danchip at the Technical University of Denmark. The fabrication procedure has been described in detail elsewhere.[23] The active area of the electron emitter is 1 cm^2.

B. Measurements of transmission and emission currents

Most of the measurements presented in this work were all carried out in an ultrahigh-vacuum (UHV) chamber with a base pressure below 10^{-9} mbar. The MOS electron emitters were placed in special sample holders in which a bias voltage could be applied across the oxide. A relatively large (3 × 3 cm^2) Cu plate, which could be biased relative to the MOS electron emitter, was installed as an electron collector and a voltage of +25 V was applied relative to the MOS electron emitter surface, see Fig. 1. During measurements of the electron emission the distance between the collector plate and the Au surface of the MOS electron emitter was approximately 2 mm. Varying the distance (±1 mm) did not affect the emission current measured. The UHV chamber was blackened out during all emission measurements, otherwise a photocurrent in the picoampere range was measured to the collector plate.

The current through the oxide layer of the MOS electron emitters, which was not emitted to vacuum (I_T), was measured using a Keithley 6485 picoampere meter. A Keithley 6514 electrometer was connected in series between the voltage supply and the collector to measure the current of electrons to the collector (I_E). The MOS electron emitters were biased using a National Instruments M-series digital acquisition card capable of delivering 20 mA of current to the MOS electron emitter. The bias voltage was measured using the same digital acquisition card. From a measurement across a thick Au film (100 nm) using the probes used for contacting the MOS electron emitters the resistance was measured to below 1 Ω, which makes the parasitic voltage drops across the contacts negligible at the currents measured in this work (<20 mA).

C. Measurements of metal film thickness and integrity

The top metal layers of various thicknesses of Ti and Au were defined using a shadow mask. After deposition the total thickness was measured using a Veeco NanoMan atomic force microscope (AFM). A scan with a side length of 10–60 μm was made across the edge of the metal layer and the NANOSCOPE software was used to process the images. The images were first leveled using a first order plane fit and thereafter the step height was measured using a built-in function of the NANOSCOPE software that compares the average height of two areas, one on each side of the step. For each film thickness one 4 in. wafer was produced and devices from this were labeled with the metal thickness obtained by AFM. For each wafer the thickness of the metal was measured at several locations across the wafer and an average

value of the step height was obtained for the thickness. The integrity of the metal layers was investigated using both AFM roughness measurements and scanning electron microscopy (SEM). The root mean square and absolute mean roughness of the metal films were all approximately 1–3 Å. The SEM micrographs showed no signs of discontinuities and only very few voids with a diameter of approximately 50–100 nm. These voids were only found in Au films with thicknesses below 10 nm. Their presence did not correlate with the thickness of the Ti wetting layer.

The measurements on cesiated devices were done after deposition of Cs using a Cs getter (SAES) mounted in a water cooled housing with a flag. Cs deposition was done by driving a constant current of 7.2 Å through the getter. Before each dose the getter was outgassed for 2 min and the timing of the doses was controlled by turning the flag in front of the getter away and dosing for 20 min. This Cs dose is expected to correspond to a coverage of 1–2 ML (monolayer) since we observe the lowest work function after this dosing time.

D. Measurements of electron emission under high pressures

The measurements of electron emission in high pressures were performed in a minichemical reactor of stainless steel. The mini reactor area was 14×17 mm^2 and the gap between the surface of the MOS electron emitter and the lid of the reactor was 1 mm. The gas pressure was measured using a Brooks 5866 pressure controller. The reactor could be evacuated to high vacuum using a turbomolecular pump. The electron emission was measured using a Keithley 6514 electrometer connected to the lid of the mini reactor. The lid was electrically isolated from the rest of the reactor by a Viton gasket also used as the seal for the reactor. The lid of the minireactor was biased with +25 V with respect to the MOS electron emitter Au film during measurements in order to attract emitted electrons.

III. RESULTS AND DISCUSSION

A. Emission from Ti–Au films

The work presented here is based on simultaneous measurements of the *IV* characteristics of MOS electron emitters and the current emitted to vacuum. The current through the SiO_2 tunnel barrier, which is not emitted to vacuum, is labeled as the transmission (I_T), while the current emitted to vacuum is labeled emission (I_E). Three typical consecutive measurements on the same MOS electron emitter are shown in Fig. 2. The first transmission curve shows a typical Fowler-Nordheim (FN) relation between voltage and current. Earlier work on similar devices[23] showed that the transmission transport mechanism obeys the Fowler-Nordheim relation for tunneling. The FN relationship indicates that electrons with high ballistic energy are injected into the metal layer under forward bias (positive voltage on the metal gate compared to the silicon substrate). Electrons are emitted to vacuum if they reach the metal-vacuum interface with enough energy to overcome the work function of the metal layer. On the emission curve for the first run a sharp turn on is seen at 4.6 V which is the voltage where electrons begin to escape the Au surface and are detected by the positively biased copper collector plate. From the point where the emission takes off, it is growing at a much faster pace than the transmission current, i.e., the emission to transmission ratio or efficiency is increasing for increasing voltage.

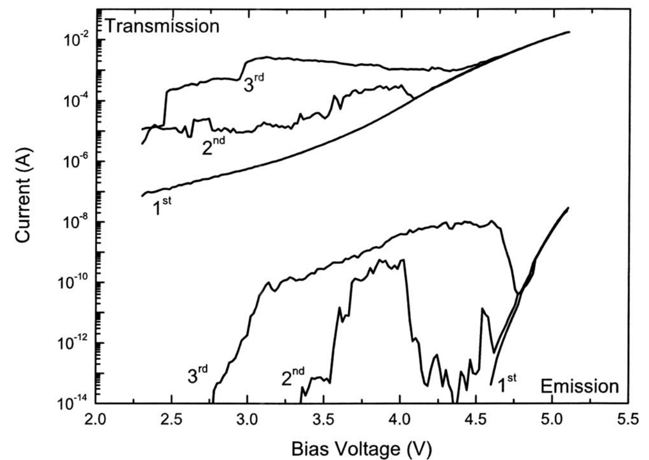

FIG. 2. Transmission through the oxide layer of a MOS electron emitter and the resulting emission to vacuum as measured to a positively (+25 V) biased copper collector plate. In this case the metal film consists of 1 nm Ti and 12 nm Au. It is seen how the emission takes off from 4.6 V in the first run, while in the second run emission is seen from as low as 3.3 V. In the third run emission appears from 2.75 V. In the first run the transmission shows tunneling behavior as the dominating current transport mechanism while significant leakage current is appearing in the second and third run. Although there are fluctuations in the emission and transmission currents in the second and third runs at low voltages, the emission is stable above 4.8 V. The fluctuations in the transmission and emission currents are related to defects in the oxide layer.

In the second and third run the oxide is clearly damaged and substantial leakage current is observed from low pretunneling bias voltages (<3 V), which is a result of the high bias voltage applied in the first run and can be circumvented by limiting the applied bias voltages to lower values. The transmission is still dominated by the FN tunneling at high voltages (>4 V) and the MOS electron emitter still emits electrons. A change in the emission current curve pattern is realized at the voltages just below the turn on of the original emission curve, where electrons are now being emitted at as low as 3 V introducing a shoulder to the original emission curve in the second and third run. At present we have no clear understanding of the origin of these fluctuations, however, they are related to defect creation and progressive breakdown in the oxide layer. Local field enhancement might be responsible for the enhanced emission at low voltages from SiO_2 or Ti due to opening and closing of nanoscale voids in the metal film.

In order to investigate the influence of varying metal layer thicknesses several wafers with MOS electron emitters were fabricated with Au film thicknesses varying from 5 to 60 nm nominally. These Au films were deposited on top of a 1 nm Ti wetting layer to avoid roughness and voids, which is critical since the emission current is expected to be exponentially

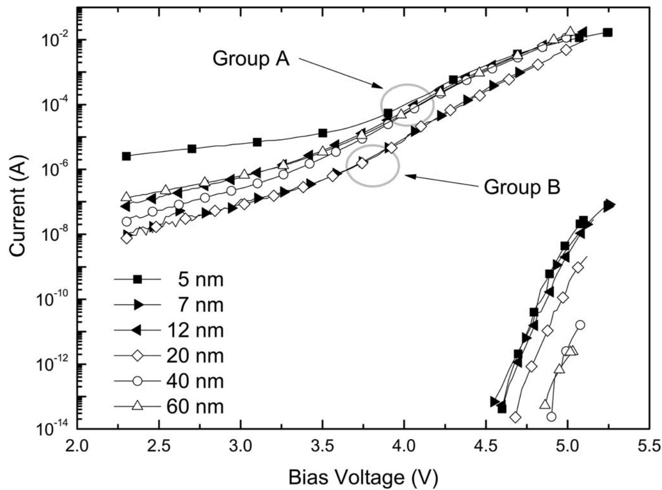

FIG. 3. Transmission and emission curves for several MOS electron emitters with varying Au layer thicknesses. The transmission curves fall in two groups, labeled A and B, which is due to variations in oxide thickness (Ref. 23). The emission current is in general highest for the thinnest metal gate layers, where the emission takes off close to 4.6 V. From the thicker metal gate layers the emission seems to take off at higher voltages, but this is due to the noise floor of the experimental setup.

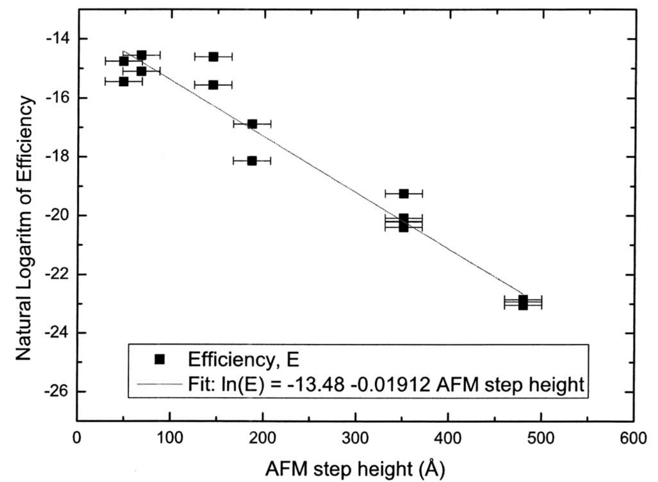

FIG. 4. Natural logarithm of the efficiency of electron emission as a function of the metal thickness measured by AFM. The thickness of the Ti wetting layer is 1 nm for the films used in these measurements. The efficiency is calculated from the emission and transmission current at 5 V from the first run of each device. It is seen that the efficiency is decreasing exponentially with increasing metal thickness.

decreasing with thickness. These wafers were all fabricated in one batch using parallel processing up to the final metal layer deposition step. Figure 3 shows several transmission and emission curves for varying metal layer thicknesses. It is seen how the transmission curves fall in two groups, marked A and B, of curve patterns; one containing the 7 and 20 nm Au film MOS electron emitters and another containing the rest. The reason for the two groups of MOS electron emitters and their different transmission *IV* characteristics is variations in the oxide thickness[23] leading to changes in the transmission probability for electrons to tunnel through the oxide layer. For the emission curves the general trend is that the thinner the metal layer, the higher the emission current, which is due to less scattering of the electrons in the thinner metal layers. There is a higher apparent threshold voltage for the emission current for the thicker metal layer, which is due to the noise of the experimental setup.

B. Electron emission as a function of film thickness

In order to investigate how the electron emission of the MOS electron emitters is affected by varying the metal layer thickness, an emission efficiency is defined as the ratio between electrons emitted to vacuum and electrons transported through the oxide,

$$\eta = \frac{I_E}{I_E + I_T}. \quad (1)$$

From the type of measurement presented in Fig. 2 the efficiency is extracted by reading off the transmission and emission current at a chosen reference voltage and calculating the efficiency by inserting in Eq. (1).

Figure 4 shows efficiencies calculated from several measurements on Ti/Au films with varying Au thicknesses from 5 to 50 nm, but all with 1 nm Ti as wetting layer. The transmission and emission currents at 5 V were used to calculate the efficiencies. It is clearly seen how the emission efficiency decreases in an exponential manner with increasing metal thickness, which is in good agreement with earlier work on electron transmission through thin metal layers.[13,24] From Fig. 4 the mean free path of the emitted electrons in the Au layer can be extracted from

$$\eta(\ell) \propto \exp\left(-\frac{\ell}{\lambda}\right), \quad (2)$$

where ℓ is the thickness of the Au layer and λ is the mean free electron path. $\eta(\ell)$ is the efficiency as defined by Eq. (1) as a function of the Au film thickness. From Fig. 4 the mean free path can be found as the inverse of the slope of the fit to the data, which yields a mean free path of 52 Å for the electrons emitted to vacuum at this energy. This value is a bit higher than the 45 Å given by Kanter[25] at 5.5 eV electron energy. The lower kinetic energy of these measurements results in a longer mean free path of the electrons and the obtained value agrees extremely well with the calculations of Krolikowski and Spicer.[26]

C. Electron emission as a function of Ti wetting layer thickness

In order to investigate the effect of the thickness of the Ti wetting layer, MOS electron emitters with nominal wetting layers of 3, 5, and 10 Å Ti underneath a 7 nm Au film were fabricated. In Fig. 5 the results of varying the Ti layer thickness can be seen. It is seen that the efficiency is, as for the Au films, decreasing with the Ti wetting layer thickness, but here the rate of decrease is 22 times faster if one would fit the data to an exponential decay and extract a mean free path. This would, however, be misleading since existing models predict

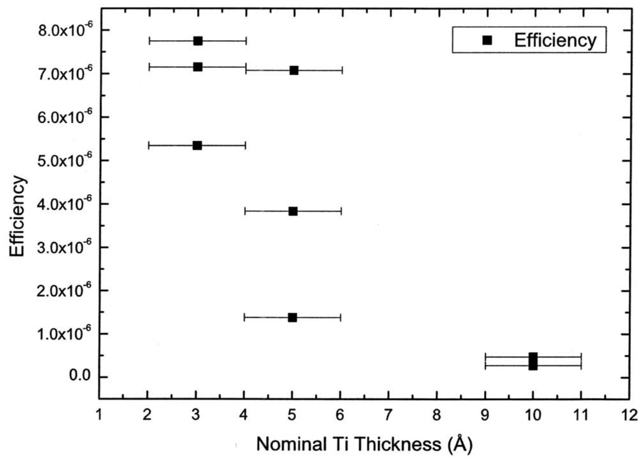

FIG. 5. Logarithm of the efficiency of electron emission as a function of the Ti wetting layer nominal thickness. The thickness of the Au layer is 7 nm. The efficiency is, as for the data in Fig. 4, calculated from emission and transmission current at 5 V from the first run of each device.

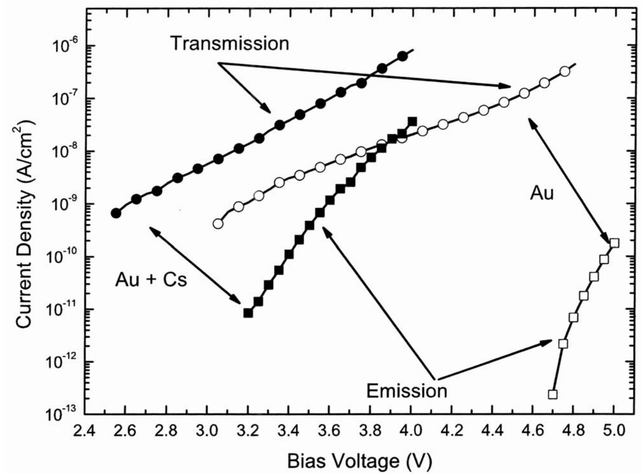

FIG. 6. Electron emission to vacuum from a MOS electron emitter. The open symbols show the *IV* characteristics of the transmission and emission of the as prepared emitter with a 7 nm Au layer while the closed symbols show the same for the emitter after deposition of approximately 1 ML of Cs. The emission threshold is moved considerably from the as prepared Au film to the Cs covered Au film, which indicates a shift of the work function by 1.6 V. The transmission curve of the Cs covered emitter (closed circles) is shifted significantly compared to the as prepared Au emitter (open circles). The emission efficiency of the Cs covered electron emitter is increasing with voltage and is 4.3% at 4 V.

the mean free path of electrons in Au and Ti to be on the same order of magnitude.[26] We believe that the effect of the Ti wetting layer on the ballistic electrons is to introduce an electric potential scattering region. This scattering potential will arise from the difference in work function of Au (5.40 eV) (Ref. 27) and Ti (4.63 eV).[27] The Ti wetting layer has a significant role in the scattering of the ballistic tunnel electrons and must either be kept as thin as possible or perhaps completely circumvented using another metal than Au as the top layer.

D. Emission current from a cesiated Au film

In order to increase the emission efficiency and bring the operation bias voltage down, Cs was deposited on the Au film surface of a MOS electron emitter. This method has proven to work successfully for similar devices.[28–30] The deposition of Cs changed the *IV* curve as well as the work function of the electron emitter significantly, as can be seen in Fig. 6. The threshold bias voltage for electron emission is changed from 4.7 to 3.1 V due to the very low work function [2.1 eV (Ref. 27)] for Cs. The Cs deposition also changes the shape of the *IV* characteristics for the transmission of the electron emitter. This is probably due to alloying effects between Au and Cs in the Au layer[31] and subsequent migration of Cs to the oxide interface. This migration of Cs from the surface of the Au layer to the SiO_2–Ti–Au interface results in changes in the work function at the oxide interface, which in turn changes the tunnel barrier shape and therefore the transmission coefficient of the SiO_2 tunnel barrier. During the experiments Cs proved to reduce the reliability of the oxide, hence Cs is not a feasible work function lowering agent for technological applications. The efficiency of the electron emitter is, despite the higher transmission, increased by two and a half orders of magnitude. The emission efficiency for the Cs covered electron emitter is 4.3% at 4 V, where the emission current reaches 36 nA cm^{-2}. The emission from this specific sample is not particularly high due to a relatively thick oxide layer, as seen in the transmission curve. The emission current can be increased by using thinner SiO_2 tunnel barriers. In this way the emission current could theoretically be increased by several orders of magnitude.

E. Emission current under high gas pressure

A significant advantage of the MOS electron emitter is the ability to operate at high pressures.[14] In Fig. 7 the electron emission from a MOS electron emitter is shown at different pressures of Ar between the collector plate and the surface of the emitter. It is clearly seen that electrons are emitted and collected even at pressures above 1 bar. The ratio of collected electron current under 1 bar of Ar to electron current under vacuum is close to 0.2, which is in very good agreement with the result of Mimura *et al.*[4] They reported an increase in collected electron current of approximately a factor of 5 from decreasing the pressure from 760 torr of air to vacuum. The inset in Fig. 7 shows the pressure dependence of the emission current to the detector plate as a function of pressure, which is very well described as an exponential decay with increasing pressure of Ar, which points toward the mean free path of electrons in the gas to be important. It is our belief that the decrease in collected electron current as a function of pressure is related to backscattering of emitted electrons into the surface of the emitter. The reason for the increase in backscattering probability, as a function of pressure, is the decreasing ratio between the mean free path of electrons in the gas and the electric field between the emitter and collector attracting electrons towards the collector.

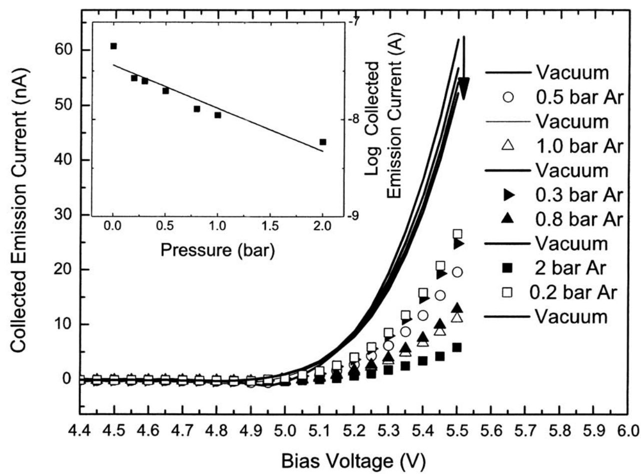

FIG. 7. Electron emission from a MOS electron emitter in Ar pressures from 0.1 to 2 bars. The collected electron emission current is measured under vacuum conditions (<1 mbar) and then under varying pressures of Ar. After each measurement at high pressure, the emission current measurement was repeated under vacuum (solid lines) and the high pressure measurements were performed in the order expressed by the legend. The inset shows the collector current at 5.5 V as a function of Ar pressure.

IV. CONCLUSION

In this work the electron emission from ultralarge area (1 cm^2) MOS electron emitters has been investigated under various conditions and we have arrived at the following conclusions:

- The electron emission efficiency is exponentially reduced when the thickness of the Au layer is increased with an apparent mean free path of 52 Å for 5 eV electrons. This result stresses the necessity of having the thinnest possible metal film in order to preserve as many ballistic electrons as possible yielding a high efficiency.
- Variation of the Ti wetting layer thickness showed that increasing the Ti layer by a few angstroms in thickness results in a decrease in the emission efficiency by an order of magnitude.
- It was shown that it is possible to increase the emission efficiency of the MOS electron emitters by several orders of magnitude using a low work function alkali metal such as Cs. Electron emission efficiencies as high as 4.3% was observed when the Au film was covered with Cs. Still the absolute emission current of 36 nA cm^{-2} is not very competitive and will have to be improved by going to thinner tunnel barriers. Furthermore Cs was seen to alter the tunnel characteristics of the MOS electron emitters and to some extent degrade the reliability of the oxide. It is our opinion that further research on the combinations of other alkali metals with either Au or another top metal could be very fruitful. Perhaps the way to go is to avoid Au altogether and search for a combination of a gate metal layer that does not need a wetting layer to stick to the oxide and is a better diffusion barrier for Cs and other work function lowering agents.
- The results from electron emission under high Ar pressures prove the pressure versatility of the MOS electron emitter, which could be an advantage in many scientific and technological applications.

ACKNOWLEDGMENT

The work presented was founded by the Danish National Research Foundation as part of their grant for the Center for Individual Nanoparticle Functionality.

[1]N. S. Xu and S. E. Huq, Mater. Sci. Eng. R. **48**, 47 (2005).
[2]W. B. Nottingham, Phys. Rev. **49**, 78 (1936).
[3]B. R. F. Kendall, J. Vac. Sci. Technol. A **17**, 2041 (1999).
[4]H. Mimura, Y. Neo, H. Shimawaki, T. Matsumoto, and K. Yokoo, Appl. Surf. Sci. **144**, 498 (2005).
[5]C. A. Mead, J. Appl. Phys. **32**, 646 (1961).
[6]J. Cohen, J. Appl. Phys. **33**, 1999 (1962).
[7]J. Cohen, Appl. Phys. Lett. **1**, 61 (1962).
[8]T. Sumiya, H. Fujinuma, T. Miura, and S. Tanaka, Appl. Surf. Sci. **130–132**, 36 (1998).
[9]K. H.-J. Fitting, T. Hingst, and E. Schreiber, J. Phys. D: Appl. Phys. **32**, 1963 (1999).
[10]D. J. DiMaria, M. V. Fischetti, J. Batey, L. Dori, E. Tierney, and J. Stasiak, Phys. Rev. Lett. **57**, 3213 (1986).
[11]S. D. Brorson, D. J. DiMaria, M. V. Fischetti, F. L. Pesavento, P. M. Solomon, and D. W. Wong, J. Appl. Phys. **58**, 1302 (1985).
[12]J. J. Quinn, Phys. Rev. **126**, 1453 (1962).
[13]C. I. Crowell, W. G. Spitzer, L. E. Howarthan, and D. E. E. LaBate, Phys. Rev. **127**, 2006 (1962).
[14]K. Yokoo, H. Tanaka, S. Sato, J. Murota, and S. Ono, J. Vac. Sci. Technol. B **11**, 429 (1993).
[15]M. Poppeller, E. Cartier, and R. M. Tromp, Microelectron. Eng. **46**, 183 (1999).
[16]S. Lombardo, J. H. Stathis, B. P. Linder, K. L. Pey, F. Palumbo, and C. H. Tung, J. Appl. Phys. **98**, 121301 (2005).
[17]E. Y. Wu and J. Sune, Microelectron. Reliab. **45**, 1809 (2005).
[18]B. P. Linder and J. H. Stathis, Microelectron. Eng. **72**, 24 (2004).
[19]J. F. Verweij and J. H. Klootwijk, Microelectron. J. **27**, 611 (1996).
[20]J. W. Gadzuk, Surf. Sci. **342**, 345 (1995).
[21]J. W. Gadzuk, Phys. Rev. B **44**, 13466 (1991).
[22]J. W. Gadzuk and C. W. Clark, J. Chem. Phys. **91**, 3174 (1989).
[23]L. B. Thomsen, G. Nielsen, S. B. Vendelbo, M. Johansson, O. Hansen, and I. Chorkendorff, Phys. Rev. B **76**, 1 (2007).
[24]H.-J. Drouhin, G. Lampel, Y. Lassailly, A. J. van der Sluijs, and C. Marlihe, J. Magn. Magn. Mater. **151**, 417 (1995).
[25]H. Kanter, Phys. Rev. B **1**, 522 (1970).
[26]W. F. Krolikowski and W. E. Spicer, Phys. Rev. B **1**, 478 (1970).
[27]H. L. Skriver and N. M. Rosengaard, Phys. Rev. B **46**, 7157 (1992).
[28]H. Mimura, Y. Neo, H. Shimawaki, Y. Abe, K. Tahara, and K. Yokoo, Appl. Phys. Lett. **88**, 123514 (2006).
[29]J. Drucker and P. K. Hansma, Phys. Rev. B **30**, 4348 (1984).
[30]H. Mimura, K. Miyajima, and K. Yokoo, J. Vac. Sci. Technol. B **21**, 1612 (2003).
[31]J. A. Rodriguez, J. Hrbek, Y.-W. Yang, M. Kuhn, and T. K. Sham, Surf. Sci. **293**, 260 (1993).

Paper C

Ultralarge area MOS tunnel devices for electron emission

Lasse B. Thomsen,[1] Gunver Nielsen,[1] Søren B. Vendelbo,[1] Martin Johansson,[1] Ole Hansen,[1,2] and Ib Chorkendorff[1,*]
[1]*CINF—Center for Individual Nanoparticle Functionality, Department of Physics, Nano•DTU, Technical University of Denmark, DK-2800 Kongens Lyngby, Denmark*
[2]*MIC—Department of Micro and Nanotechnology, Oersteds Plads Building 345E, Nano•DTU, Technical University of Denmark, DK-2800 Kongens Lyngby, Denmark*

(Received 16 May 2007; revised manuscript received 23 August 2007; published 23 October 2007)

A comparative analysis of metal-oxide-semiconductor (MOS) capacitors by capacitance-voltage (*C-V*) and current-voltage (*I-V*) characteristics has been employed to characterize the thickness variations of the oxide on different length scales. Ultralarge area (1 cm^2) ultrathin (~5 nm oxide) MOS capacitors have been fabricated to investigate their functionality and the variations in oxide thickness, with the use as future electron emission devices as the goal. *I-V* characteristics show very low leakage current and excellent agreement to the Fowler-Nordheim expression for the current density. Oxide thicknesses have been extracted by fitting a model based on Fermi-Dirac statistics to the *C-V* characteristics. By plotting *I-V* characteristics in a Fowler plot, a measure of the thickness of the oxide can be extracted from the tunnel current. These apparent thicknesses show a high degree of correlation to thicknesses extracted from *C-V* characteristics on the same MOS capacitors, but are systematically lower in value. This offset between the thicknesses obtained by *C-V* characteristics and *I-V* characteristics is explained by an inherent variation of the oxide thickness. Comparison of MOS capacitors with different oxide areas ranging from 1 cm^2 to 10 μm^2, using the slope from Fowler-Nordheim plots of the *I-V* characteristics as a measure of the oxide thickness, points toward two length scales of oxide thickness variations being ~1 cm and ~10 μm, respectively.

DOI: 10.1103/PhysRevB.76.155315 PACS number(s): 73.40.Qv, 73.43.Jn, 77.22.Jp, 85.45.Db

I. INTRODUCTION

Solid-state low energy electron emitters have a variety of potential application in science and technology. Several of such potential applications require inexpensive electron emitters.[1] Free electrons can be obtained by heating a filament and extracting electrons with a high voltage extractor. In many applications, the use of such a filament is a problem due to its size, the heat evolved, outgassing,[2] or the light emitted. It has been a goal for decades to be able to substitute these traditional electron sources with inexpensive compact silicon-based cold-cathode emitters.

Most on-chip electron emitters available today are based on the field effect type emitter structure. The field effect emitter has to be operated in vacuum, since it cannot withstand operation at high pressure due to the high fields involved. Another approach to achieve a semiconductor electron emitter is by using a metal-oxide-semiconductor (MOS) structure with an ultrathin oxide acting as a tunnel barrier.[3–5] Oxide film thicknesses on the nanometer scale allow electrons to tunnel from the semiconductor substrate into the top metal film. Applying a voltage larger than the work function of the metal film across such a structure will lead to electrons being emitted into vacuum[3,6,7] if the gate metal film is sufficiently thin. These devices work at low voltages (<10 V), low temperatures, and have a nearly pressure-independent emission.[8] The drawback compared to the field emitter is the low emission current density.

In order to increase the emission current, the area of the thin oxide forming the tunnel barrier must be enlarged. The great challenge of implementing MOS structures as electron emitters lies in the fabrication process, since it is extremely difficult to produce an ultrathin oxide film which is still electrically insulating and nearly defect-free over an ultralarge area, e.g., 1 cm^2. When scaling up the oxide area, the number of statistical defects leading to electric breakdown of the oxide increases dramatically,[9] which leads to a high probability of having a significant fraction of nonfunctional devices. This underlines the necessity of having a means to characterize large area oxides if these devices are to be successfully implemented in electronic devices.

The variation of oxide thickness is of great importance to large area electron emitters for several reasons. One reason is the breakdown of the oxide being of the weakest-link nature.[9] The number of weak points due to spots of thin oxide will scale with the area and, therefore, be more important the larger the oxide area is since breakdown in one of these weak spots is enough to render the whole oxide useless. Another reason is the exponential dependence of the tunneling current on the thickness. The average thickness of the device is, in this way, very important for the absolute brightness of the emission from the device. Furthermore, a variation in thickness will lead to "hot" and "cold" spots in the electron emission being a nuisance in applications where an even distribution of electrons is needed on a certain length scale.

Two possible, unique applications for MOS electron emitters are in electronic catalysis and hot electron emission lithography (HEEL).[10] It has previously been proposed by Gadzuk[11–14] that hot electrons injected from the substrate into the gate in metal-insulator-metal tunnel devices, and thus similar MOS based devices, can be used to enhance surface reactivity on the surface of the ultrathin gate metal. This phenomenon has been investigated experimentally by several groups.[15–19] In HEEL, a MOS electron emitter is used as a combined electron source and mask to illuminate an electron sensitive polymer resist.[10] The patterning is

 ©2007 The American Physical Society

achieved by forming the tunnel oxide or gate metal as a 1:1 mapping of the pattern to be transferred to the substrate. In this way, electron beam lithography can be combined with the massive parallelism known from standard UV lithography.

The MOS capacitor, being one of the most important components in very large scale integration technology as the heart in the field effect transistor (FET), has received a considerable amount of attention in the literature.[20] With regard to FET technology, the thickness variations of the oxide in the MOS structure are important in relation to fluctuations in threshold voltages and electrical breakdown of the oxide, leading to excessive power consumption[21] and possible malfunction. The oxide thickness variations have been characterized on a microscopic length scale by transmission electron microscope,[22] atomic force microscope,[22–24] and scanning tunneling microscope[22,25] measurements. These types of measurements yield valuable information on the micrometer length scale, which is relevant, for example, in FETs, but they do not give the full picture for large area MOS devices, where also longer length scales of variations in the oxide thickness might be important.

Our work is devoted to electronically promoted chemical phenomena, and the devices presented here have been developed to be a platform for delivering hot electrons to a metal surface from within. In this work, we report on the results of the characterization of ultralarge area ($1\ \text{cm}^2$) MOS devices with ultrathin tunnel oxides by *I-V* and *C-V* characteristics. Insights into the oxide thickness variations across these large devices are extracted from a comparative analysis of obtained *C-V* and *I-V* characteristics, and are reported here.

Breakdown statistics[23,26–28] are, besides oxide thickness variations, one of the most important characteristics for ultralarge area MOS electron emitters employed in technological applications, but perhaps not as crucial in our future work of studying electronically promoted chemical phenomena. For this reason, we have not devoted serious attention to this aspect, even though we recognize its extreme importance in other applications.

II. EXPERIMENT

A. Fabrication of ultralarge area ultrathin metal-oxide-semiconductor capacitors

The MOS capacitors presented in this paper are fabricated in the cleanroom facilities at Danchip at the Technical University of Denmark. The wafers used are silicon wafers, fabricated by Okmetic, heavily doped with antimony ($\sim 3 \times 10^{18}\ \text{cm}^{-3}$), resulting in a resistivity of $<0.025\ \Omega\,\text{cm}$. A thick oxide of 750 nm is grown by wet thermal oxidation at 1000 °C to serve as an underlayer for a contact pad for electrical measurement purposes. A wet-etch mask is formed by standard photolithography, and the thick oxide is etched back to the substrate in a standard buffered hydrofluoric acid solution to form the areas for the ultrathin tunnel oxide (SiO_2). The wafers are etched for 9 min continuously, and then inspected for a hydrophobic surface. If this has not been achieved, the wafers are etched in steps of 30 s until a hydrophobic Si surface is observed. It is critical to avoid overetching due to the risk of increasing the surface roughness.[29]

The resist is stripped and a standard RCA cleaning procedure[30] is performed. An ultrathin SiO_2 tunnel barrier is grown thermally in a dedicated ultraclean three-zone drive-in furnace at 800 °C in 1 atm of O_2 for 40 min, with a flow of 6 SLM (SLM denotes standard liters per minute). The oxide growth is followed by a 20 min anneal in 1 atm N_2 at 800 °C, with a flow of 6 SLM. Ti/Au (10/100 nm) gate electrodes are deposited using electron-beam physical vapor deposition (PVD), where Ti serves as a wetting layer. Finally, the native oxide is stripped from the backside of the wafer using a 5% HF solution, and a Ti/Au (10/100 nm) backside electrode is deposited using electron-beam PVD.

B. Measurements of the capacitance and current

Due to the large capacitance ($\sim 0.6\ \mu\text{F}$) in combination with a high tunneling current of the fabricated MOS capacitors, a special technique for measuring the capacitance-voltage (*C-V*) characteristics is adopted. The technique is designed to measure large capacitances and correct for current from parallel conductance due to tunneling. The capacitance is measured by the use of a switched analog integrator (Fig. 1).

The capacitance of a MOS capacitor can be obtained by applying a signal of the form shown in Fig. 2. For each voltage step in the *C-V* characteristics, a square voltage signal is applied to the MOS capacitor. The reason for using a square signal instead of a simple step is to be able to correct for the current signal due to tunneling electrons.

The voltage versus time signal on the integrator increases or decreases in steps when the MOS capacitor is charged or discharged as a consequence of the applied square voltage signal. In between each charging or discharging step, the integrator signal changes at a constant rate due to the current passing through the MOS capacitor (tunneling or leakage current). The voltages V_0, V_1, V_2, and V_4 are measured since there is no decaying charging or discharging current at these points which would otherwise influence the measurement. The signal from a constant current and charging or discharging of the MOS capacitor can be separated using the following procedure: V_0 is used as the reference zero, and V_1 is subtracted from V_4 to obtain V_3. The signal due to the capacitance of the MOS capacitor, V_C, is $V_2 - V_3$. From this voltage difference, the MOS capacitance is calculated as

$$C_{\text{MOS}} = \frac{(V_2 - V_3)C_{\text{ref}}}{\Delta V}, \tag{1}$$

where C_{ref} is the capacitance of the reference capacitor in the integrator and ΔV is the height of the square voltage signal. The current through the oxide of the MOS capacitor and any other leakage currents in the system during Δt are proportional to $V_T = V_3 - V_1$:

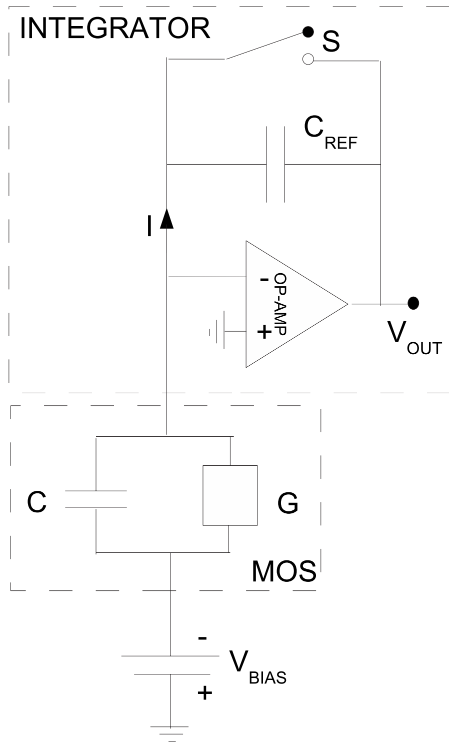

FIG. 1. Diagram of the analog integrator used to measure the *C-V* characteristics presented in this paper. The MOS capacitor under test is modeled as a capacitance C in parallel with a conductance G. The operational amplifier stores the charge flowing to and from the MOS capacitor on the reference capacitor C_{ref}. The switch S is used to reset the integrator before each measurement point. V_{bias} is the bias voltage applied to the MOS capacitor and V_{out} is the readout voltage of the integrator used to calculate the capacitance and current.

$$I_{\mathrm{MOS}} = \frac{(V_3 - V_1)C_{\mathrm{ref}}}{\Delta t}, \qquad (2)$$

where Δt is the duration of the applied voltage pulse. In practice, the current is determined by integration of the current for a period of between 100 μs and 1 s at a constant voltage for better accuracy. Here, the current can be made up of any physical or electronic phenomena in the system such as oxide tunnel current, oxide leakage current, noise induced current, and amplifier bias current.

C. Instrumentation

The bias voltage was generated using a National Instruments PCIe-6259 DAQ card, where the current output was enhanced with a TI BUF634T high speed buffer enabling a maximum current of 250 mA continuously. The MOS capacitors were contacted using Accuprobe *Z*-adjustable probes with gold plated Be and/or Cu tips. The voltage output was measured at the output pin of the TI BUF634T to account for offset and nonunity gain.

The instrument has seven reference capacitors, each covering one decade (4.7 pF–47 μF), switched using standard reed relays. This combined with the variation of the integration time results in a theoretical dynamic range of 14 decades. In practice, this is limited to 11 decades due to the current limitation of the output amplifier (250 mA) and the noise level of the instrument (picoamperes).

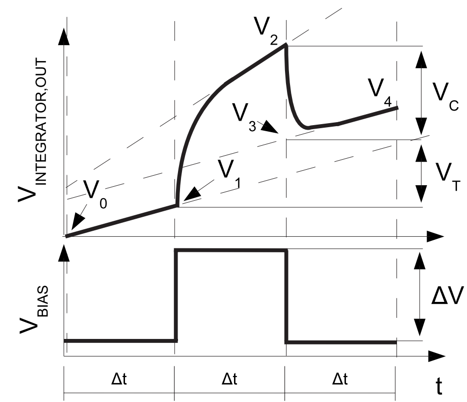

FIG. 2. A sketch of the applied square voltage signal which makes the MOS capacitor charge and discharge, and above, the resulting signal on the integrator. The MOS capacitor is equivalent to a capacitor in parallel with a conductor. The signal on the integrator can be divided into two parts: fast decaying charging and/or discharging signals from the capacitance, and constant increasing signals due to the current flowing through the MOS capacitor. By measuring the voltages V_0, V_1, V_2, and V_4, the current and capacitance of the MOS capacitor can be obtained as explained in the text.

I-V characteristics were also measured using a Keithley 485 ampere meter with a dynamical range from 0.1 pA to 2 mA.

D. Extraction of the oxide thickness

From the *C-V* characteristics, the oxide capacitance is extracted from the total capacitance of the MOS capacitor by fitting it to the exact solution to Poisson's equation for the system using Fermi-Dirac statistics for the electrons in the semiconductor. It is important to use Fermi-Dirac statistics for this system due to the high dopant concentration in the silicon wafers used and due to the very high surface field. Using Boltzmann instead of Fermi-Dirac statistics typically returned 1 Å higher values for the thickness of the oxides. Since the *C-V* characteristics are obtained at high frequency, interface traps are neglected in the extraction of the oxide thickness. The model assumes spatially constant dopant impurity concentration, and interface traps and minority carrier capacitances are neglected. This model, known as the McNutt-Sah-Walstra algorithm, has earlier been used as the benchmark for five other *C-V* oxide thickness extraction algorithms by Walstra and Sah.[31] In addition to fitting the thickness, we also allow for a variation in the dopant concentration to circumvent any misleading changes in the oxide thickness from variations in dopant concentration, which could give rise to changes in the semiconductor capacitance in series with the oxide capacitance.

The oxide thickness is calculated from the oxide capacitance as[32]

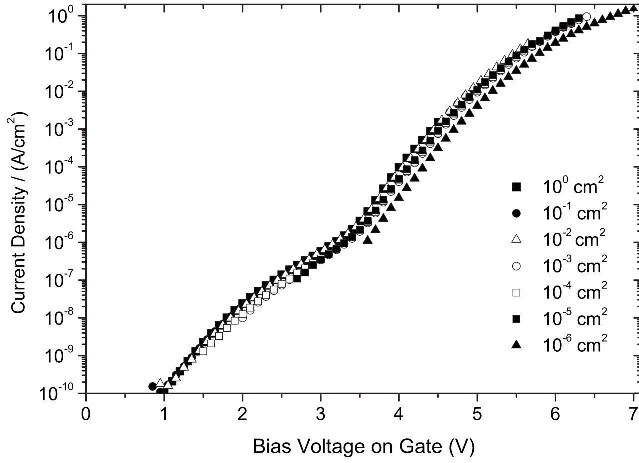

FIG. 3. The current density as a function of gate voltage for seven MOS devices, with oxide areas ranging from 10^{-6} to 1 cm^2. The reason for the different voltage range of measurements on different area devices is the dynamical range of the ammeter.

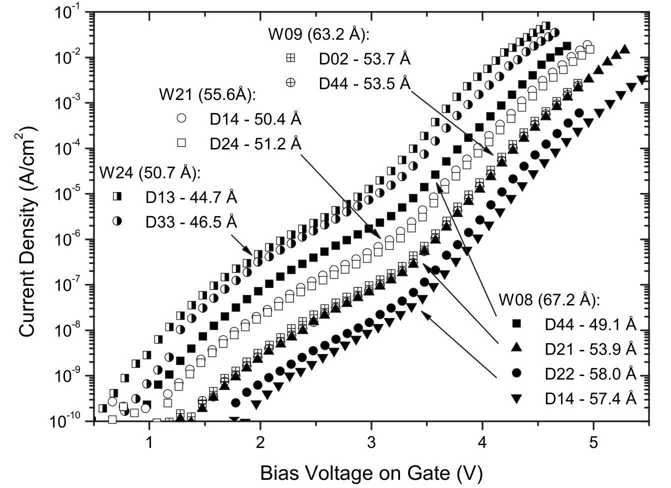

FIG. 4. Measured *I-V* characteristics of ten devices from four wafers, all with an oxide area of 1 cm^2. The oxide thickness measured by ellipsommetry measured on each wafer is shown in parentheses. There is a spread in the oxide thickness between devices, but the thickness extracted from *C-V* measurements agrees qualitatively well with the relative positions of the *I-V* characteristics and the thickness implied therefrom.

$$X_{\text{ox}} = \frac{\epsilon_0 \epsilon_{\text{ox}} A}{C_{\text{ox}}}, \tag{3}$$

where ϵ_0 is the permittivity of vacuum, ϵ_{ox} is the relative dielectric constant of the oxide (SiO_2:3.9), A is the MOS capacitor area, and X_{ox} is the oxide thickness.

III. RESULTS

The results presented here are measured on MOS capacitors on wafers from a single batch. This means that when parallel processing was possible, all wafers were processed in the same run. The MOS capacitors are enumerated according to host wafer and position on same, e.g., W24D02, where W24 is the wafer and D02 is the MOS capacitor.

In Fig. 3, *I-V* characteristics from MOS capacitors with oxide areas ranging from 100 μm^2 to 1 cm^2 with an increment in area of a decade are shown. The current is scaled with area to show the current density. It is seen that the six larger devices have similar current densities, while the smallest device lies a factor of 2–3 lower.

In Fig. 4, the *I-V* characteristics of a range of different 1 cm^2 area MOS capacitors are shown. The MOS capacitors measured are from four different wafers, but with several MOS capacitors from each wafer shown. The oxide thickness measured by ellipsommetry on each wafer is shown in parentheses after each wafer number. The oxide thickness extracted from *C-V* characteristics is shown after the number designating each MOS capacitor. From Fig. 4, it is seen that the thicknesses extracted from *C-V* characteristics and the relative position of the *I-V* characteristics show systematically and qualitatively good agreement. There is a variation in the oxide thickness between different wafers, but also between different MOS capacitors on the same wafer. Figure 4 shows a variation of typically 5 Å in oxide thickness on single wafers, and up to 15 Å from wafer to wafer. Variation in substrate dopant concentration is known to affect oxidation rates,[33,34] which can explain variations in oxide thickness.

IV. DISCUSSION

A. Functionality of ultralarge area oxides

With the general motivation for creating ultralarge area, high current electron emitters in mind, it is important to determine the transport mechanism of the electrons through the oxide. In order to have electron emission, the electrons must have an energy equal to or higher than the work function of the gate metal. This kind of extreme electron heating can only occur if the electrons are tunneling through the oxide. To verify the tunnel nature of the electron transport through the oxide, the higher bias part ($\gtrsim$3.4 V) of the *I-V* characteristics is compared to the Fowler-Nordheim[35–37] (FN) model for the current density:

$$J_{\text{FN}} = A F_{\text{ox}}^2 \exp\left(-\frac{B}{F_{\text{ox}}}\right), \tag{4}$$

where F_{ox} is the electric field in the oxide given by $F_{\text{ox}} = \frac{V_{\text{ox}}}{X_{\text{ox}}}$; A and B are constants given by

$$A = \frac{e^3}{16\pi^2 \hbar} \frac{m_{\text{Si}}}{\phi_B m_{\text{ox}}} \text{ and } B = \frac{4}{3} \frac{\sqrt{2 m_{\text{ox}}}}{e\hbar} \phi_B^{3/2}, \tag{5}$$

where e is the electron charge, $\hbar$ is the reduced Planck's constant, m_{Si} is the effective electron mass in silicon, m_{ox} is the effective electron mass in the oxide, and ϕ_B is the barrier height for electron tunneling, given by the difference between the Fermi level in the semiconductor and the conduction band edge of the insulator.

The model can be rewritten so as to yield a mean to linearize the *I-V* characteristics:

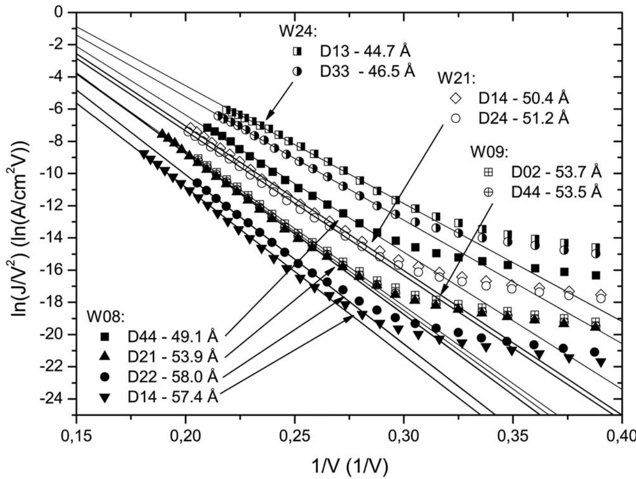

FIG. 5. The *I-V* characteristics from Fig. 4 shown in a Fowler plot. The data yield straight lines in the Fowler-Nordheim regime above 3.4 V, corresponding to ∼0.29 on the inverse voltage axis. The slope of the Fowler-Nordheim fit should be proportional to the thickness, as seen from Eq. (6).

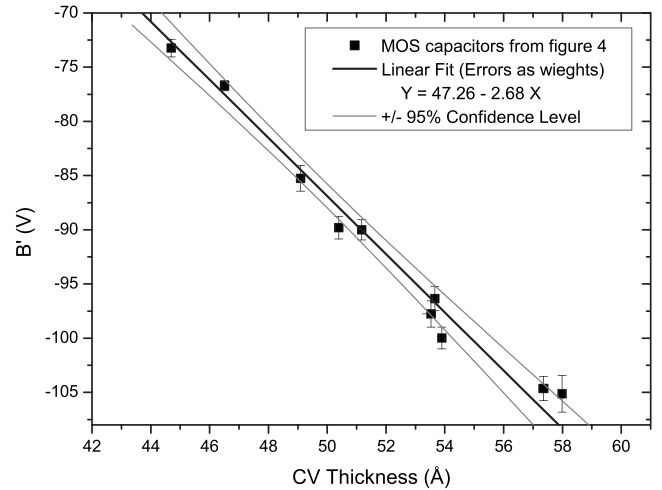

FIG. 6. The extracted slope from fits to the Fowler-Nordheim model (B') plotted against the oxide thickness extracted from *C-V* characteristics on the same devices.

$$\ln\left(\frac{J}{V_{\mathrm{ox}}^2}\right) = \ln(A') - \frac{B'}{V_{\mathrm{ox}}}, \qquad (6)$$

where $A' = \frac{A}{X_{\mathrm{ox}}^2}$ and $B' = BX_{\mathrm{ox}}$.

The *I-V* characteristics from Fig. 4 are shown as Fowler plots, using Eq. (6), in Fig. 5. The *I-V* characteristics fit the Fowler-Nordheim model very well above a bias voltage of ∼3.4 V, which matches well the sum of typical values for the flatband (FB) voltage $eV_{\mathrm{FB}} = \Phi_{\mathrm{Ti}} - \Phi_{\mathrm{Si}} \approx 4.3\ \mathrm{eV} - 4.1\ \mathrm{eV} = 0.2\ \mathrm{eV}$ and the tunnel barrier height $\phi_B \sim 3.2$ eV.[38]

B. Variations in the oxide thickness

A significant variation of the oxide thickness between devices and certainly from wafer to wafer is observed using *C-V* characteristics, but also more qualitatively from the *I-V* characteristics (Fig. 4) and again quantitatively from the slopes of the Fowler plots in Fig. 5.

From Fig. 4, it can be seen that there is a systematic relation between the thickness measured by *C-V* measurements and the apparent thickness in the *I-V* measurement. In order to quantify this further, the slopes extracted from the Fowler plot in Fig. 5 are plotted against the thicknesses derived from the *C-V* measurements of the same 1 cm^2 MOS capacitors in Fig. 6. From Eq. (6), it is seen that the slope (B') is directly proportional to the thickness of the oxide X_{ox} and would, therefore, be expected to yield a straight line intercepting the origin (0,0) when plotted against the thicknesses extracted from *C-V* measurements. As seen from Fig. 6, plotting B' against the thicknesses extracted from *C-V* measurements yields a straight line, but it does not intercept the origin when extrapolated. The oxide will not be completely flat, but will have a certain roughness and thickness variation from fabrication. A roughness or oxide thickness variation is weighted as $\frac{1}{X_{\mathrm{ox}}}$ in the *C-V* measurement, as seen from Eq. (3), but weighted as $\exp(-X_{\mathrm{ox}})$ in the *I-V* measurement, from which B' is extracted. As a direct consequence of those two different nonlinear weighings, the FN slopes (B') and the thickness probed by the *I-V* measurements will appear thinner than in the corresponding *C-V* measurements. From the fact that the *I-V* measurements give thinner areas exponentially more weight than areas with relatively thicker oxide, the offset in Fig. 6 can be explained by a thickness variation in the oxide. The characteristic length scale of the thickness variation must be on the order of 1 cm or larger, since the oxide thickness variations are clearly not averaged out in measurements on the square (1 cm^2) MOS capacitors.

In Fig. 7, the relative offset of the slope extracted from a Fowler plot is plotted against the nominal area of the devices for four series of devices. A series contains seven devices from 1 to 10^{-6} cm^2 in oxide area, situated close to each other on the same wafer. Since the slope of the Fowler plot is proportional to the thickness [see Eq. (5)] the relative offsets can be interpreted as relative differences in thickness. From Fig. 7, it is seen that there is a typical variation in thickness of ∼3%, which for a 50–60 Å thick oxide corresponds to ∼2 Å. The thicknesses of the smallest MOS capacitors (10^{-6} cm^2) are significantly larger than those of the larger area MOS capacitors.

The larger apparent thickness of the smallest oxide area MOS capacitors can be understood as a consequence of the variation in oxide thickness. In the simplest model, the thickness variation with a certain length scale is considered in two extreme regimes of MOS capacitor oxide areas. In the first regime, an area of oxide that is far larger than the length scale of the oxide thickness variation is considered. In this situation, an *I-V* measurement samples the entire distribution of oxide thicknesses, and each is weighted exponentially with regard to the thickness, and the total current is the surface integral of the current from each part of the thickness distribution:

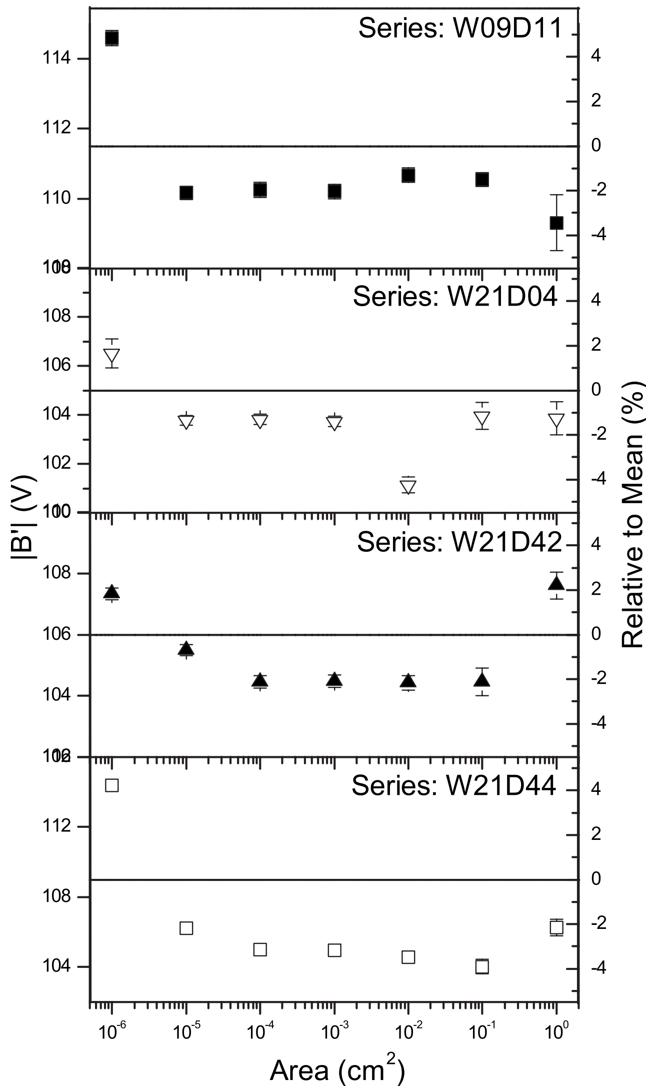

FIG. 7. Slopes (B') extracted from Fowler plots for four series of MOS capacitor, each series includes seven MOS capacitors of increasing area. The left axis shows the absolute value of the slopes, which are proportional to the oxide thickness. The right axis shows the relative deviation of each slope compared to the mean of each series. The error bars express the standard deviation of each slope value from the linear fit to the data plotted in a Fowler plot, not the statistical variation in oxide thickness for a particular MOS capacitor area.

$$I_{tot} = \int J_{FN}(X_{ox}(x,y))dA, \tag{7}$$

where I_{tot} is the total current of the MOS capacitor and $J_{FN}(X_{ox}(x,y))$ is the Fowler-Nordheim current density of a part of the oxide, with the thickness X_{ox} situated at (x,y). The current is integrated over the entire oxide area.

In the opposite extreme, the area of the MOS capacitor is very small compared to the length scale of the roughness or thickness variation; in this case, an *I-V* measurement samples one thickness of oxide and the *I-V* measurements for a series of MOS capacitors yield a distribution of current densities reflecting the variation in oxide thickness. Due to the exponential weighting by the tunnel current, the thicknesses extracted from the *I-V* measurements will be lower than the arithmetic mean of the distribution of oxide thicknesses present in the area sampled. Therefore, depending on the exact nature of the oxide thickness variation distribution, there will always be a larger probability of finding a larger than a smaller thickness of the smaller MOS capacitors compared to the larger MOS capacitors.

Taking an oxide thickness variation and an accompanying characteristic length scale into account make Fig. 7 relatively straightforward to interpret as expressing variations in oxide thicknesses with a characteristic length scale being ~ 10 μm. Another explanation for the larger apparent thickness of the smallest area (100 μm^2) MOS capacitors could be an edge effect arising from the fabrication technique, where back etching of a thick wet oxide to the Si substrate defines the area of the MOS capacitor as described in Sec. II A. In this case, one has to remember that the FN slope (B') is not directly dependent on the area of the MOS capacitor, but only indirectly through the integration of the current distribution [Eq. (7)].

The fact that the FN slope (B') is independent of area and no assumptions of the tunneling parameters, such as barrier height (ϕ_B) and effective electron mass in the oxide (m_{ox}), have been made makes this method of characterization very robust.

V. CONCLUSION

MOS devices with ultralarge area (1 cm^2) and ultrathin oxides (~ 5 nm) have been fabricated and characterized electrically by *C-V* and *I-V* measurements. The oxide thickness has been extracted from *C-V* characteristics by fitting to a model incorporating band bending and Fermi-Dirac statistics. The thicknesses obtained are realistic from an absolute perspective, by comparing with ellipsommetry, and they show qualitatively and systematically good agreement with the *I-V* characteristics. The thicknesses extracted from *C-V* characteristics as well as the *I-V* characteristics show a significant variation in the oxide thickness between MOS capacitors on the same wafer as well as between wafers. The spread in thicknesses measured on a single wafer is ~ 5 Å, while between wafers it is ~ 15 Å. The *I-V* characteristics of the MOS capacitors fit the Fowler-Nordheim model well in the region where the model is applicable, which is a strong evidence for the tunnel transport mechanism being dominant, and indicates that the MOS capacitors will work as electron emitters with a thinner gate metal layer. The *I-V* characteristics for the 1 cm^2 MOS capacitors are comparable to those with smaller oxide areas ($10^{-1}-10^{-6}$ cm^2). The smallest area MOS capacitors are significantly different from the others, which is well explained by the variation of the oxide thickness on a length scale comparable to the side length of these. The slopes extracted from Fowler plots give a different method of characterizing the oxide thickness and, when comparing several orders of magnitude of area, also a good quantitative measure of the oxide thickness variations and the characteristic length scales of these. For the MOS capacitors

fabricated in this work, two length scales of importance, namely ~10 μm and ~1 cm, were found. Of course, the data presented here are just a few samples of statistical phenomena and it is, therefore, not possible to conclude on the exact nature of the oxide thickness variations. It would be very interesting to see more elaborate studies of oxide thickness variations using slopes extracted from Fowler plots to gain information on the thickness variation of ultrathin oxides.

With regards to the motivation for the fabrication of ultralarge area electron emitters and the issues of oxide thickness variation discussed in the Introduction, there might be a problem with the large variation of thicknesses that is seen between different and across single large area MOS capacitors, since this can easily lead to a large difference in current density both between devices and from one side of a device to the other. These thickness variations might be improved upon by implementing alternative oxide growth methods and annealing, or, perhaps, by using alternative insulating materials for tunnel barriers.

ACKNOWLEDGMENT

The work presented has been funded by the Danish National Research Foundation as part of their grant to the Center for Individual Nanoparticle Functionality.

*ibchork@fysik.dtu.dk

[1] N. S. Xu and S. E. Huq, Mater. Sci. Eng., R. **48**, 47 (2005).
[2] B. R. F. Kendall, J. Vac. Sci. Technol. A **17**, 2041 (1999).
[3] J. Cohen, J. Appl. Phys. **33**, 1999 (1962).
[4] J. Cohen, Appl. Phys. Lett. **1**, 61 (1962).
[5] T. Sumiya, H. Fujinuma, T. Miura, and S. Tanaka, Appl. Surf. Sci. **130–132**, 36 (1998).
[6] D. J. DiMaria, M. V. Fischetti, J. Batey, L. Dori, E. Tierney, and J. Stasiak, Phys. Rev. Lett. **57**, 3213 (1986).
[7] S. D. Brorson, D. J. DiMaria, M. V. Fischetti, F. L. Pesavento, P. M. Solomon, and D. W. Wong, J. Appl. Phys. **58**, 1302 (1985).
[8] H. Mimura, Y. Neo, H. Shimawaki, T. Matsumoto, and K. Yokoo, Appl. Surf. Sci. **144**, 498 (2005).
[9] E. Y. Wu and J. Sune, Microelectron. Reliab. **45**, 1809 (2005).
[10] M. Poppeller, E. Cartier, and R. M. Tromp, Microelectron. Eng. **46**, 183 (1999).
[11] J. W. Gadzuk, Phys. Rev. Lett. **76**, 4234 (1996).
[12] J. W. Gadzuk, J. Vac. Sci. Technol. A **15** 1520 (1997).
[13] J. W. Gadzuk, Phys. Rev. B **44**, 13466 (1991).
[14] J. W. Gadzuk and C. W. Clark, J. Chem. Phys. **91**, 3174 (1989).
[15] D. Diesing, G. Kritzler, M. Stermann, D. Nolting, and A. Otto, J. Solid State Electrochem. **7**, 389 (2003).
[16] T. Wadayama, A. Kojim, and A. Hatta, Appl. Phys. A: Mater. Sci. Process. **79**, 1891 (2004).
[17] D. Diesing, H. Janssen, and A. Otto, Surf. Sci. **331–333**, 289 (1995).
[18] R. G. Sharpe, S. J. Dixon-Warren, P. J. Durston, and R. Palmer, Chem. Phys. Lett. **234**, 354 (1995).
[19] T. Wadayama and M. Yokawa, Chem. Phys. Lett. **428**, 348 (2006).
[20] E. H. Nicollian and J. R. Brews, *MOS (Metal Oxide Semiconductor) Physics and Technology* (Wiley, New York, 1982).
[21] M. Hirose, M. Koh, W. Mizubayashi, H. Murakami, K. Shibahara, and S. Miyazaki, Semicond. Sci. Technol. **15**, 485 (2000).
[22] P. Mur *et al.*, Appl. Surf. Sci. **175–176**, 726 (2001).
[23] M. Houssa, T. Nigam, P. W. Mertens, and M. M. Heyns, Solid-State Electron. **43**, 159 (1999).
[24] O. Maida, H. Yamamoto, N. Okada, T. Kanashima, and M. Okuyama, Appl. Surf. Sci. **130–132**, 214 (1998).
[25] A. Crossley, C. J. Sofield, J. P. Goff, A. C. I. Lake, M. T. Hutchings, and A. Menelle, J. Non-Cryst. Solids **187**, 221 (1995a).
[26] S. Lombardo, J. H. Stathis, B. P. Linder, T. Watson, K. L. Pey, F. Palumbo, and C. H. Tung, J. Appl. Phys. **98**, 121301 (2005).
[27] B. P. Linder and J. H. Stathis, Microelectron. Eng. **72**, 24 (2004).
[28] J. Verweij and J. Klootwijk, Microelectron. J. **27**, 611 (1996).
[29] A. Crossley, C. J. Sofield, J. P. Goff, A. C. I. Lake, M. T. Hutchings, and A. Menelle, J. Non-Cryst. Solids **187**, 221 (1995b).
[30] W. Kern, *Handbook of Semiconductor Wafer Cleaning Technology—Science, Technology, and Applications* (Noyes, New York, 1993).
[31] S. V. Walstra and C.-T. Sah, IEEE Trans. Electron Devices **44**, 1136 (1997).
[32] E. Vincent, G. Ghibaudo, G. Morin, and C. Papadas, Proceedings of the IEEE International Conference on Microelectronic Test Structures, Monterey, CA, 1997 (unpublished), pp. 105–110.
[33] C. P. Ho and J. D. Plummer, J. Electrochem. Soc. **126**, 1516 (1979).
[34] C. P. Ho and J. D. Plummer, J. Electrochem. Soc. **126**, 1523 (1979).
[35] R. H. Fowler and L. W. Nordheim, Proc. R. Soc. London, Ser. A **119**, 173 (1928).
[36] M. Lenzlinger and E. H. Snow, J. Appl. Phys. **40**, 278 (1969).
[37] Z. Weinberg, J. Appl. Phys. **53**, 5052 (1982).
[38] H. C. Card, Solid State Commun. **14**, 1011 (1974).